E.O. Paton Electric Welding Institute of the National Academy of Science of Ukraine
International Association «Welding»
LLC «Scientific Journals»

The Paton Welding Journal

03
2022

International Scientific-Technical and Production Journal ◊ Founded in January 2000 (12 Issues Per Year)

EDITORIAL BOARD

Editor-in-Chief	
I.V. Krivtsun	E.O. Paton Electric Welding Institute, Kyiv, Ukraine
Deputy Editor-in-Chief	
S.V. Akhonin	E.O. Paton Electric Welding Institute, Kyiv, Ukraine
Deputy Editor-in-Chief	
L.M. Lobanov	E.O. Paton Electric Welding Institute, Kyiv, Ukraine
Editorial Board Members	
O.M. Berdnikova	E.O. Paton Electric Welding Institute, Kyiv, Ukraine
Chang Yunlong	School of Materials Science and Engineering, Shenyang University of Technology, Shenyang, China
V.V. Dmitrik	NTUU «Kharkiv Polytechnic Institute», Kharkiv, Ukraine
Dong Chunlin	China-Ukraine Institute of Welding of Guangdong Academy of Sciences, Guangzhou, China
A. Gumenyuk	Bundesanstalt für Materialforschung und –prüfung (BAM), Berlin, Germany
V.V. Knysh	E.O. Paton Electric Welding Institute, Kyiv, Ukraine
V.M. Korzhyk	E.O. Paton Electric Welding Institute, Kyiv, Ukraine
V.V. Kvasnytskyi	NTUU «Igor Sikorsky Kyiv Polytechnic Institute», Kyiv, Ukraine
Yu.M. Lankin	E.O. Paton Electric Welding Institute, Kyiv, Ukraine
S.Yu. Maksymov	E.O. Paton Electric Welding Institute, Kyiv, Ukraine
Yupiter HP Manurung	Smart Manufacturing Research Institute, Universiti Teknologi MARA, Shah Alam, Malaysia
M.O. Pashchin	E.O. Paton Electric Welding Institute, Kyiv, Ukraine
Ya. Pilarczyk	Welding Institute, Gliwice, Poland
V.D. Poznyakov	E.O. Paton Electric Welding Institute, Kyiv, Ukraine
U. Reisgen	Welding and Joining Institute, Aachen, Germany
I.O. Ryabtsev	E.O. Paton Electric Welding Institute, Kyiv, Ukraine
V.M. Uchanin	Karpenko Physico-Mechanical Institute, Lviv, Ukraine
Yang Yongqiang	South China University of Technology, Guangzhou, China
Managing Editor	
O.T. Zelnichenko	International Association «Welding», Kyiv, Ukraine

Address of Editorial Board
E.O. Paton Electric Welding Institute, 11 Kazymyr Malevych Str. (former Bozhenko), 03150, Kyiv, Ukraine
Tel./Fax: (38044) 200 82 77, E-mail: journal@paton.kiev.ua
https://patonpublishinghouse.com/eng/journals/tpwj

State Registration Certificate 24933-14873 ПР from 13.08.2021
ISSN 0957-798X, DOI: http://dx.doi.org/10.37434/tpwj

Subscriptions, 12 issues per year:
$384 — annual subscription for the printed (hard copy) version, air postage and packaging included;
$312 — annual subscription for the electronic version (sending issues in pdf format or providing access to IP addresses).

Representative Office of «The Paton Welding Journal» in China:
China-Ukraine Institute of Welding, Guangdong Academy of Sciences
Address: Room 210, No. 363 Changxing Road, Tianhe, Guangzhou, 510650, China.
Zhang Yupeng, Tel: +86-20-61086791, E-mail: patonjournal@gwi.gd.cn

The content of the journal includes articles received from authors from around the world in the field of welding, metallurgy, material science and selectively includes translations into English of articles from the following journals, published by PWI in Ukrainian:

- Automatic Welding (https://patonpublishinghouse.com/eng/journals/as);
- Technical Diagnostics & Nondestructive Testing (https://patonpublishinghouse.com/eng/journals/tdnk);
- Electrometallurgy Today (https://patonpublishinghouse.com/eng/journals/sem).

© E.O. Paton Electric Welding Institute of NASU, 2022
© International Association «Welding» (Publisher), 2022
© LLC «Scientific Journals», 2022

CONTENTS

ORIGINAL ARTICLES

---

*Translated Article(s) from «Automatic Welding», No. 3, 2022.

**Translated Article(s) from «Electrometallurgy Today», No. 4. 2021.

***Translated Article(s) from «Technical Diagnostics & Nondestructive Testing», No. 1, 2022.

JOINT EDUCATION AND RESEARCH LABORATORY OF WELDING AND RELATED PROCESSES

Main building of NTUU Igor Sikorsky KPI

Modern conditions for the development of progressive technologies require the integration of certain processes to obtain a new quality of products. The basic condition for such integration processes is the combination of a scientific experience of researchers working over related problems in different scientific divisions. This approach provides a more full analysis and solution to the problems that researchers have to do with when scientific and technological progress is constantly marching on.

Combining efforts of scientists in solving problems of plasma and hybrid welding and additive arc technologies has already become necessary a long time ago. Several decades ago, this need has led to an intensive development and branching of the E.O. Paton Electric Welding Institute of the NAS of Ukraine. However, modern realities require finding new approaches. In 2017, the basis for their creation was found. At the initiative of the National Technical University of Ukraine “Igor Sikorsky Kyiv Polytechnic Institute” and with the support of Academician B.E. Paton, five scientific and technical organizations took part in the foundation of the Joint Education and Research Laboratory of Welding and Related Processes. Among the founders there were:

- PWI;
- Foreign Economic Representation of the E.O. Paton Chinese-Ukrainian Institute of Welding;
- National Technical University of Ukraine “Igor Sikorsky KPI”;
- “Scientific and Production Center “PLAZER” Ltd;
- “Ukrspetstekhnologiyi” Corporation.

The foundation of the Joint Research Laboratory with the support of Academician B.E. Paton was legally settled by an agreement on cooperation No.2500/17-0 dated 13.06.2019.

The aim of the Laboratory foundation is building of a scientific and technological experimental base of a collective use with the attraction of the most advanced equipment for research works in plasma, laser and hybrid welding technologies and related processes, additive technologies, diffusion welding and brazing.

To achieve this aim it is planned to solve the following tasks:

1. Creation of new forms of scientific and technical cooperation by combining the creation of a scientific experimental base of a collective use with the involvement of modern equipment for conducting research works in the fields of advanced welding technologies and related processes using the material and technical base of research, educational and scientific-production organizations.
2. Attraction of investments, including from foreign partners.
3. Expansion of international scientific and technical cooperation and cooperation between research institutions and industrial enterprises in Ukraine, attraction of leading Ukrainian and international scientists and specialists to participation in scientific and technological developments.

Main building of E.O. Paton Electric Welding Institute

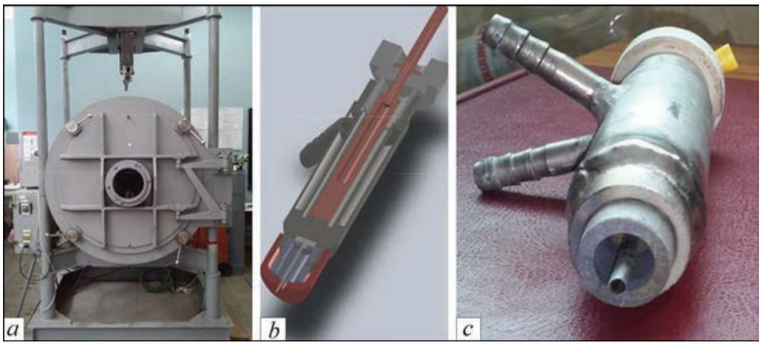

Figure 1. Appearance of vacuum chamber (*a*) and plasmatron (model (*b*) and a specimen made on its base (*c*)) for vacuum plasma-emission discharge welding

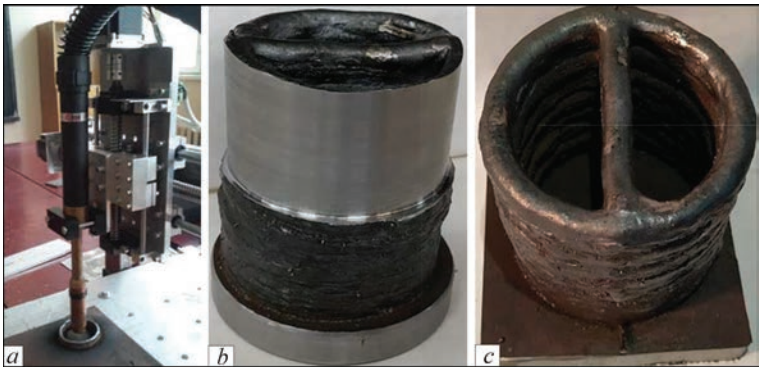

Figure 2. Head (*a*) with a consumable electrode for additive growing of parts with inner stiffeners (*b*, *c*)

4. Education of scientific personnel, involvement of students of higher education institutions of Ukraine with bachelor, master and Ph-D levels of education to participate in real scientific, technical and production projects.

At present, the structure of the Joint Laboratory includes two experimental and technological platforms: “Plasma and hybrid welding and additive arc technologies” (E.O. Paton Educational and Research Institute of Materials Science and Welding of the Igor Sikorsky KPI) and “Demonstration and technological platform of plasma, hybrid and additive technologies” (PWI, LLC “Scientific and Production center “PLAZER”, Foreign Economic Representation of the E.O. Paton Chinese-Ukrainian Institute of Welding). Scientific supervisor of the Joint Laboratory is Dr. of Techn. Sci., Prof. V.M. Korzhyk, the correspondent member of the NASU.

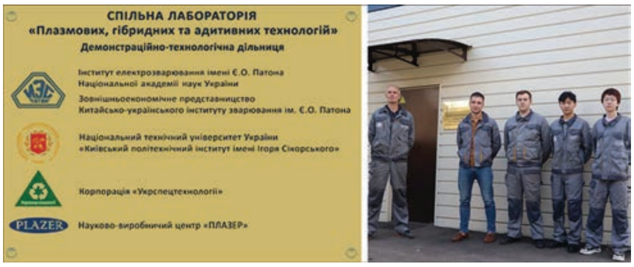

Figure 3. Mock-up of the title board of the Demonstration and technological platform and its opening by the international research team

Within the frames of Cooperation Agreements, concluded with the PWI, the mentioned Joint Laboratory is the base for international scientific and technical cooperation with the Welding Technologies Research Institute in Zhejiang Province (PRC) and Zhejiang Special Equipment Research Institute (PRC).

In the Laboratory of plasma and hybrid welding and additive arc technologies, research works are carried out on the development and further advancing of such progressive processes as:

- hollow cathode vacuum welding with a plasma-emission direct current discharge of straight polarity;
- vacuum diffusion welding;
- vacuum brazing;

Figure 4. One of the laboratory facilities of the Demonstration and technological platform

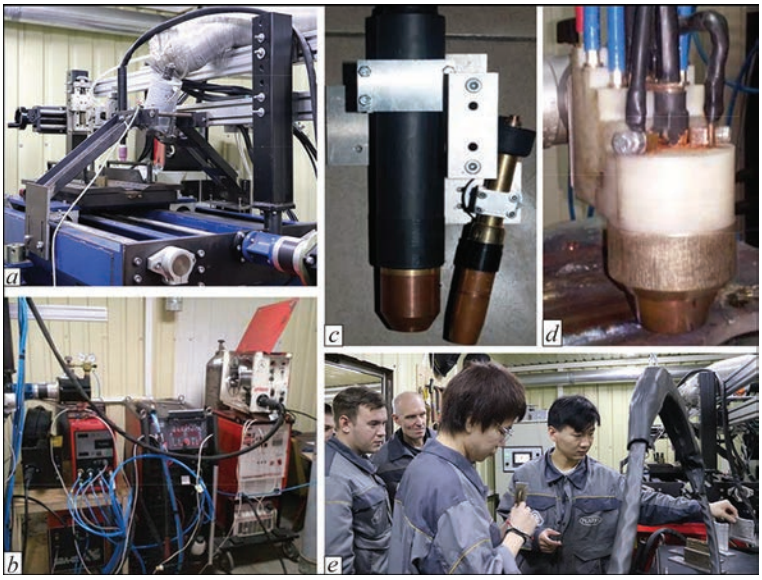

Figure 5. Universal technological complex of plasma-arc and hybrid technologies, automatic combined and hybrid welding "plasma + arc of a consumable electrode": *a* — manipulator for welding in different spatial positions; *b* — welding equipment; *c* — monoblock of combined plasma + MIG/MAG welding; *d* — plasmatron for hybrid plasma-MIG/MAG welding; *e* — familiarization of foreign partners with the equipment and technology within the framework of international scientific and technical cooperation

- additive growing of parts by means of a consumable electrode.

For realization of research works, complexes of the corresponding vacuum equipment were created (Figure 1). The study of a plasma-emission discharge (plasma-arc discharge with a hollow cathode) in vacuum proved the possibility of its successful use in welding of titanium alloys with a thickness of up to 16 mm without edge preparation. At the same time, in terms of quality and service characteristics, the produced welds are approaching the results obtained by electron beam welding at a significantly lower cost.

Also, in this division of the Joint Laboratory, additive growing of parts by means of a consumable electrode is investigated. In particular, technologies for manufacture of metal parts of a complex spatial shape with inner stiffeners are developed (Figure 2).

On the "Demonstration and technological platform of plasma, hybrid and additive technologies" (Figure 3), the development of such technologies is carried out as:

- robotic seam and spot plasma welding by a direct current of straight polarity;
- robotic seam and spot plasma welding of aluminium and magnesium alloys by a bipolar asymmetric current;
- robotic (automated) plasma-powder cladding by a direct current of straight polarity and by a bipolar asymmetric current (for aluminium and magnesium alloys);
- robotic (automated) welding in the mode of "mild plasma" by a direct current of straight polarity and by a bipolar asymmetric current (for aluminium and magnesium alloys);

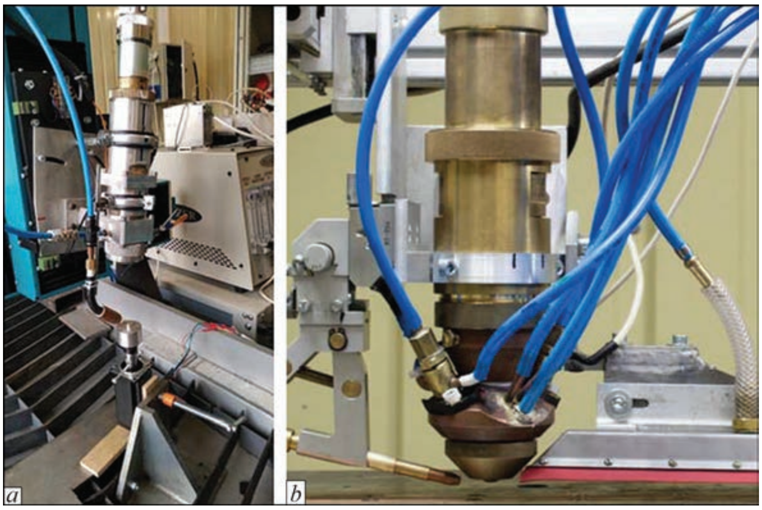

Figure 6. Heads for laser (*a*) and hybrid laser-plasma welding (*b*) created in the Joint Laboratory

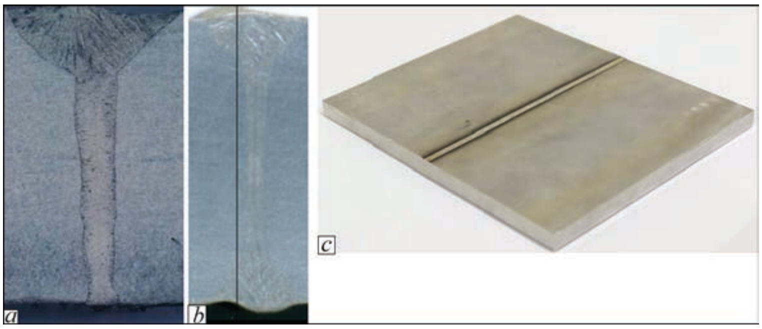

Figure 7. Macrostructures of joints of 6 (*a*) and 10 mm (*b*) thickness produced by laser-plasma welding in one and two passes, respectively, and the appearance of butt joints of 10 mm thickness (*c*). Material — stainless AISI304 steel

- robotic (automated) welding and surfacing applying the process of welding by a consumable electrode with short circuits (CMT — Cold Metal Transfer);
- robotic (automated) argon-arc welding by a direct current of straight polarity and by a bipolar asymmetric current (for aluminium and magnesium alloys);
- laser welding in a controlled atmosphere and in a dynamic vacuum;
- robotic (automated) laser cutting and welding;
- hybrid welding processes (plasma-MIG/MAG, plasma-TIG, laser-plasma, laser-MIG/MAG, laser-TIG);
- hybrid laser-plasma cutting;
- plasma cutting of metal sheets of increased thicknesses on the reverse polarity;
- plasma cutting with different types of plasma-forming gases and addition of water;
- supersonic plasma powder spraying of coatings;
- high-velocity plasma-arc spraying of coatings by conductive wires;
- high-velocity electric arc two-wire spraying of coatings in the products of combustion of hydrocarbon gases;
- hybrid supersonic electric arc oxy-fuel two-wire spraying of coatings;
- supersonic high-velocity oxy-fuel spraying of coatings by powders and wires (HVOF);
- plasma technologies of powder spheroidization;
- growing of three-dimensional products by additive layer-by-layer microplasma, plasma and arc cladding (3D-printing).

To study the mentioned technologies, there are appropriate laboratory facilities with the necessary technological equipment (Figure 4). Also office premises, a modern conference room with the possibility of online conferences, areas for mechanical treatment with milling and turning machine tools, utility and warehouse premises, etc. are provided. In particular, the Demonstration and technological platform for plasma-arc and hybrid technologies was certified by the Certificate on the quality management system ISO 9001:2015.

Specially, the innovative hybrid technologies should be noted, which are developed on the Demonstration and technological platform. Thus, the equipment and technologies of automatic and robotic combined (Plasma + MIG/MAG) and hybrid (Plasma-MIG/MAG) welding by a constricted arc of a nonconsumable electrode with an arc of a consumable electrode arc allow joining sheets of aluminium alloys with a thickness of up to 16 mm for a one pass, minimizing the tendency to inner pore formation in welds, increasing the efficiency of welding by eliminating the operations on edge preparation, increasing

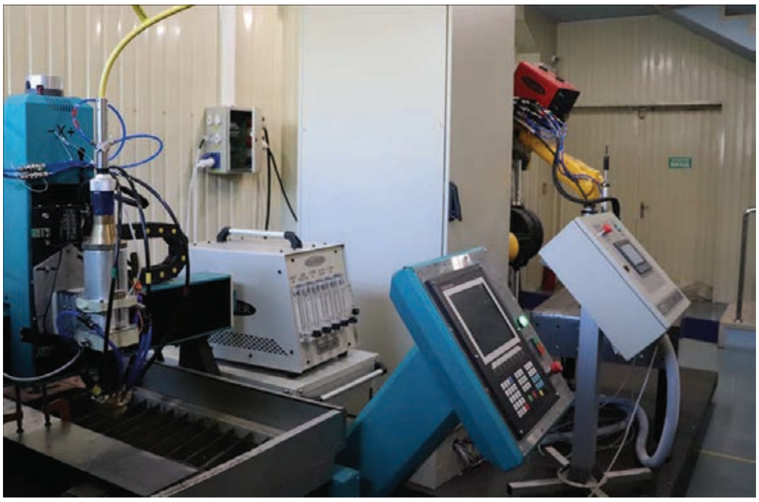

Figure 8. Universal technological complex for laser and hybrid laser-plasma cutting

Figure 9. Complex for laser, microplasma and laser-microplasma welding in a controlled atmosphere and in a dynamic vacuum

welding speed up to two times as compared to conventional MIG/MAG-welding (Figure 5).

The equipment and technologies for laser and hybrid laser-plasma welding created in the Joint Laboratory allow producing joints of steels and alloys with a high thermal locality and speed of welding. A vivid example of achievements in the field of laser-plasma welding is the production of single- and two-pass butt joints of stainless AISI304 steel of 6 and 10 mm thickness, respectively, at a speed of 60 m/h using 1.8 kW radiation power of a fiber laser (Figures 6, 7).

Among the challenging technological developments, created on the basis of the Joint Laboratory, a universal technological complex of laser and hybrid laser-plasma cutting (Figure 8), laser, microplasma and laser-microplasma welding in a controlled atmosphere and in a dynamic vacuum (Figure 9), installation (3D printer) for 3D-printing by a powder

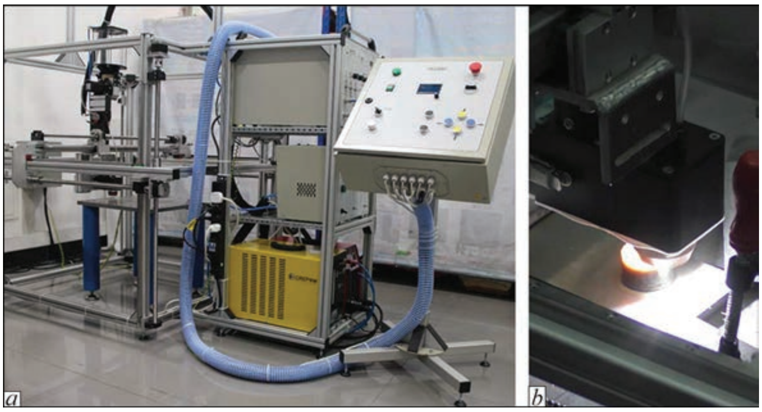

Figure 10. Appearance of installation (*a*) and process (*b*) for microplasma 3D-printing using powder materials

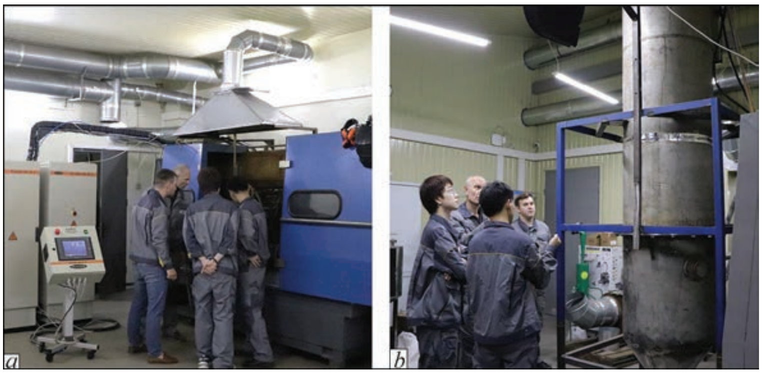

Figure 11. Equipment for realization of plasma-arc technologies for spraying of coatings and treatment of materials: *a* — universal technological complex of plasma-arc spraying and cutting; *b* — experimental installation for plasma-arc spheroidization of wire materials and rods and powders of irregular shape

Figure 12. Familiarization of the Academician of the NASU I.V. Krivtsun, Director of the PWI, with the capacities of the Joint Laboratory

microplasma layer-by-layer cladding can be attributed (Figure 10).

At present, the works on the development and industrialization of plasma-arc technologies of spraying coatings and treatment of materials, production of spherical powders by plasma-arc spraying of wires and rods, plasma-arc spheroidization of powders of irregular shape are actively continuing. With this purpose, the necessary equipment and technological base were created (Figure 11).

After opening of the Joint Laboratory, its Demonstration and technological platform was visited by leading staff scientists of the NAS of Ukraine, in particular, Academicians of the NASU I.V. Krivtsun and L.M. Lobanov (Figure 12). They approved the technical equipment of the Laboratory and highly praised the scientific and technological developments, which are currently carried out by its staff colleagues. Further, it is planned to visit the Joint Laboratory by delegations of foreign scientists and managers, which are interested in scientific cooperation and industrial implementation of developed technologies.

The management of the Joint Laboratory offers the application of the described advanced innovation equipment with all those desirable researchers, students and postgraduate students. Research works can be conducted both within the joint projects as well as on individual agreements. A separate task is teaching students and postgraduate students. The Laboratory gladly welcomes not only domestic students, but also foreign ones — all who wishes to raise their own skills within the framework of joint projects and programs. For this purpose, both specialists of the Laboratory, as well as third-party specialists may be involved. The latter may be involved on individual principles. In general, the Joint Education and Research Laboratory was built as a scientific and technological experimental base of a collective use. The accumulated advanced experience and available innovative equipment are aimed to be attracted for research works in the fields of advanced technologies of welding and related processes.

V.M. Korzhyk[1], V.V. Kvasnytskyi[1,2], V.Yu. Khaskin[1]
[1]E.O. Paton Electric Welding Institute of the NAS of Ukraine,
[2]NTUU “Igor Sikorsky KPI”

https://doi.org/10.37434/tpwj2022.03.01

CHARACTERISTICS OF HIGH-FREQUENCY PULSED CURRENT ARC WITH REFRACTORY CATHODE

I. Krivtsun[1], V. Demchenko[1], I. Krikent[1], U. Reisgen[2], O. Mokrov[2], R. Sharma[2]

[1]E.O. Paton Electric Welding Institute of the NASU
11 Kazymyr Malevych Str., 03150, Kyiv, Ukraine
[2]RWTH Aachen University, ISF – Welding and Joining Institute
Pontstr. 49, 52062, Aachen, Germany

ABSTRACT

A self-consisted mathematical model is presented, describing nonstationary processes of energy, momentum, mass and charge transfer in plasma column and anode boundary layer of an electric arc burning in atmospheric pressure inert gas at pulsed modulation of current. A numerical study of distributed and integrated characteristics of 2 mm long argon arc was performed in the case of current modulation by rectangular pulses at 10 kHz frequency and different values of the duty cycle (0.3; 0.5; 0.7) under the condition that the average current value remains unchanged and equal to 140 A. Calculated time dependencies of plasma temperature, velocity and current density in the arc column centre, as well as axial values of plasma temperature and pressure near the anode surface, anode current density and heat flux into the anode are given for the selected values of duty cycle. Radial distributions of averaged over the current modulation period heat flux, introduced by the arc into the anode, pressure and force of friction of arc plasma flow on its surface were calculated, which are the determinant ones for simulation of thermal and hydrodynamic processes in the metal being welded in TIG welding with high-frequency pulsed current (HFPC) modulation. Results of simulation of nonstationary arc characteristics are compared with the respective results for a direct current (DC) arc, at current equal to average value of modulated current. Analysis of the obtained results leads to the conclusion that in the case of HFPC TIG welding at 10 kHz frequency decrease of duty cycle (increase of pulse current) at constant value of average current leads to greater force impact of such an arc on weld pool metal and to increase of its penetrability, respectively.

KEYWORDS: electric arc, refractory cathode, arc column, anode boundary layer, TIG welding, pulsed current modulation, frequency, duty cycle, simulation

INTRODUCTION

TIG welding currently is one of the main technological processes of producing high-quality permanent joints of critical structures from steels, titanium and aluminium alloys. This welding process is realized by excitation of DC electric arc in inert shielding gas (Ar, He or their mixture) between refractory (W) cathode and item being welded, which is the anode [1].

There are different modifications of TIG welding, one of which is welding current modulation. A large number of works are devoted to experimental study of the features of this process (see, for instance, [2–8]). Modes of TIG welding with low-frequency (modulation frequency $f \leq 50$ Hz) [2, 3, 4, 7, 8]), medium-frequency ($f \sim 5$ kHz) [3, 4]) and high-frequency ($f \geq 10$ kHz) [3, 5, 6]) arc current modulation were investigated. Results of these studies lead to the conclusion that variation of such parameters of welding current modulation as frequency, pulse ratio, amplitude and shape of the pulses, allows controlling the metal penetration shape, and thermal cycle of welding and, therefore, influencing the structure and properties of metal of the weld and heat-affected zone.

Works [9–11] are devoted to theoretical study and computer simulation of the processes, running in the welding arc and metal being welded in TIG welding with low-frequency pulsed current modulation. The problems of simulation of distributed and integrated characteristics of arc plasma and its impact on the metal being welded in HFPC TIG welding are not given enough attention in modern scientific and technical publications. Therefore, the objective of this work is numerical analysis of nonstationary processes of energy, momentum, mass and charge transfer in the arc with a refractory cathode at HFPC modulation in the range of 30–400 A by rectangular pulses at 10 kHz frequency.

Let us consider a nonstationary electric arc with a refractory cathode and water-cooled (nonevaporating) anode, burning in atmospheric pressure inert gas, the diagram of which is shown in Figure 1. At construction of a mathematical model of such an arc, we will give the main attention to processes running in the column and anode boundary layer of arc plasma. For self-consistent description of the above-mentioned processes, we will use an approach, described in detail in [12], according to which we will divide arc plasma into two regions: arc column, where plasma is in the state of local thermodynamic equilibrium and anode boundary layer of thermally and ionizationally nonequilibrium plasma. Accordingly, a self-consistent mathematical model of the considered system should include two interrelated models:

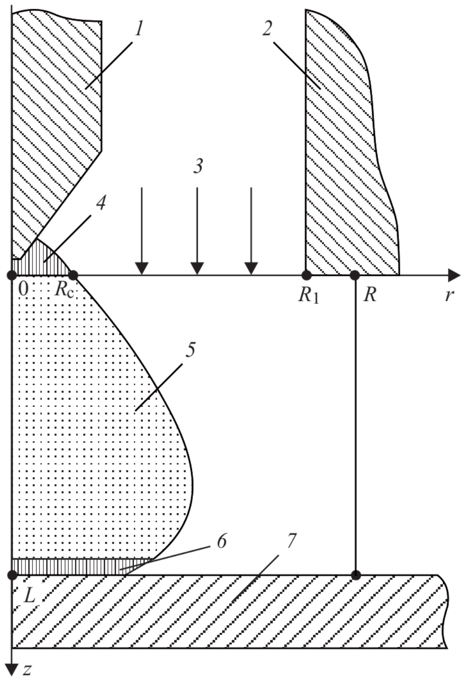

Figure 1. Diagram for simulation of a nonstationary arc: *1* — refractory cathode; *2* — nozzle for shielding gas feeding; *3* — shielding inert gas; *4* — cathode region; *5* — arc column; *6* — anode boundary layer; *7* — water-cooled anode; R_c — radius of the region of the arc cathode attachment; R_1 — protective nozzle radius; R — calculation domain radius, L — arc length

- Model of nonstationary thermal, electromagnetic and gas-dynamic processes in arc column plasma at pulsed current modulation.
- Model of anode boundary layer, allowing formulation of boundary conditions on the interface of plasma column with the above layer, which, on the one hand, are required to solve the equations of the first model, and on the other hand they are needed for determination of the characteristics of thermal, electric and force impact of a nonstationary arc on the anode surface.

MODEL OF NONSTATIONARY ARC COLUMN

At construction of the model of thermal, electromagnetic and gas-dynamic processes in arc column plasma at pulsed modulation of current, we will use the following approximations:

- the system is assumed to be axisymmetric, anode surface is flat and is perpendicular to the arc axis;
- arc column plasma contains only shielding gas particles (electrode material evaporation is neglected), it is in the state of local thermodynamic equilibrium (one-temperature model of ionizationally equilibrium plasma is used) and it is optically thin for intrinsic radiation;
- main mechanism of plasma heating is Joule heating (work of pressure forces and viscous dissipation are ignored), while energy transfer in arc column takes place through thermal conductivity, convection and transport of energy of the plasma electron component;
- electromagnetic processes in arc plasma are assumed to be quasistationary (bias currents are neglected);
- arc column plasma flow is viscous, subsonic, flow mode is laminar;
- gravitational force is neglected, external magnetic fields are absent.

The corresponding to these approximations system of differential equations for description of nonstationary processes in arc column plasma, written in the cylindrical system of coordinates {r, φ, z} has the following form:

- Mass conservation equation

$$\frac{\partial\rho}{\partial t}+\frac{1}{r}\frac{\partial}{\partial r}(r\rho v)+\frac{\partial}{\partial z}(\rho u)=0, \tag{1}$$

where ρ is the mass density of plasma; *v*, *u* are the radial and axial components of its velocity.

Equations of momentum conservation

$$\rho\left(\frac{\partial v}{\partial t}+v\frac{\partial v}{\partial r}+u\frac{\partial v}{\partial z}\right)=-\frac{\partial P}{\partial r}-$$

$$-j_z B_\varphi+\frac{2}{r}\frac{\partial}{\partial r}\left(r\eta\frac{\partial v}{\partial r}\right)+\frac{\partial}{\partial z}\left[\eta\left(\frac{\partial u}{\partial r}+\frac{\partial v}{\partial z}\right)\right]- \tag{2}$$

$$-2\eta\frac{v}{r^2}-\frac{2}{3}\frac{\partial}{\partial r}\left\{\eta\left[\frac{1}{r}\frac{\partial(rv)}{\partial r}+\frac{\partial u}{\partial z}\right]\right\};$$

$$\rho\left(\frac{\partial u}{\partial t}+v\frac{\partial u}{\partial r}+u\frac{\partial u}{\partial z}\right)=-\frac{\partial P}{\partial z}+$$

$$+j\ \ B\ \ +\ \frac{\partial}{\partial z}\left(\eta\frac{\partial u}{\partial z}\right)+\frac{}{r}\frac{\partial}{\partial r}\left[r\eta\left(\frac{\partial u}{\partial r}+\frac{\partial v}{\partial z}\right)\right]- \tag{3}$$

$$-\frac{2}{}\frac{\partial}{\partial z}\left\{\eta\left[\frac{1}{r}\frac{\partial(rv)}{\partial r}+\frac{\partial}{\partial z}\right]\right\}$$

where *P* is the pressure; j_z, j_r are the axial and radial components of current density in the arc; B_φ is the azimuth component of magnetic induction vector; η is the coefficient of dynamic viscosity. Since the pressure can be determined up to the constant, let's choose such a constant from the condition that pressure in external media corresponds to atmospheric one. The value P should be understood below to refer to overpressure.

- Energy conservation equation

$$\rho C_p \left(\frac{\partial T}{\partial t} + v \frac{\partial T}{\partial r} + u \frac{\partial T}{\partial z} \right) =$$
$$= \frac{1}{r} \frac{\partial}{\partial r} \left(r\chi \frac{\partial T}{\partial r} \right) + \frac{\partial}{\partial z} \left(\chi \frac{\partial T}{\partial z} \right) + \frac{k}{e} \times \tag{4}$$
$$\times \left\{ j_r \frac{\partial \left[(5/2 - \delta) T \right]}{\partial r} + j_z \frac{\partial \left[(5/2 - \delta) T \right]}{\partial z} \right\} +$$
$$+ \frac{j_r^2 + j_z^2}{\sigma} - \psi,$$

where C_p is the specific heat of arc plasma, allowing for ionization energy; T is the plasma temperature; χ is the coefficient of thermal conductivity; k is the Boltzmann constant; e is the electron charge; δ is the thermal diffusion constant; ψ are the radiation energy losses.

- Equations of electromagnetic field

$$\frac{1}{r} \frac{\partial}{\partial r} \left(r \sigma \frac{\partial \varphi}{\partial r} \right) + \frac{\partial}{\partial z} \left(\sigma \frac{\partial \varphi}{\partial z} \right) = 0; \tag{5}$$

$$B_\varphi (r, z) = \frac{\mu^0}{r} \int_0^r j_z (\xi, z)\, \xi \, d\xi, \tag{6}$$

where φ is the electric potential; σ is the specific heat conductivity of plasma; μ^0 is the universal magnetic constant;

$$j_r = -\sigma \frac{\partial \varphi}{\partial r}; \qquad j_z = -\sigma \frac{\partial \varphi}{\partial z}. \tag{7}$$

Before we go over to consideration of the initial and boundary conditions for equations (1)–(5), we will briefly describe the model of the arc anode boundary layer used in this paper.

MODEL OF ANODE BOUNDARY LAYER

According to the model proposed in [12, 13], the anode boundary layer is assumed to be infinitely thin, compared to arc column dimensions, and potential drop in this layer (anode drop) $U_a = \varphi_a - \varphi_{pa}$ is negative and its distribution along the anode surface is nonuniform. Here, φ_a is the anode surface potential assumed to be constant, in view of the high conductivity of the anode metal, and selected equal to zero further on, while φ_{pa} is the potential of arc column plasma on the interface with the anode boundary layer, the value of which depends on distance r to the arc axis for an axisymmetric arc. To calculate the radial distribution of plasma potential on the above-mentioned interface, we will use expression [13], which in the case of nonevaporating anode (arc plasma contains just the atoms and single-charged ions of shielding gas) can be written in the following form

$$\varphi_{pa}(r) = \frac{kT(r,L)}{e} \ln \left(\frac{e n_e (r,L) \upsilon_e (r,L)}{4 \left[j_a(r) + j_i(r) \right]} \right), \tag{8}$$

where $T(r, L)$, $n_e(r, L)$, $\upsilon_e(r,L) = \sqrt{8kT(r,L)/\pi m_e}$ are the radial distributions of temperature, concentration and thermal velocity of plasma electrons on the interface of the arc column with the anode boundary layer, m_e is the electron mass; $j_a(r) = |j_z(r, L)|$, $j_i(r) = e n_i (r,L) \exp\left(-\frac{1}{2}\right) \sqrt{\frac{k\left[T(r,L) + T_s\right]}{M}}$ are the respective distributions of normal to the anode surface component of the density of the arc anode current and ion current from the plasma to anode surface, $n_i(r, L)$ is the distribution of plasma ion concentration on the interface of the arc column with the anode boundary layer, M is the ion mass, T_s is the anode surface temperature. Taking into account the above assumption of ionisational equilibrium of arc column plasma, the distributions of $n_e(r, L)$, $n_i(r, L)$ and the respective atom concentration $n_a(r, L)$ can be calculated, using Saha equation, plasma quasineutrality condition and law of partial pressures [13].

We will present the heat flux from the plasma to the anode surface as follows: $q_{pa} = q_e + q_i$, where q_e, q_i are the flows of kinetic and potential energy, transferred by electrons and ions of plasma, respectively. To calculate the radial distributions of the above quantities, we will use expressions [12], which in the case of a nonevaporating anode can be written in the following form:

$$q_e(r) = j_e(r) \frac{5kT(r,L)}{2e}; \tag{9}$$

$$q_i(r) = j_i(r) \left[\varphi_{pa}(r) + \frac{1}{2} \frac{kT_s}{e} + U_i \right]. \tag{10}$$

Here,

$$j_e(r) = \frac{1}{4} e n_e (r,L) \upsilon_e (r,L) \exp \left[-\frac{e \varphi_{pa}(r)}{kT(r,L)} \right]$$

is the electron current from the plasma to the anode surface; U_i is the ionisation potential of shielding gas atoms. It should be noted that the distribution of the full heat flux into the anode should be calculated, allowing for electron work function ζ_a that yields:

$$q_a(r) = q_{pa}(r) + j_a(r)\zeta_a. \tag{11}$$

Thus, the proposed model of the arc anode boundary layer allows calculation of the distributions of the anode potential drop $U_a(r)$ and density $q_a(r)$ of the heat flux introduced into the anode, depending on the kind of shielding gas, distributions of anode current density and arc column plasma temperature on the interface with the anode boundary layer, as well as anode surface temperature T_s. In its turn, the distributions of $j_a(r)$ and $T(r, L)$ quantities can be determined, proceeding from the arc column model with self-consistent boundary conditions on the anode.

In completion of the description of anode boundary layer model, we will note that its application in the case of a nonstationary arc requires allowing for the dependencies of all the quantities, included into relationships (8)–(11), not only on radial coordinate r, but also on time t. Estimating the relaxation time of the anode boundary layer characteristics using relationship $\tau_a \sim / l_a / \upsilon_e$, where l_a is the layer thickness, υ_e is the thermal velocity of electrons, the values of which for atmospheric pressure argon arc are equal to $5 \cdot 10^{-4}$ m and $5 \cdot 10^5$ m/s, respectively [14], we obtain $\tau_a \sim 10^{-9}$ s, that is much smaller than the time for the change of arc column plasma characteristics $\tau_p \sim 10^{-4}$ s [15] and the period of current change at the considered modulation frequency. Thus, the above-given relationships are quite applicable to the description of anode processes running in the considered arc, allowing for the fact that the included into them distributed characteristics of arc plasma on the interface with the anode boundary layer appropriately depend on time.

INITIAL AND BOUNDARY CONDITIONS FOR A NONSTATIONARY ARC MODEL

Appropriate initial and boundary conditions should be assigned to solve the system of differential equations (1)–(5), describing nonstationary processes of heat-, mass- and charge transfer in the arc column. As the fields of arc plasma temperature and velocity are set fast enough (as shown by calculations [16], 6–8 pulses are sufficient in order to achieve a periodical change of characteristics of the above-mentioned fields at about 10 kHz frequency of arc current pulsed modulation), initial distributions of plasma velocity and temperature are of no fundamental importance. For instance, zero values can be set for velocity components, and plasma temperature in the current channel area should be selected so as to ensure the plasma conductivity characteristic for an argon arc.

In the case considered here of a nonstationary arc with the tungsten cathode and water-cooled (nonevaporating) anode, we will formulate boundary conditions for sought functions (v, u, P, T, φ) as follows.

Near the cathode (plane $z = 0$ in Figure 1) the conditions for the components of the velocity vector are set as follows:

$$v|_{z=0} = 0; \quad u|_{z=0} = \begin{cases} u\ , 0 \le r < R\ ; \\ 0, R\ \le r \le R, \end{cases} \tag{12}$$

where quantity u_0 is determined by shielding gas flow rate and radius R_1 of its feeding nozzle (see Figure 1).

For temperature and electric potential in the zone of cathode attachment of a nonstationary arc (at $0 \le r \le R_c$, $z = 0$) we will take the following conditions

$$T|_{z=0} = T_c(r,t); \quad \sigma \left.\frac{\partial \varphi}{\partial z}\right|_{z=0} = j_c(r,t), \tag{13}$$

where $T_c(r, t)$, $j_c(r, t)$ are the radial distributions of plasma temperature and current density near the cathode, changing in time at arc current modulation, the explicit form of which, following [17], is set as follows:

$$j_c(r,t) = j_{c0}(t)\frac{1}{2} erfc\left\{\frac{10\left[r - r_{0c}(t)\right]}{r_{0c}(t)}\right\} \tag{14}$$

and similarly for $T_c(r, t)$, taking into account the fact that shielding gas temperature is equal to ambient temperature T_0 outside the region of cathode attachment of the arc ($r > R_c$). Here, $j_{c0}(t)$ is the axial value of current density; $erfc(x) = \frac{2}{\sqrt{\pi}} \int\limits_x^\infty e^{-y^2} dy$; $r_{0c}(t)$ is the distance from the arc axis, where current density drops two times.

Estimating the time for setting of cathode layer characteristics τ_c using relationship $\tau_c \sim L_c / \overline{\upsilon}_e$ where L_c is the layer thickness, $\overline{\upsilon}_e$ is the mean thermal velocity of electrons in this layer, the values of which we will select equal to $3 \cdot 10^{-4}$ m and $1.2 \cdot 10^6$ m/s in the case of atmospheric pressure argon arc with a tungsten cathode [18], we will obtain $\tau_c \sim 2.5 \cdot 10^{-10}$ s. As this time is much shorter than the period of arc current variation at modulation frequency $f = 10$ kHz, we will assume that radial distributions of current density and plasma temperature near the cathode completely follow the change of arc current at considered f value. Thus, we will assign the axial values of current density $j_{c0}(t)$ and near-cathode plasma temperature $T_{c0}(t)$ at each moment of time according to recommendations of work [17], depending on the instantaneous value of arc current, determined by the law of its modulation $I(t)$. Selecting radius $R_c(t)$ of the zone of cathode attachment of the arc (see Figure 1) as the distance from its axis, at which current density is less than 1 %

of j_{c0} at the respective moment of time, and allowing for (14), we have $R_c(t) = 1.165r_{0c}(t)$. Here, the time dependence of quantity r_{0c} can be found from the integral relationship for total current.

$$I(t) = 2\pi \int_0^{\infty} r j_c(r,t)dr. \tag{15}$$

Outside the zone of cathode attachment of the arc (at $R_c < r \le R$, $z = 0$) we assume:

$$T|_{z=0} = T_0; \quad \left.\frac{\partial \varphi}{\partial z}\right|_{z=0} = 0. \tag{16}$$

On the anode surface (plane $z = L$ in Figure 1) we accept the "sticking" conditions

$$v|_{z=L} = u|_{z=L} = 0. \tag{17}$$

On the interface of arc column plasma with the anode boundary layer, or considering the assumption made of its infinitely small thickness, at $z = L$, the following condition of energy balance can be used as the boundary condition:

$$\begin{gathered} \left[-\chi\frac{\partial T}{\partial z} + |j_z|\frac{k}{e}\left(\frac{5}{2} - \delta\right)T\right]\Bigg|_{z=L} = \\ = \varphi_{pa}(r,t)\, j_a(r,t) + q_{pa}(r,t). \end{gathered} \tag{18}$$

As the electric potential of the anode surface is assumed to be constant and equal to zero, the boundary condition for plasma potential on the interface of the arc column with the anode boundary layer can be written as follows:

$$\varphi|_{z=L} = \varphi_{pa}(r,t). \tag{19}$$

Boundary conditions for plasma velocity, temperature and electric potential on the axis of system symmetry are set in a standard way

$$v|_{r=0} = 0; \ \left.\frac{\partial u}{\partial r}\right|_{r=0} = \left.\frac{\partial T}{\partial r}\right|_{r=0} = \left.\frac{\partial \varphi}{\partial r}\right|_{r=0} = 0. \tag{20}$$

On the outer boundary of the calculated region ($r = R$) for plasma velocity and electric potential we can write

$$\left.\frac{\partial(\rho v r)}{\partial r}\right|_{r=R} = 0; \quad u|_{r=R} = 0; \quad \left.\frac{\partial \varphi}{\partial r}\right|_{r=R} = 0. \tag{21}$$

We will determine the boundary condition for plasma temperature at $r = R$, depending on the flow direction

$$\begin{gathered} T|_{r=R} = T_0, \text{ at } v|_{r=R} \le 0; \\ \left.\frac{\partial T}{\partial r}\right|_{r=R} = 0, \text{ at } v|_{r=R} > 0. \end{gathered} \tag{22}$$

The system of differential equations (1)–(5) with above-described initial and boundary conditions was solved numerically, by the method of finite differences, using the joint Euler–Lagrange method, adapted to the conditions of the compressible medium. Calculated data from works [19, 20] were used to determine the temperature dependencies of thermodynamic characteristics, transport coefficients and losses of energy for arc plasma radiation, included into the model equations.

SIMULATION RESULTS

As the object of numerical study, we will select a nonstationary arc with a refractory cathode, burning under the conditions characteristic for HFPC TIG welding. We will assume that arc current $I(t)$ is unipolar ($I(t) \ge 0$), and its modulation is performed by rectangular pulses in the range of $I_1 < I(t) < I_2$, where I_1 is the pause current; I_2 is the pulse current (modulation amplitude $A = I_2 - I_1$), with pulses following with frequency f (modulation period $T_m = 1/f$) at different values of duty cycle δ, characterizing the ratio of pulse duration to modulation period. Average I_{av} and effective I_{eff} values of arc current can be determined as follows:

$$I_{av} = \langle I(t) \rangle; \ I_{eff} = \sqrt{\langle I^2(t) \rangle},$$

where

$$\langle \phi(t) \rangle = \frac{1}{T_m} \int_0^{T_m} \phi(t)\, dt$$

is the integral mean value of periodic function $\phi(t)$ in interval $t \in [0; T_m]$.

We will consider a nonstationary arc of length $L = 2$ mm with a refractory cathode and water-cooled (nonevaporating) anode, burning in atmospheric pressure argon, at the following parameters of HFPC modulation: frequency $f = 10$ kHz ($T_m = 100$ μs); duty cycle δ = 0.3; 0.5 (meander); 0.7; pause current $I_1 = 30$ A, and we will determine the respective value of pulse current I_2 from the condition that average value of arc current I_{av} remains constant and equal to 140 A at all values of δ. The obtained values of I_2, A, I_{eff} are given in Table 1.

Results of calculation of the distributed and integrated characteristics of the considered arc and its impact of the anode surface at the given parameters of current modulation were compared with the calculated values of the respective characteristics of a DC arc, at current equal to average value of modulated current.

Figure 2 shows the change in time of arc plasma temperature T_0, its velocity u_0 and current density $j_0 = |j_{0z}|$ on the arc column axis ($r = 0$) in section $z = 1$ mm (midpoint of arc length). In these figures and further on the solid curves marked by numbers 1, 2, 3, correspond to duty cycles δ = 0.3; 0,5; 0.7; dashed

Table 1. Parameters of arc current modulation

δ	I_2, A	A, A	I_{eff}, A
0.3	396.7	366.7	218.7
0.5	250.0	220.0	178.0
0.7	187.1	157.1	157.4

lines are the respective values for DC arc (I = 140 A); time is counted from the beginning of the pause.

Calculations show that under the considered conditions, values T_0, u_0 and j_0 turn out to be significantly greater during the current pulse, than during the pause, and the more so, the smaller is the duty cycle δ and the higher is the pulse current value I_2, respectively.

After the pulse impact is over, cooling of arc column plasma occurs due to the dissipative mechanism of energy transfer, so that value T_0 decreases continuously during the entire pause duration. Characteristic time of relaxation of arc plasma temperature in the pause for the selected parameters of current modulation is equal to the value of the order of 30 μs (see Figure 2, *a*). At the pulse leading edge the plasma is heated by Joule heat source, which almost instantly reacts to a change of arc current. Here, in the case of small δ values (high values of pulse current), plasma temperature in the column center rises abruptly to values, exceeding the respective values for a DC arc, with current I_2, and then smoothly decreases during the time of the order of 20 μs (see curve 1 in Figure 2, *a*).

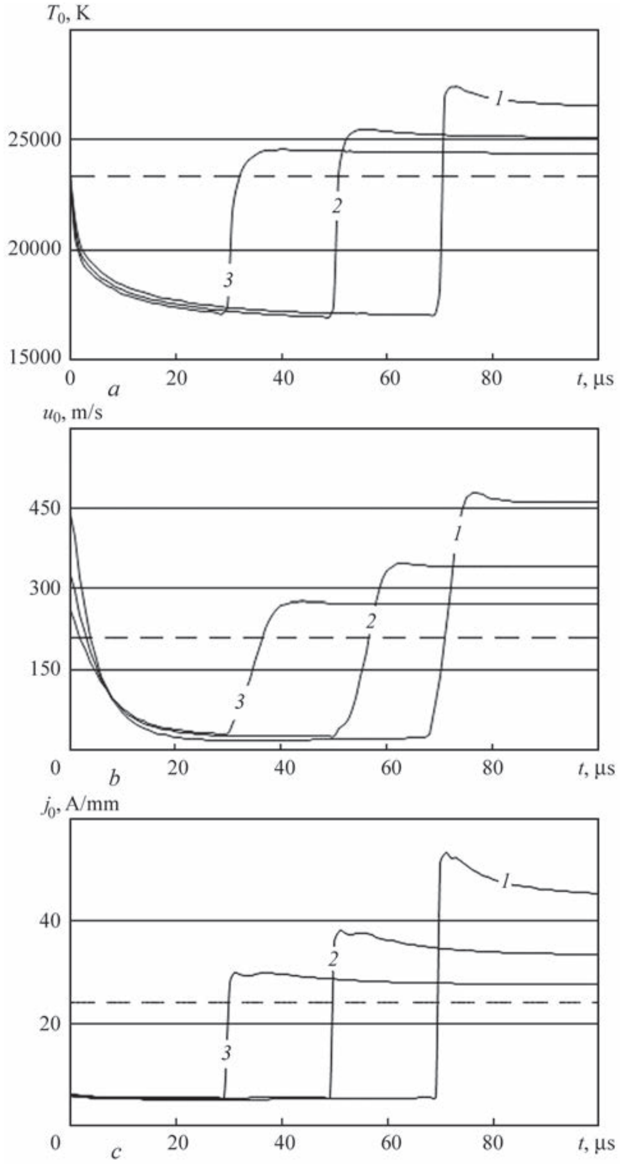

Figure 2. Time dependencies of plasma temperature (*a*), axial components of velocity (*b*) and current density (*c*) in the arc column center

A similar pattern is observed also for the velocity of plasma in the center of arc column (see Figure 2, *b*), except for value u_0 growing slower than temperature at instantaneous rise of current on the pulse leading edge. This is associated with the inertia of gas-dynamic processes in arc plasma [15]. As regards the change in time of current density in the arc column center, it decreases almost instantly at current drop on the pulse trailing edge and grows, accordingly, on the leading edge (see Figure 2, *c*). Note that at small values of δ, behaviour of values u_0 and j_0 at transition from the pause to the pulse corresponds to the above described extreme behaviour of arc plasma temperature with subsequent relaxation (see curves *1* in Figure 2, *a*–*c*).

We will analyze the characteristics of thermal, force and electromagnetic impact of the considered arc on the anode surface. Figure 3 shows the time dependencies of axial values of temperature T_{a0} of arc plasma column on the interface with the anode boundary layer, overpressure P_{a0} and current density j_{a0} on the anode surface, as well as the heat flux introduced by the arc into the anode q_{a0}.

Quantity T_{a0} behaves similar to plasma temperature in the arc column center, at significantly smaller values both during the pause, and during the pulse (compare Figures 2, *a* and 3, *a*). As overpressure can be presented as a sum of magnetic pressure P_m and pressure P_v due to plasma motion [15], analysis of time dependence of value P_{a0} should be performed, allowing for this circumstance. Axial value of magnetic pressure, dependent on radial distribution of current density, changes almost instantly on the pulse leading and trailing edges, reacting to the respective changes of arc current. As regards to pressure due to plasma motion, its change occurs slower, which is associated with the above-noted inertia of gas-dynamic processes in arc plasma. It leads to a two-stage change in the axial value of aggregated overpressure on the anode surface: almost instant at the first stage and slower at the second one, with characteristic relaxation time of about 10 μs during the pulse (see Figure 3, *b*).

Dynamics of the change in time of axial values of anode current density and heat flux into the anode is shown in Figure 3, *c*, *d*. Unlike the respective values

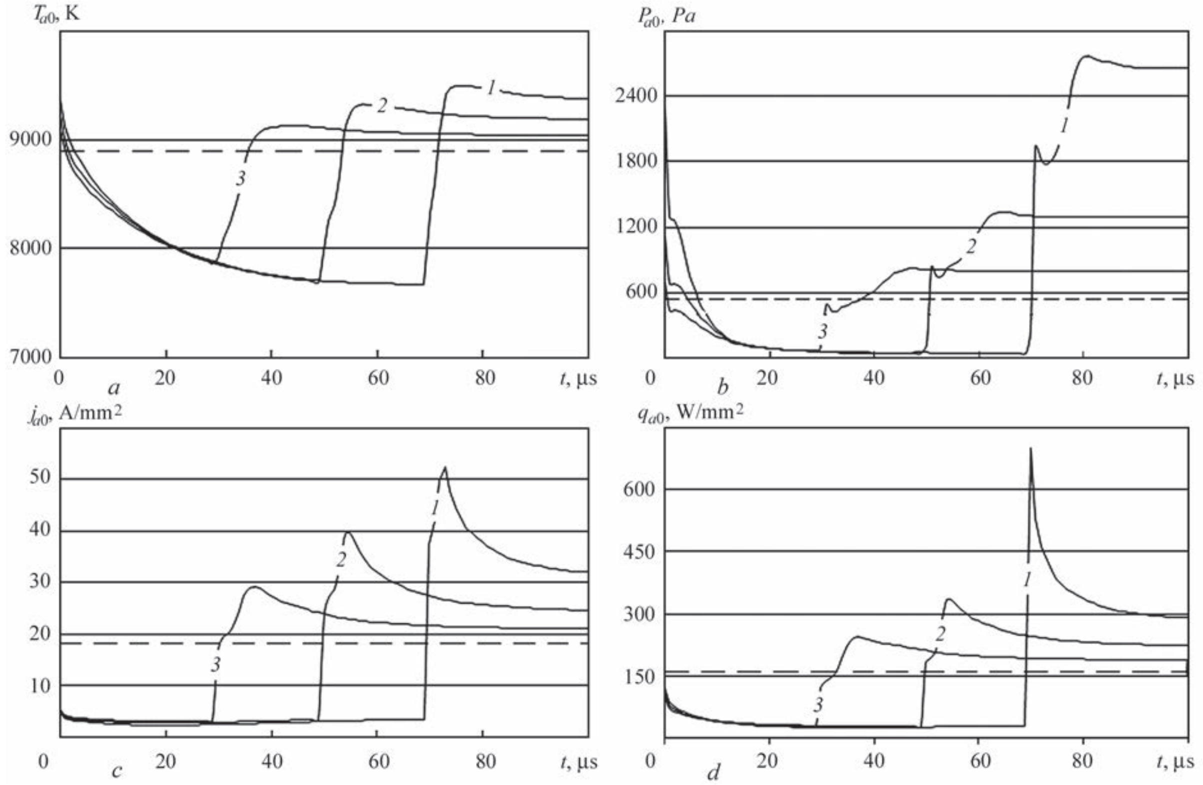

Figure 3. Time dependencies of axial values of arc plasma temperature on the interface with the anode boundary layer (*a*), overpressure (*b*) and current density (*c*) on the anode surface, as well as heat flux into the anode (*d*)

of arc plasma temperature and overpressure near the anode surface, value j_{a0} falls quickly enough on the pulse trailing edge and remains practically constant during the pause (compare Figure 3, *a*–*c*). At pulse feeding, increase of the mentioned value (similar to axial overpressure on the anode surface) occurs in two stages. At the first stage current density on the axis of the arc anode attachment rises abruptly, as at feeding of the pulse high current flows through the current channel of a small cross-section, initially remaining after the pause. At the second stage restructuring of radial distribution of plasma temperature and, hence, of its electric conductivity, takes place through convective-conductive energy transfer in arc column plasma, leading to further, slower increase of quantity j_{a0}. As a result, for all the considered duty cycles, the axial value of current density on the anode surface rises up to values, significantly exceeding the respective values for a DC arc, with current equal to I_2, and then it relaxes to them with the characteristic time of the order of 20 μs (see Figure 3, *c*). As the specific heat flux into the anode is practically proportional to anode current density [14], the change of value q_{a0} in time is similar to the change of axial value of current density on the anode surface (see Figure 3, *c*, *d*).

We will consider radial distributions of thermal, force and electromagnetic impact of a nonstationary arc on the anode surface. In study [15] it is shown

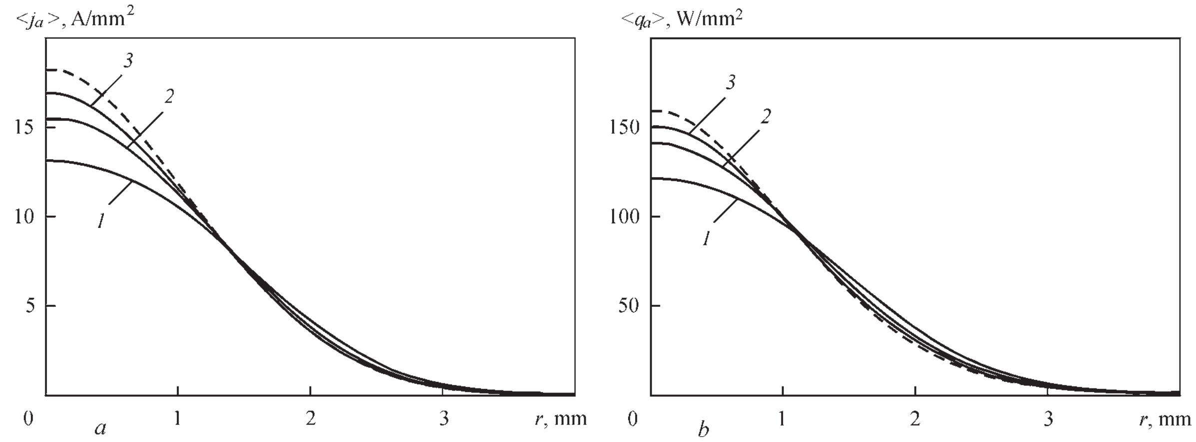

Figure 4. Radial distributions of averaged over the modulation period values of current density on the anode surface (*a*) and heat flux into the anode (*b*)

Table 2. Full heat flux into the anode

δ	$\langle Q_a\rangle$, W
0.3	1261
0.5	1212
0.7	1183
DC mode	1141

that at TIG welding with high-frequency ($f \sim 10$ kHz) pulsed modulation of current, the thermal and force impact of the arc on the surface of the metal being welded (radial distributions of heat flux into the anode and overpressure of arc plasma on its surface) can be regarded as averaged over the modulation period, as the characteristic time of the change of metal temperature and velocity in the weld pool is equal to a value of the order of 10^{-2} s, that is two orders of magnitude greater than the period of current modulation with the specified frequency.

Figure 4 gives radial distributions of anode current density $\langle j_a(r, t)\rangle$ and heat flux$\langle q_a(r, t)\rangle$, introduced into the anode, averaged over the period of arc current modulation. Respective radial distributions of magnetic pressure $\langle P_m(r, t)\rangle$ and pressure due to arc plasma motion $\langle P_v(r, t)\rangle$ on the anode surface are shown in Figure 5.

Unlike the considered above extreme change of instantaneous values of current density on the anode surface, and heat flux into the anode on the axis of the region of the arc anode attachment (see Figure 3, *c*, *d*), the dependencies given in Figure 4 demonstrate an opposite tendency, namely averaged axial values of current density and heat flux into the anode decrease at reduction of duty cycle δ. Moreover, they remain smaller than the respective values of j_{a0} and q_{a0} for a DC arc, with current equal to average value of modulated current. This is associated with the fact that at δ decrease the pause duration becomes greater, during which the anode current density and the heat flux into the anode are much lower than the respective values for an equivalent DC arc (see Figure 3, *c*, *d*).

According to the data, presented in Table 2, the averaged value of total heat flux into the anode $\left\langle Q_a\right\rangle = 2\pi\int\limits_0^\infty \left\langle q_a(r,t)\right\rangle rdr$ unlike $\langle q_{a0}(t)\rangle$, rises at decrease of δ (at increase of pulse current) and constant average current. This feature is related to a change of filling of the profiles $\langle q_a(r, t)\rangle$, depending on the duty cycle (see Figure 4, *b*).

As regards electromagnetic impact of the arc with HFPC modulation on weld pool metal, it can also be considered as an averaged value over the modulation period [15], allowing for the fact that the expression for Lorenz force $\vec{F} = \mu^0 \vec{j} \times \vec{H}$ setting the molten metal into motion, is quadratic in current density $\vec{j}$ (magnetic field intensity $\vec{H}$). Therefore, in order to determine the spatial distribution of averaged value of electromagnetic force, it is necessary to find the distributions of the above-mentioned values at each moment of time, using the distribution of electric current density on the anode surface at the respective moment of time, then calculate the instantaneous values of $\vec{F}$ (r, z, t) and only then average over time. Here, $j_a(r, t)$ distributions should be used instead of $\langle j_a(r, t)\rangle$ distribution given in Figure 4, *a*.

Comparison of the thus calculated averaged electromagnetic force $\langle F_{mz}(r, z, t)\rangle$ in the case of the considered high-frequency ($f = 10$ kHz) current modulation by rectangular pulses in the form of a meander ($\delta = 0.5$) and the respective force for an equivalent DC arc shows that the magnitude of this force in the first case turns out to be approximately 1.5 times greater than in the second case [15], and it increases at δ reduction. As this force causes molten metal motion towards the weld pool bottom, the penetrability of the arc with HFP modulation of current should become greater with decrease of the duty cycle (with I_2 increase) while maintaining I_{av}.

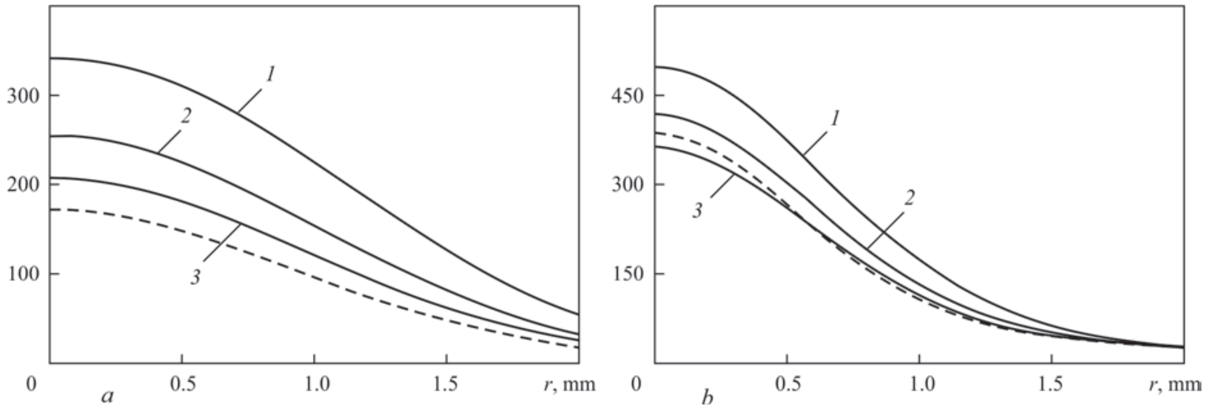

Figure 5. Radial distributions of averaged over the modulation period magnetic pressure (*a*) and pressure due to arc plasma motion (*b*) on the anode surface

As follows from the calculated data, presented in Figure 5, the averaged magnetic pressure near the surface of the anode of a nonstationary arc turns out to be significantly higher than the respective magnetic pressure for an equivalent DC arc, increasing with reduction of δ (see Figure 5, *a*). Pressure due to arc plasma motion on the anode surface, averaged over the current modulation period, also becomes higher at decrease of the duty cycle. However, its values at $\delta > 0.6$ are lower than the respective values for a DC arc at 140 A current. Average value of aggregate overpressure near the anode surface, which is a sum of $\langle P_m(r, t)\rangle$ and $\langle P_v(r, t)\rangle$ for a nonstationary arc under the considered conditions of current modulation, is higher than the overpressure of a DC arc that corresponds to the results of experimental measurement of the above quantity in [5].

Note that at determination of the shape of weld pool free surface only value P_v should be used as an essential component of arc plasma overpressure in the balance of normal stresses on the above-mentioned surface, as magnetic pressure P_m does not experience a jump when passing through arc plasma-metal interface [15]. As was already mentioned, in the case of HFPC modulation, quantity $\langle P_v(r, t)\rangle$, determining the depression of the weld pool surface, increases with δ reduction (with increase of pulse current) at constant value of average current. It promotes deeper immersion of such an arc into the metal being welded and increase of its penetrability, respectively, at I_2 increase and maintenance of the same I_{av}.

An important force factor, determining the hydrodynamic situation in the weld pool in TIG welding (alongside Lorentz and Marangoni forces) is the force of viscous friction of arc plasma flow against the anode metal surface. In the case of HFPC modulation ($f = 10$ kHz), the above-mentioned force, similar to P_v, can be considered as averaged over the modulation period [15]. Radial distribution of tangential stress $\langle S_v(r, t)\rangle$, generated by this force, is illustrated in Figure 6.

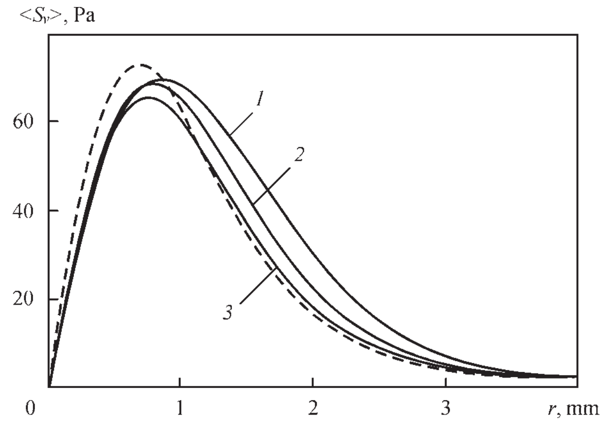

Figure 6. Radial distributions of averaged over the modulation period tangential stress, generated by the force of friction of the plasma flow on the anode surface

Calculated data given in Figure 6 shows that compared to S_v distribution for an equivalent DC arc, the maximum of averaged value of arc plasma viscous friction on the anode surface at HFPC modulation somewhat decreases in magnitude at increase of the duty cycle, and its position shifts towards smaller values of r. This is indicative of a weak effect of current modulation on the force of viscous friction of the arc plasma flow against the weld pool surface in HFPC TIG welding.

CONCLUSIONS

Performed numerical analysis of thermal, gas-dynamic and electromagnetic characteristics of arc plasma, as well as its impact on the anode surface, under the conditions characteristic for TIG welding with arc current modulation by rectangular pulses of different duration and amplitude (at constant value of average arc current), following at 10 kHz frequency, leads to the following conclusions:

1. At the considered modulation parameters, the current density in the arc column plasma almost instantly reacts to changes of the arc current, whereas the temperature and velocity of arc plasma have greater inertia, with the characteristic setting time of about 20 μs in the pulse and about 30 μs at transition from the pulse to the pause. Here, the values of the above-mentioned parameters are considerably higher during the pulse, that during the pause, and they are the greater, the smaller the duty cycle (the higher the pulse current).

2. Axial values of current density on the anode surface and heat flux to the anode, averaged over the period of arc current modulation, decrease at reduction of the duty cycle for the considered modulation conditions. Moreover, they remain smaller than the respective values for a DC arc at current equal to average value of modulated current. Here, the full heat flux into the anode, contrarily, is greater than the respective value for an equivalent DC arc, increasing with reduction of the duty cycle (with increase of pulse current).

3. Pressure on the anode surface due to arc plasma motion, averaged over the current modulation period, increases with reduction of the duty cycle and at $\delta < 0.6$ it becomes greater than the respective pressure for a DC arc at current equal to average value of modulated current. As a result, shortening of the pulse duration and the respective increase of current modulation amplitude in welding by an arc with a refractory cathode leads to increase of the depression of weld pool surface that promotes deeper immersion of the arc into the metal being welded and increase of its penetrability. As regards the force of viscous friction of arc plasma flow driving the surface layers of weld pool metal from its center to the

periphery, thus increasing the width of the penetration zone by reducing its depth, it practically does not differ from the respective force applied to the melt surface by plasma of an equivalent DC arc.

4. Evaluation of an averaged force impact of the considered nonstationary arc on the welded metal melt is indicative of a considerable increase (compared to an equivalent DC arc) of the volume electromagnetic force, driving the melt and causing the convective heat transfer from the surface towards the weld pool bottom, that also promotes greater penetration depth in HFPC TIG welding.

ACKNOWLEDGMENTS

This work was carried out with the financial support of the German Research Foundation DFG Project No. 390246097/RE2755/51-1 “Investigation of the influence of non-stationary processes in the arc plasma on the penetration depth during high frequency TIG welding”. The authors wish to express their thanks for this funding.

REFERENCES

1. (2011) Welding fundamentals and processes. Ed. by T.J. Lienert, S.S. Babu et al. ASM Handbook, Ohio, USA. ASM Int.
2. Leither, R.E., McElhinney, G.H., Pruitt E.L. (1973) An investigation of pulsed GTA welding variables. *Welding J., Res. Suppl*., **9**, 405s–410s.
3. Omar, A.A., Lundin, C.D. (1979) Pulsed plasma-pulsed GTA arcs: A study of the process variables. *Welding J., Res. Suppl*., **4**, 97s–105s.
4. Saedi, H.R., Unkel, W. (1988) Arc and weld pool behavior for pulsed current GTAW. *Welding J., Res. Suppl*., **11**, 247s–255s.
5. Onuki, J., Anazawa, Y., Nihei, M., et al. (2002) Development of a new high-frequency, high-peak current power source for high constricted arc formation. *Japan J. Appl., Phys*., **41**, 5821–5826.
6. Karunakaran, N., Balasubramanian, V. (2011) Effect of pulsed current on temperature distribution, weld bead profiles and characteristics of gas tungsten arc welded aluminum alloy joints. *Transact. Nonferrous Met. Soc. China*, **21**, 278–286.
7. Cunha, T.V.d., Louise-Voigt, A., Bohorquez, C.E.N. (2016) Analysis of mean and RMS current welding in the pulsed TIG process. *J. of Materials Proc. Technology*, **231**, 449–455.
8. Silva, D.C.C., Scotti, A. (2017) Using either mean and RMS values to represent current in modeling of arc welding bead geometries. *J. of Materials Proc. Technology*, **240**, 382–387.
9. Kim, W.H., Na, S.J. (1998) Heat and fluid flow in pulsed current GTA weld pool. *Int. J. of Heat and Mass Transfer*, Vol. 41(Issue 21), 3213–3227.
10. Wu, C.S., Zheng, W., Wu, L. (1999) Modeling the transient behaviour of pulsed current tungsten-inert-gas weld pools. Modelling and Simul. *Mater. Sci. Eng*., 7(**1**), 15–23.
11. Traidia, A., Roger, F., Guyot, E. (2010) Optimal parameters for pulsed gas tungsten arc welding in partially and fully penetrated weld pools. *Int. J. of Thermal Sci*., **49**, 1197–1208.
12. Krivtsun, I., Demchenko, V., Krikent, I. et al. (2015) Distributed and integrated characteristics of the near-anode plasma of the welding arc in TIG and Hybrid (TIG + CO_2 Laser) welding. In: *Mathematical Modelling of Weld Phenomena 11*. Techn. Universitat Graz, Graz, Austria, 837–874.
13. Krivtsun, I., Demchenko, V., Lesnoi, A. et al. (2010) Modelling of electromagnetic processes in system “welding arc–evaporating anode”. Pt 1: Model of anode region. *Sci. and Technol. of Welding & Joining*, 15(**6**), 457–463.
14. Semenov, I.L., Krivtsun, I.V., Reisgen, U. (2016) Numerical study of the anode boundary layer in atmospheric pressure arc discharges. *J. Phys. D: Appl. Phys*., 49(**10**), 105204.
15. Demchenko, V.F., Boi, U., Krivtsun, I.V., Shuba, I.V. (2017) Effective values of electrodynamic characteristics of the process of nonconsumable electrode welding with pulse modulation of arc current. *The Paton Welding J*., **8**, 2–11. DOI: https://doi.org/10.15407/tpwj2017.08.01
16. Sydorets, V.N., Krivtsun, I.V., Demchenko, V.F. et al. (2016) Calculation and experimental research of static and dynamic volt-ampere characteristics of argon arc with refractory cathode. *The Paton Welding J*., **2**, 2–8.
17. Wendelstorf, J., Simon, G., Decker, I. et al. (1997) Investigation of cathode spot behavior of atmospheric argon arcs by mathematical modeling. In: *Proc. of the 12th Int. Conf. on Gas Discharges and their Applications (Germany, Greifswald, 1997)*, Vol. 1, 62–65.
18. Benilov, M.S., Marotta, A. (1995) A model of the cathode region of atmospheric pressure arcs. *J. Phys. D: Appl. Phys*., Vol. 28, 1869–1882.
19. Cressault, Y., Murphy, A.B., Teulet, Ph. et al. (2013) Thermal plasma properties for Ar–Cu, Ar–Fe and Ar–Al mixtures used in welding plasma processes: II . Transport coefficients at atmospheric pressure. *J. Phys. D: Appl. Phys.*, Vol. 46, 415207.
20. Essoltani, A., Proulx, P., Boulos, M.I. et al. (1994) Volumetric emission of argon plasma in the presence of vapours of Fe, Si and Al. *Plasma Chem. and Plasma Proc*., 14(**4**), 437–450.

ORCID

I. Krivtsun: 0000-0001-9818-3383
I. Krikent: 0000-0002-4196-6800
U. Reisgen: 0000-0003-4920-2351
O. Mokrov: 0000-0002-9380-6905
R. Sharma: 0000-0002-6976-4530

CONFLICT OF INTEREST

The Authors declare no conflict of interest

CORRESPONDING AUTHOR

I. Krivtsun
E.O. Paton Electric Welding Institute of the NASU
11 Kazymyr Malevych Str., 03150, Kyiv, Ukraine
E-mail: krivtsun@paton.kiev.ua

SUGGESTED CITATION

I. Krivtsun, V. Demchenko, I. Krikent, U. Reisgen, O. Mokrov, R. Sharma (2022) Characteristics of HFPC arc with refractory cathode. *The Paton Welding J*., **3**, 9–18.

JOURNAL HOME PAGE

https://pwj.com.ua/en

Received: 13.04.2022
Accepted: 16.05.2022

https://doi.org/10.37434/tpwj2022.03.02

EFFECT OF PARAMETERS OF PULSED-ARC WELDING ON THE FORMATION OF WELD METAL AND MICROSTRUCTURE OF HEAT-AFFECTED ZONE OF 09G2S STEEL

S.Yu. Maksymov, D.M. Krazhanovskyi, Yu.A. Shepelyuk, S.V Osynska

E.O. Paton Electric Welding Institute of the NASU
11 Kazymyr Malevych Str., 03150, Kyiv, Ukraine

ABSTRACT

One of the promising ways to solve the problem of increasing the service life of welded structures is the development of welding methods based on the use of pulsed control of energy parameters of the process. The pulsed mode of welding allows performing a regulated heat input in the welded butt joint zone, controlling the mode of melting the electrode metal, forming the structure of weld metal and heat-affected zone (HAZ). It was found that with an increase in the frequency of pulsed-arc welding, it is possible to reduce the width of the HAZ and the region of a coarse grain. Thus, in the case of welding low-alloy steels, due to the use of technology with a pulsed process, there is a prospect of reducing the width of the overheating region, which is important for the cases of repair of pipe wall thinning during remelting of defects in the operating pipeline using a mechanized method.

KEYWORDS: main pipelines, pulsed-arc welding, technological parameters, welded joint, geometric parameters, structure

INTRODUCTION

At present, oil and gas-oil equipment and main pipelines become objects of increased danger because of their technical condition. This circumstance causes the need in using effective methods of repair. With the help of traditional welding methods, it is difficult to solve all technological problems that are complicated: providing the possibility of regulating penetration depth in a wide range, welding over increased gaps and in different spatial positions, joining of metals and alloys dissimilar in their composition, reduction of sputtering of electrode metal, increase in the stability of arc ignition and its burning [1].

The main problem in welding of position butt joints of main pipelines is to provide the necessary quality of root, filling and facing layers and a high level of mechanical characteristics in a butt to be welded. It is known that up to 90 % of defects revealed during testing of the quality of welded joints, are associated with defects in the root layers of welds: undercuts, lacks of penetration, nonmetallic inclusions, pores [2]. The main cause for appearance of these defects, except for a poor preparation of a butt to be welded, is a violation of welding conditions (welding speed, arc voltage, current), as well as their inconsistency with the necessary values that provide producing high-quality welded joints. Traditionally, the used processes of manual welding can provide the necessary quality of welded joints only during a careful preparation of a butt to be welded and the use of high-quality materials.

The gained experience shows that pulsed methods of welding process control allow solving the following technological problems:

- controlled and directed transfer of electrode metal [3–5];
- possibility of welding in all spatial positions and simplification of welding techniques [6, 7];
- improvement of quality of welded joints due to the greater concentration of the power of the heating source and the better conditions of primary crystallization [5, 8, 9];
- reduction of losses on burn and sputtering [4, 10].

The analysis of literature showed that at a pulsed feeding the weld structure is fine-grained and disoriented, and the mechanical properties of welded joints are higher than in welding with short circuits of an arc gap [11–13]. The application of pulses allows a significant increase in the intensity and stability of arc discharge, the hydrodynamic processes in the welding pool and the conditions of its crystallization are changing. The pulsed increase in the pressure of the arc improves the formation of the weld, the weld bead becomes fine-rippled and refining of the microstructure associated with the collision impact of electrode metal droplets is observed [14–16].

The aim of the carried out investigations was to determine the impact of welding and frequency f of the process of pulsed-arc welding on geometric dimensions of the deposits and structural transformations in the HAZ.

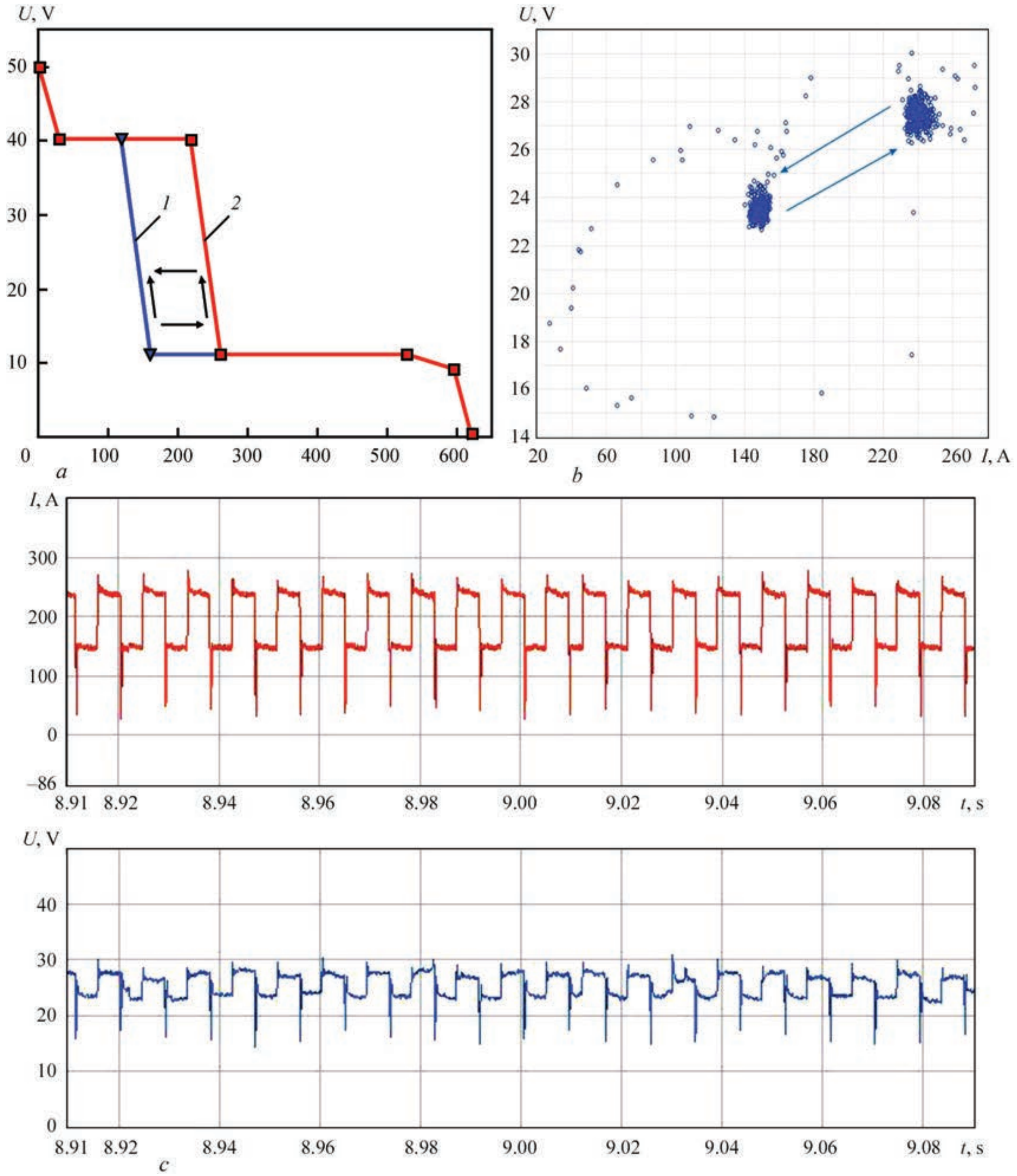

Figure 1. Combination of VACh of power source for realization of a pulsed process of welding (*a*): *1*, *2* — respectively, pause and pulse current; dynamic VACh (*b*) and oscillogram of the process (*c*)

PROCEDURE OF EXPERIMENT

To realize the set task, the power source LET-500 was used. Using additional software, a very flexible adjustment of most of the power source parameters can be performed, including the shape of the output volt-ampere characteristics. The pulsed mode of the source operation allows operating on two such VACh indicating the time of operation of each one (Figure 1, *a*). The falling regions of VACh (*1* and *2*) correspond to the pause and pulse current. During switching between the characteristics, the value of the welding current varies to the corresponding value for the actual characteristic (Figure 1, *b*, *c*).

For the first part of the experiments, the families of volt-ampere characteristics VACh No.1 and VACh No.2 were selected (Figure 2, *a*). The main difference between the families was in a gradual increase in the pause current, shifting the falling area *1* to the left (curve *1*) (VACh No.1). In this case, the position of the curve *2* (VACh No.2) remained unchanged.

In the work, the pulsed-arc process with a frequency $f = 100$ Hz and a duty cycle $C = 2$ was used. The input energy Q for each experiment (Table 1) was calculated by the formula:

$$Q = \frac{60 I_{\text{mean}} U_{\text{mean}}}{v_{\text{w}}} \eta,$$

where v_{w} is the welding speed (m/h), $\eta = 0.7$; I_{mean} is the mean welding current, which is calculated by the

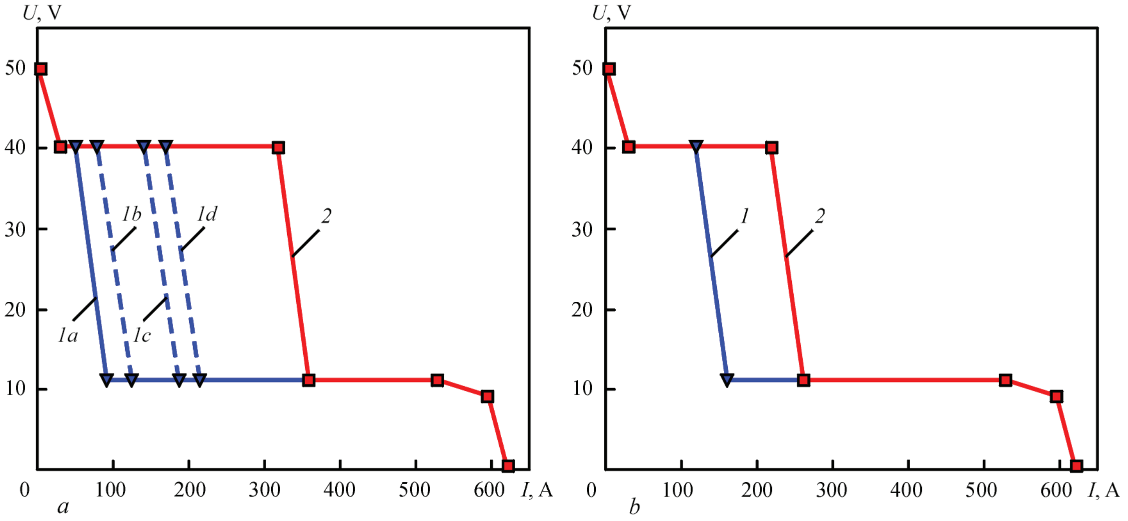

Figure 2. VACh family for PAW performance in order to determine the dependence of geometric dimensions *b*, *h* from: *a* — welding modes I_{mean}, U_{mean}; *b* — frequency *f* of the process (description *1*, *2* see in the text)

formula known for pulsed-arc processes, namely, $I_{mean} = (I_{pulse}\, t_{pulse} + I_{pause}\, t_{pause})/(t_{імпульсу} + t_{pause})$.

In order to determine how frequency *f* of the pulsed-arc process that occurs with short-circuits, affects the geometric characteristics *h* and *b*, the experimental studies were conducted. For this purpose, to the pulsed power source, VACh No.1 and VACh No.2 were introduced (Figure 2, *b*), the welding speed was v_w = 30 cm/min, the feed of welding wire was v_{wire} = 6.4 m/min. After setting up, deposits on the plate at a frequency *f* = 5, 10, 25, 37, 50, 75 and 100 Hz were performed. In order to avoid thermal effect from the preliminary deposition, each subsequent deposition was performed after cooling of the plate to 20 °C. The indicated parameters provided the following welding mode I_{mean} = 202–205 A, U_{mean} = 21.5 V. This, in accordance with the formula, allowed obtaining the heat input at the level *Q* = 6.0–6.2 kJ/cm.

To detect the influence of PAW frequency *f* on the width and microstructure of HAZ of welded joints, the experimental part of the work envisaged carrying out deposits on the plate of 09G2S steel with pulses of 3, 5, 10, 25, 37 and 50 Hz frequency. In order to compare the obtained results, surfacing using the conventional process of mechanized arc welding in a mixture of Ar + CO_2 was additionally performed. To conduct the experiments, the volt-ampere characteristics were selected, depicted in Figure 2, *b*, providing pulsed-arc and conventional (Figure 3) process of welding.

The modes of mechanized welding (I_{mean}, U_{mean}) by the wire Sv08G2S of 1.2 mm diameter in a mixture of Ar + CO_2 for both processes were determined using the computerized information and measuring system IMS 2007 (Table 2). The heat input *Q* for each experiment was determined by the formula.

After the completion of deposits on the plate of 12 mm thickness, the sections for metallographic

Table 1. Received modes of a pulsed-arc process at different positions of VACh No.1

VACh No.1	I_{mean}, A	U_{mean}, V	*Q*, kJ/cm	v_w, cm/min	v_{wire}, m/min
1*a*	187	22	5.760	30.0	6.8
1*b*	200	23	6.440		
1*c*	225	25.4	8.036		
1*d*	230	29.2	9.402		

Table 2. Mechanized welding modes

f, Hz	I_{mean}, A	U_{mean}, V	*Q*, kJ/cm	v_{wire}, m/min	v_w, cm/min	Note
3	203	21.8	6.195	6.4	30.0	PAW
5	203	21.6	6.139			
10	198	22.2	6.153			
25	207	21.1	6.115			
37	198	22.3	6.181			
50	205	21.0	6.027			
–	200	22.1	6.188	6.4	30.0	Stationary

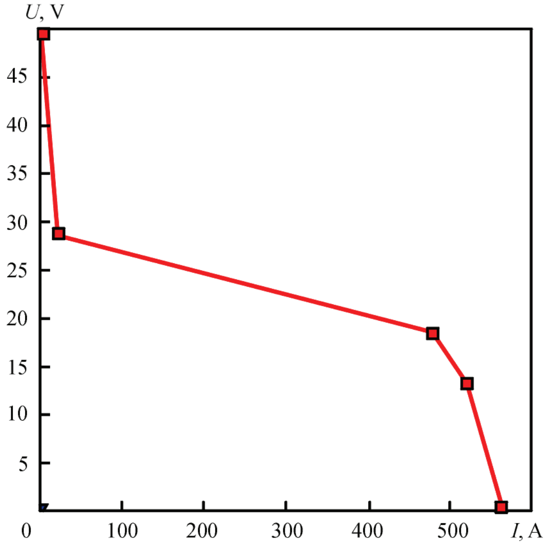

Figure 3. Volt-ampere characteristic of power source to perform mechanized welding by stationary process

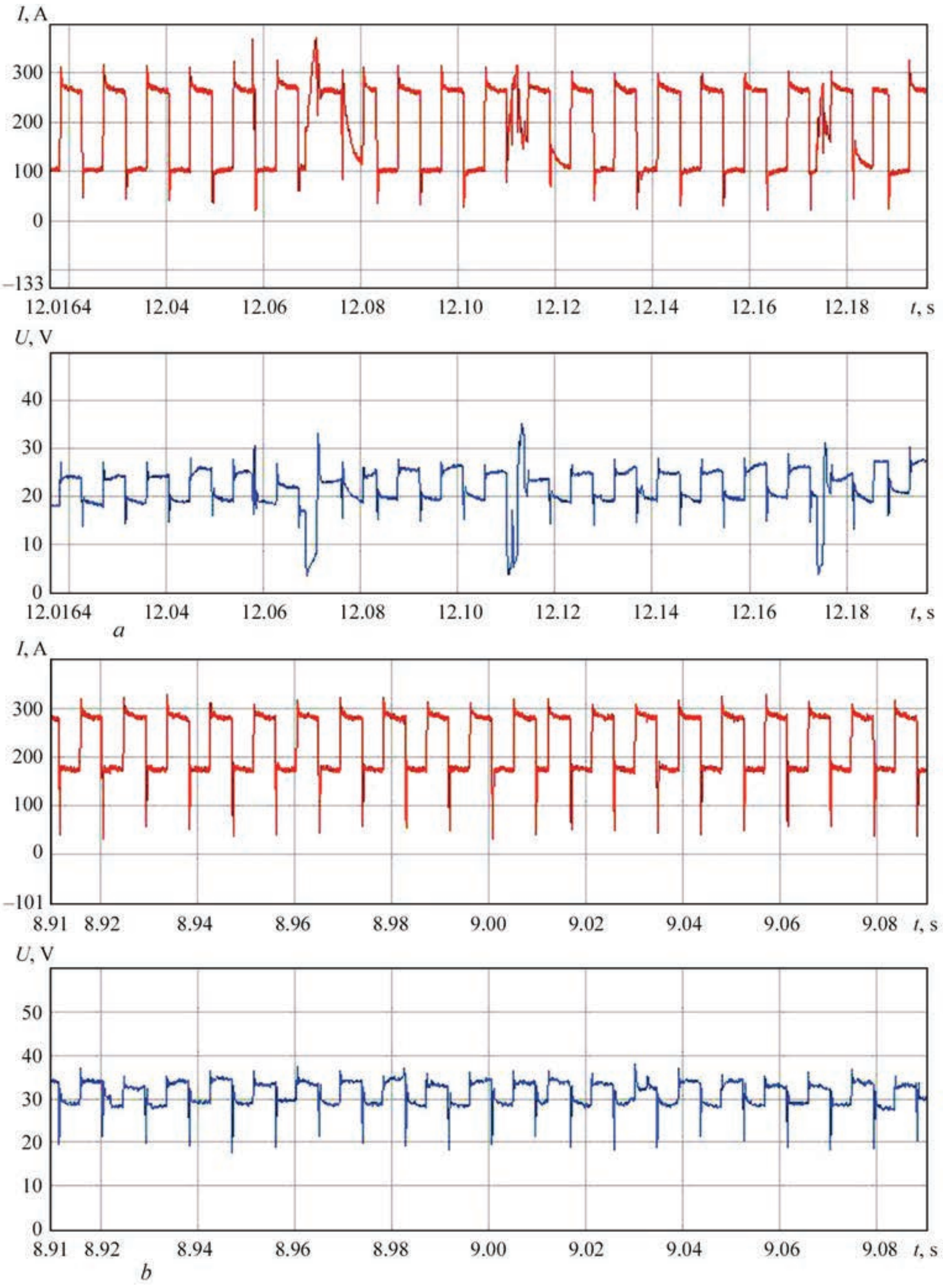

Figure 4. Oscillograms of pulsed-arc processes: *a* — with short circuits (for I_{mean} = 187 A); *b* — without short circuits (for I_{mean} = 225 A)

examinations of weld and HAZ metal were made. The hardness of the HAZ and the weld region was measured on the microhardness meter M-400 LECO.

As a result of data processing from oscillograms, it was found that a gradual increase in the value of the pause current causes an increase in the mean welding current, which increases the power of the process. Given that the rate of welding wire feed remains unchanged, a more intensive melting of the metal on the electrode end and the elongation of an arc gap occur. An increase in the mean welding voltage can be observed. A change in the pulsed-arc process with short circuits on a process without short-circuit is also observed (Figure 4).

At the histograms of the arc voltage, this is reflected by the presence of instant values in the range of $U_{sh.-c}$ = 3–10 V (Figure 5, *a*), which is characteristic for short circuits, and by their absence as compared to PAW on a “long” arc (Figure 5, *b*).

RESULTS OF INVESTIGATIONS AND DISCUSSION

Adjustment of VACh No.1 from the position 1*a* to the position 1*d* leads to an increase in the value of the heat input $Q = f(I_{mean}, U_{mean})$ with the respective changes in geometric sizes and shapes of deposited beads at v_{wire} = const, v_w = const. It was established that an increase in the pause current leads to an increase in U_{mean}, and this is ultimately reflected on the growth

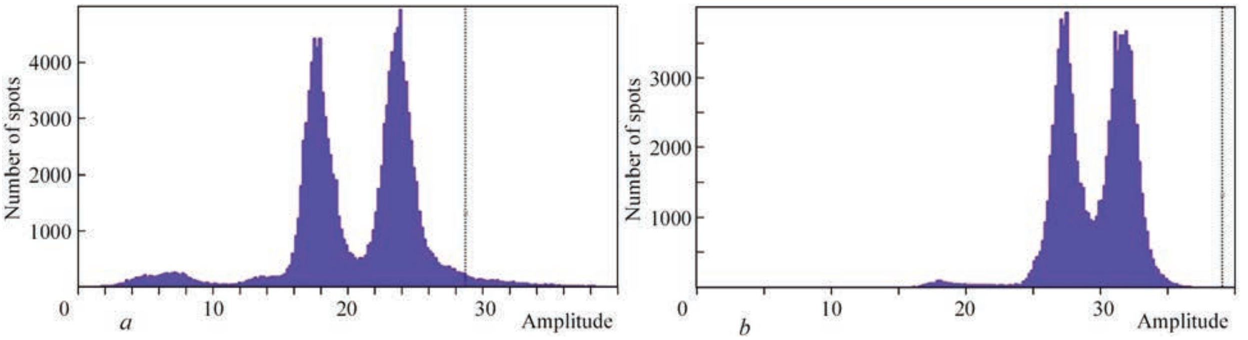

Figure 5. Histogram of instant values of arc voltage at a pulsed-arc process: *a* — with short circuits for $I_{\mathrm{mean}} = 187$ A); *b* — without short circuits (for $I_{\mathrm{mean}} = 225$ A)

in the width of the beads *b* with a corresponding decrease in the penetration depth *h* (Figure 6).

The influence of the heat input $Q = f(I_{\mathrm{mean}}, U_{\mathrm{mean}})$ of the pulsed process on the mean value of the penetration depth *h* and the width *b* of the beads is shown in Figure 7.

An analysis of the results of measurements of the width of the deposits and the penetration depth showed that an increase in the value of frequency *f* from 5 to 100 Hz does not lead to a change in geometric dimensions. The most significant influence of the frequency *f* affects the amount of ripples of the beads: with an increase in *f* to 100 Hz, the amount of ripples decreases (Figure 8). This is associated with the fact that a rapid switching of the operation of the pulsed power source from VACh No.2, which is responsible for the maximum energy level of the process, to VACh No.1, which determines the minimum energy level, does not lead to a significant cooling of molten metal. The thermal mode of the pool is approaching a quasi-stationary state, which is characteristic of conventional welding with short circuits without a pulsed effect.

Investigation of the effect of the PAW frequency *f* on the width and microstructure of HAZ of welded joints showed that the structure of the deposited weld metal is ferritic-perlitic with separate regions of a preeutectoid ferrite on the boundaries of crystallites. Regarding HAZ, the analysis as in the cases of PAW, as well as in a stationary arc showed that almost the same types of structural components are formed on a region of a coarse grain. Therefore, in general, the structure of this region in all specimens is ferritic-perlitic with different modifications of ferrite: ordered by a second phase, Widmanstätten, polyhedral (Figure 9). In the specimens that were produced during PAW with the frequencies *f* = 37, 50 Hz and by stationary welding mode, the structures of bainite were additionally revealed.

The size of grains in the region of HAZ overheating grows with an increase in frequency *f*. Therefore, for *f* = 3, 5 Hz, grain size number amounts to 7–8 ($D_{\mathrm{gr}} = 22$–30 μm); at *f* = 10 Hz — 7 ($D_{\mathrm{gr}} = 30$ μm); *f* = 25, 37 Hz — 6, 7 ($D_{\mathrm{gr}} = 30$–44 μm). For *f* = 50 Hz and the stationary process of welding, the grain size number amounts to 6 ($D_{\mathrm{gr}} = 44$ μm).

Measurement of microhardness *HV*1 in different zones showed that a gradual increase in frequency *f* does not lead to significant changes in the mean values of microhardness on the region of a coarse grain (Figure 10).

A mean value of microhardness for *f* = 50 Hz is approaching to such that is obtained in welding by a stationary arc. In the analysis of these results, it seems that with an increase in the PAW frequency *f*,

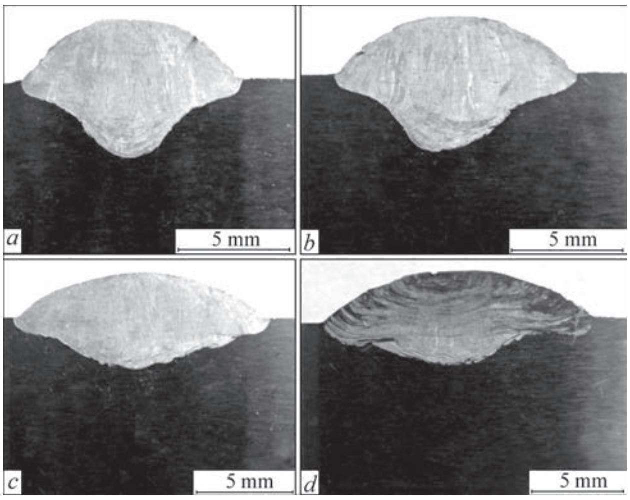

Figure 6. Macrosections of deposits performed at different VACh No.1: *a* — positions 1*a*; *b* — 1*b*; *c* — 1*c*; *d* — 1*d*

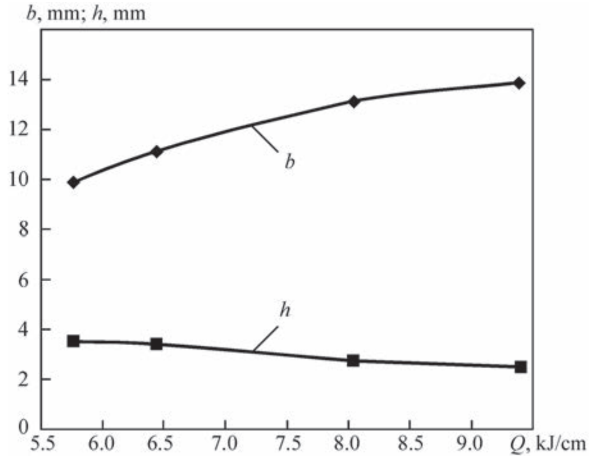

Figure 7. Dependence of penetration depth *h* and width *b* on heat input $Q = f(I_{\mathrm{m}}, U_{\mathrm{m}})$ of a pulsed process

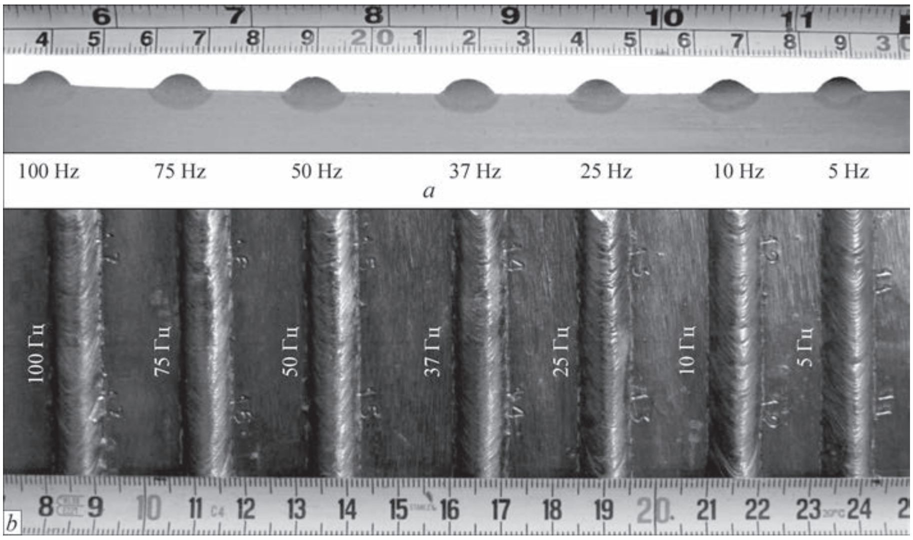

Figure 8. Influence of frequency *f* of a pulsed process on the section of beads (*a*); ripples of deposited metal (*b*)

the effect of impact on the HAZ metal approaches the process of welding with a stationary arc.

In relation to one more index — the width of HAZ, the results of metallographic examinations showed a gradual, slight decrease in the total width of HAZ with an increase in frequency *f* to 50 Hz (Figure 11).

A similar trend is observed also in the region of coarse grains in HAZ. However, as compared to the stationary process of welding, the width of this region decreases more significantly — by 25–30 %. Thus, in the case of welding low-alloy steels, due to the application of technology with a pulsed process, there is a prospect to affect the width of the region of HAZ overheating at different values of frequencies and relatively low values of the heat input *Q* (6.0–6.2 kJ/cm). From a practical point of view, this allows reducing the share of an unfavourable, low-ductile area of overheating, which is important

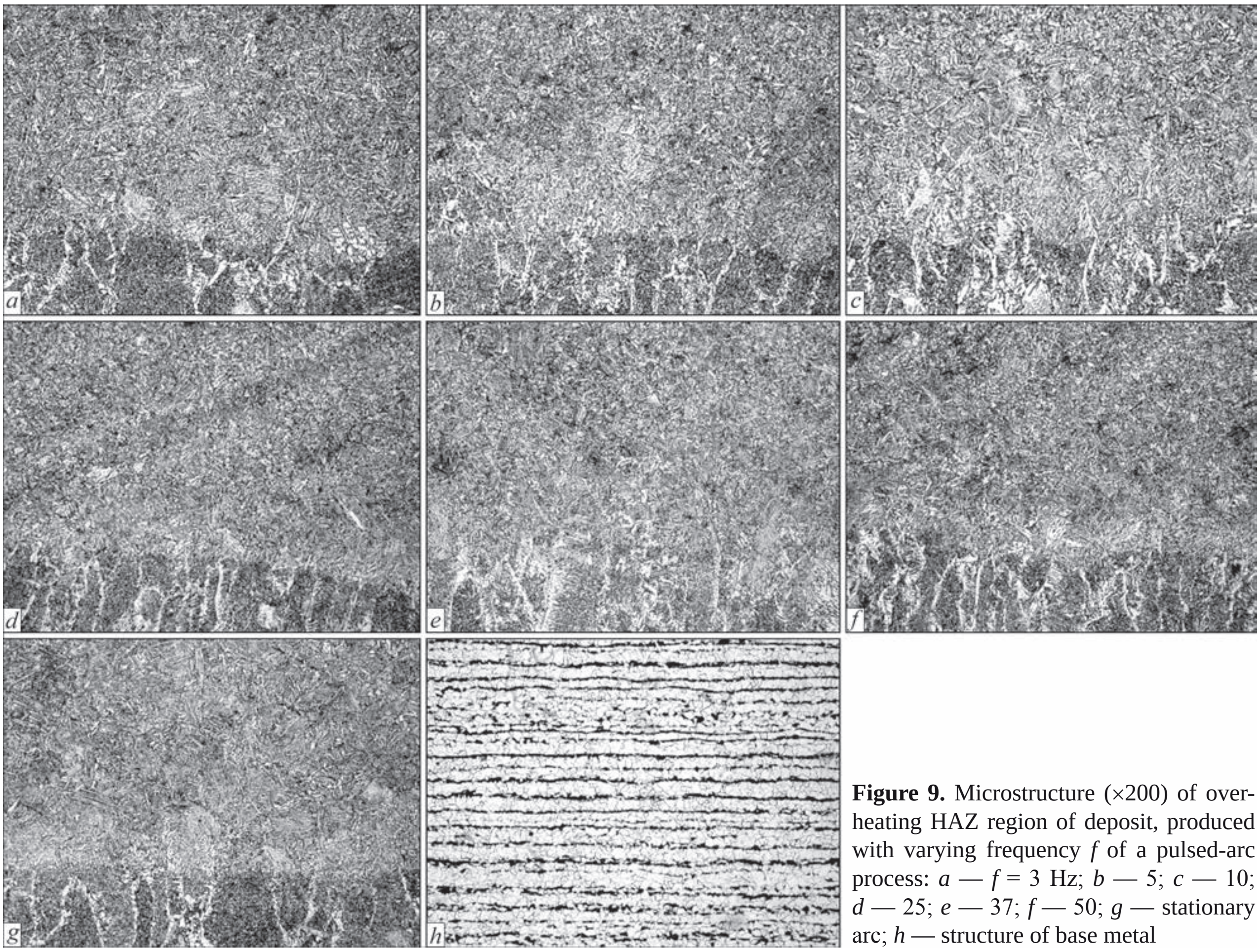

Figure 9. Microstructure (×200) of overheating HAZ region of deposit, produced with varying frequency *f* of a pulsed-arc process: *a* — *f* = 3 Hz; *b* — 5; *c* — 10; *d* — 25; *e* — 37; *f* — 50; *g* — stationary arc; *h* — structure of base metal

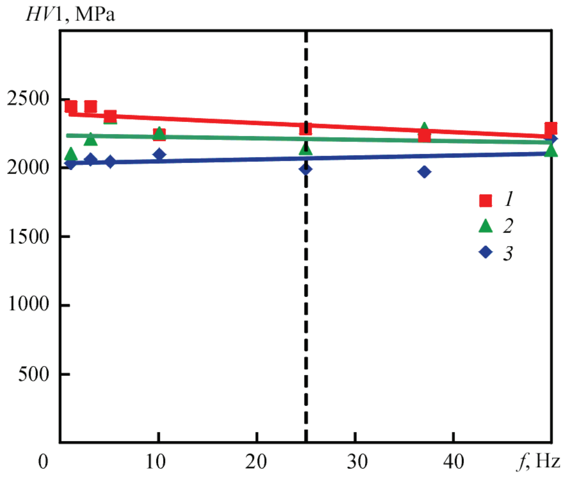

Figure 10. Impact of PAW *f* frequency on the distribution of microhardness *HV*1 in different regions of HAZ: *1* — coarse grain region near the fusion line; *2* — region of coarse grain near the region of recrystallization; *3* — weld near the fusion line

for the cases of repair of wall thinnings in the pipes during remelting of the defects in the operating pipeline using mechanized method.

CONCLUSIONS

1. It was established that a gradual increase in the pause current due to the displacement of a falling VACh region at an unchanged rate of electrode wire feed leads to an increase in the arc voltage and, as a consequence, the pulsed-arc process with short circuits changes to the process without short circuits. In this case, an increase in the width of beads by 30–40 % with a corresponding decrease in the penetration depth by 25–30 % is observed.

2. An increase in frequency from 5 to 100 Hz does not affect the geometric parameters of the weld. However, a decrease in ripples is observed.

3. It was shown that a change in the PAW frequency almost does not affect the structural components on the region of coarse grain of HAZ, which also coincide with a specimen, welded applying stationary welding modes. Also no significant changes in the values of the average microhardness on the region of a coarse grain is observed.

4. It was established that an increase in frequency has a direct proportional effect on the size of the grains in the region of HAZ overheating. Thus, as the PAW frequency increases from 3 to 50 Hz, the size of grains in the HAZ overheating region increases from 8 (D_{gr} = 22 μm) to 6 (D_{gr} = 44 μm).

5. It was established that an increase in PAW frequency allows reducing the width of HAZ and the region of a coarse grain. In this case, a decrease in the width of the region of a coarse grain is more significant and reaches 25–30 % at a frequency *f* = 50 Hz.

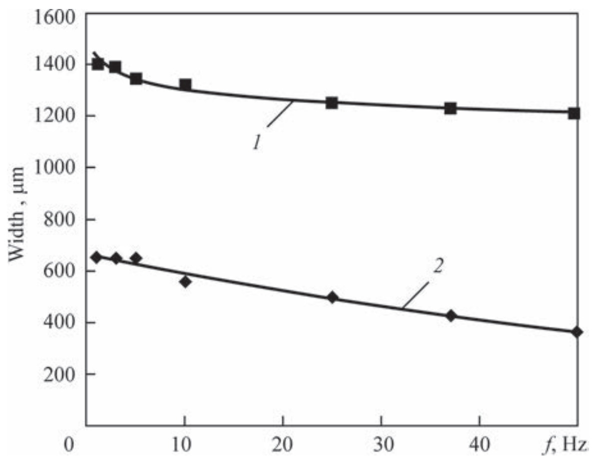

Figure 11. Impact of PAW f frequency on the total HAZ width (*1*) and width of the coarse grain region (*2*) at *Q* = 6.0–6.2 kJ/cm

REFERENCES

1. Saraev, Yu.N., Makarova, L.I., Kirilova, N.V. et al. (2001) Ways of increase in efficiency of construction, operation and repair of oil and gas equipment and main pipelines on the base of adaptive pulsed technologies of welding and surfacing. *Svarochn. Proizvodstvo*, **5**, 31–37 [in Russian].
2. Mazel, A.G., Tarlinsky, V.D., Shejkin, M.Z. (1979) *Modern methods of fusion welding of main pipelines*. Moscow, Nedra [in Russian].
3. Saraev, Ju.N. (1999) Increase in efficiency of arc welding based on an adaptive algorithm for pulsed control of process energy parameters. In: *Proc. of Int. Conf. LUI Join'99 on Efficient Welding in Industrial Applications (ICEWIA)*, 222–226.
4. Krampit, N.Yu., Krampit, A.G. (2014) Investigation of the process of CO_2 consumable electrode pulsed arc welding. *Vestnik MGTU, Ser. Mashinostroenie*, **5**, 106–112 [in Russian].
5. Knyazkov, A.F., Knyazkov, S.A. (2011) Active control of melting and transfer of electrode metal. *Svarka i Diagnostika*, **4**, 27–32 [in Russian].
6. Verevkin, A.V. (2010) *Increase in efficiency of CO_2 welding of main pipeline fixed joints through the application of pulse power supply of the welding arc*: Syn. of Thesis for Cand. of Tech. Sci. Degree., Barnaul [in Russian].
7. Krampit, M.A., Burakova, E.M., Zubenko, L.N. (2014) Tendencies of development of pulsed methods for welding process control. In: *Proc. of 5th Int. Sci.-Pract. Conf. on Innovative Technologies and Economics in Mechanical Engineering, (22–23 May 2014)*, Vol. 1.
8. Yakushin, B.F., Bakulo, A.V. (2017) On mechanism of weld metal structure formation in pulsed arc welding. *Svarochn. Proizvodstvo*, **9**, 29–35 [in Russian].
9. Manikya Kanti, K., Srinivasa Rao, P., Ranga Janardhana, G. (2013) Optimization of weld bead penetration in pulsed gas metal arc welding using genetic algorithm. *Int. J. of Emerging Technology and Advanced Engineering*, 3(**3**), 368–371.
10. Zhernosekov, A.M., Andreev, V.V. (2007) Consumable electrode pulsed arc welding. *The Paton Welding J.*, **10**, 48–52.
11. Golikov, N.I., Maksimova, E.M., Saraev, Yu.N. (2019) Investigation of the microstructure of the heat-affected zone of low-alloyed steel during pulsed arc welding under conditions of low climatic ambient temperatures. In: *OP Conf. Series: Materials Sci. and Engineering*, 681.
12. Zavdoveev A.V., Poznyakov V.D., Rogante M., et al. (2020) Features of structure formation and properties of joints of S460M steel made by pulsed-arc welding. *The Paton Welding J.*, **6**, 9–13. DOI: https://doi.org/10.37434/tpwj2020.06.02.
13. Zavdoveev, A.V., Poznyakov, V.D., Zhdanov, S.L. et al. (2020) Influence of pulsed-arc welding conditions on change of parameters of weld and HAZ of welded joints and mechan-

ical properties of low-alloy steels. *The Paton Welding J.*, **10**, 21–26. DOI: https://doi.org/10.37434/tpwj2020.12.03.
14. Krampit, A.G., Krampit, N.Yu. (2015) Methods of weld formation control. *Tekhnologii i Materialy*, **2**, 21–26 [in Russian].
15. Golikov, N.I., Sidorov, M.M., Maksimova, E.M., Saraev, Yu.N. (2018) Examination of microstructure of welded joints made under negative temperature conditions. Science — Education — Production: Experience and Prospects of Development. In: *Proc. of 14th Int. Sci.-Tech. Conf. (8–9 February 2018)*, 161–164.
16. Saraev, Y.N., Bezborodov, V.P. (2013) Effect of the energy parameters of the welding process on the structure and properties of welded joints in low-alloy steels. *Welding Intern.*, 2(**9**), 678–680.

ORCID

S.Yu. Maksymov: 0000-0002-5788-0753,
D.M. Krazhanovskyi: 0000-0001-7292-7188,
Yu.A. Shepelyuk: 0000-0002-2912-2648

CONFLICT OF INTEREST

The Authors declare no conflict of interest

CORRESPONDING AUTHOR

S.Yu. Maksymov
E.O. Paton Electric Welding Institute of the NASU
11 Kazymyr Malevych Str., 03150, Kyiv, Ukraine
E-mail: maksimov@paton.kiev.ua

SUGGESTED CITATION

S.Yu. Maksymov, D.M. Krazhanovskyi,
Yu.A. Shepelyuk, S.V Osynska (2022) Effect of parameters of pulsed-arc welding on the formation of weld metal and microstructure of heat-affected zone of 09G2S steel. *The Paton Welding J.*, **3**, 19–26.

JOURNAL HOME PAGE

https://pwj.com.ua/en

Received: 26.01.2022
Accepted: 16.05.2022

https://doi.org/10.37434/tpwj2022.03.03

FOR DISCUSSION

INFLUENCE OF WELDING MODES ON DECARBURIZATION IN THE HEAT-AFFECTED ZONE OF R91 STEEL IN WELDED JOINTS OF DISSIMILAR STEELS AFTER HIGH-TEMPERATURE TEMPERING

M.O. Nimko, V.Yu. Skulskyi, A.R. Gavryk, I.G. Osypenko

E.O. Paton Electric Welding Institute of the NASU
11 Kazymyr Malevych Str., 03150, Kyiv, Ukraine

ABSTRACT

Carbon migration from the lower-alloyed to the higher-alloyed steel takes place in welded joints of dissimilar steels, as a result of difference in carbon chemical potential after tempering and in high-temperature service. Decarburization in the HAZ near-weld zone of the lower-alloyed steel can lead to formation of service defects and subsequent failure. From mass transfer theory it is known that in polycrystalline bodies the diffusion of interstitial elements, including carbon, occurs most rapidly along the grain boundaries. Theoretically, reduction of carbon diffusion can be achieved by increasing the grain dimensions in the HAZ near-weld zone that will lead to reduction of the overall grain boundary area per a unit of volume in this zone. This work is a study of the influence of the angle of electrode inclination and welding current at deposition of austenitic metal on R91 steel on the width of the decarburized interlayer, forming at subsequent tempering at the temperatures of 700 and 760 °C. It is shown that the resultant decarburized interlayer becomes narrower with increase of the angle of electrode inclination and deposition current.

KEYWORDS: carbon diffusion, dissimilar steel joint, HAZ, decarburized interlayer, grain boundaries

INTRODUCTION

Problems related to carbon migration from the lower-alloyed steel to the higher-alloyed one started arising from the beginning of application of combined joints with austenitic stainless steels and respective welding consumables in pipe systems of boilers in 1940s. First accidents were recorded in 1950s and efforts were made to improve the equipment operation mode and to understand the causes for this phenomenon. In 1960s there was an increase in application of transition joints from austenitic materials for the needs of boiler construction, particularly when the steam temperature rose up to 566 °C. In 1970s and 1980s the scope of application and number of failures of the transition welds increased. Numerous studies of the causes for these accidents showed that carbon migration in welded joints of dissimilar steels at higher temperatures is an important factor [1].

As ferritic steels have higher carbon content than austenitic ones, the gradient of carbon concentration in the zone of contact of these steels decreases from ferritic towards austenitic steel. At higher temperatures carbon diffuses in the direction of reduction of the chemical potential gradient. It is important to note that chromium lowers the carbon chemical potential [2], while carbon content increases from ferritic-martensitic to austenitic steel. Therefore, the gradients of chromium and carbon concentration create a rather abrupt gradient of chemical potential across the fusion zone. More over, the coefficient of carbon diffusion in ferrite is much higher, than that in austenite, while the solubility is lower. These factors result in a strong driving force for carbon diffusion from ferritic to austenitic steel, leading to formation of a decarburized interlayer.

The decarburized interlayer has lower mechanical properties, which can be characterized by hardness reduction and high concentration of localized strain measured during tensile testing [1]. An important aspect of degradation of the properties associated with decarburization, is the loss of long-term hardening mechanism, because of dissolution of $M_{23}C_6$, M_7C_3 carbides and MX carbonitrides [3] that decreases the dispersion hardening. The recrystallization process also eliminates the combined influence of dislocation and subgrain-boundary hardening [4]. The consequence is the possibility of fracture inside the decarburized interlayer [1, 5, 6].

In its turn, a carburized interlayer forms in the higher-alloyed steel. In work [7], it was shown that microcracks can initiate in such a carburized interlayer. Microcracks predominantly initiate in the transition zone and are intragranular.

This necessitates reducing the decarburized interlayer in dissimilar steel joints in high-temperature service under creep conditions. It is general practice to

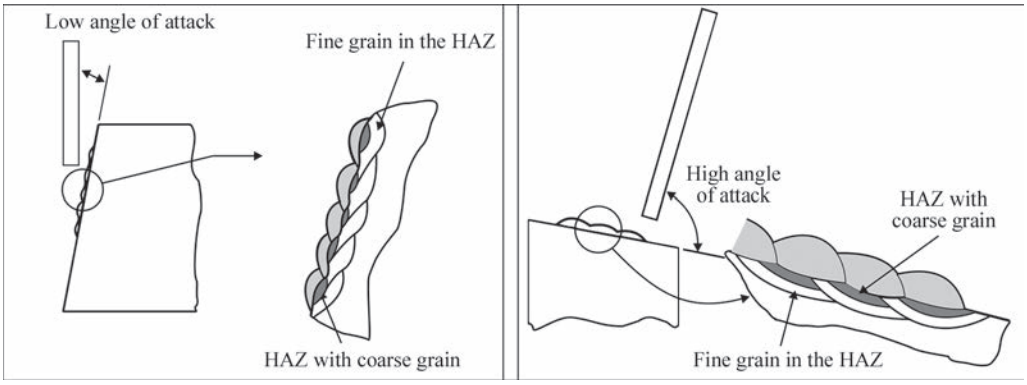

Figure 1. Technique of cladding the plate edges by austenitic metal [13]

use nickel welding consumables to reduce carbon diffusion. However, most of the researchers believe that the traditional nickel-based materials (for instance, Ni 6082, Ni 6182, Ni 6117, Ni 6625 to DSTU ISO 14172) cannot effectively completely contain carbon diffusion from martensitic steel into the weld, as most of the nickel alloys used as welding consumable, contain a large quantity of carbide formers, in particular chromium [8–11].

The problem of containment diffusion-induced carbon redistribution remains urgent and requires other approaches (methods) to solve it. In the first part of the work [12] investigations were performed of the influence of the modes of surfacing (heat input and heating temperature) by an austenitic welding consumable on development of the width of decarburized interlayer in X10CrMoVNb9-1 (R91) steel at tempering at 750 °C temperature for 7 and 18 h, and it was clarified that the interlayer width after tempering decreases with heat input increase; with increase of heating temperature from 20 to 195 °C the width of the interlayer after tempering also decreases, and then starts increasing with heating up to 300 °C. Considering that the above investigations were performed using single-interlayer austenitic deposits on martensitic steel surface, it was necessary to check the obtained regularities on real combined joints.

The objective of the study was to verify the influence of the welding mode and technique (electrode inclination angle) on decarburization kinetics in the HAZ near-weld zone of the lower-alloyed steel in the combined welded joints after high-temperature tempering.

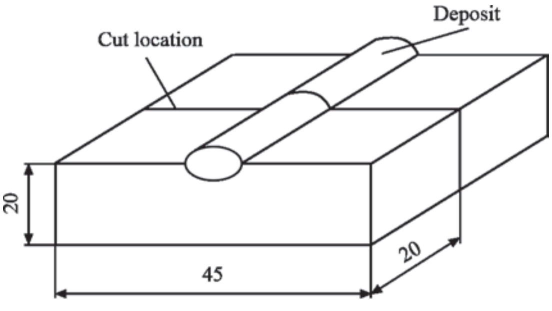

Figure 2. Scheme of cutting up the deposit into templates

INVESTIGATION PROCEDURE

Martensitic steel R91 (X10CrWMoVNb9-2 (1.4901) to DSTU EN 10216-2:2016), containing 9 % Cr (wt.%: 0.1 C; 0.34 Si; 0.47 Mn; 8.52 Cr; 0.28 Ni; 0.93 Mo; 0.2 V; 0.072 Nb; 0.06 N), was selected for the experiments. Austenitic welding consumable Fox CN 23/12 Mo–A (wt.%: 0.01 C; 0.63 Si; 0.73 Mn; 23.0 Cr; 13.1 Ni; 2.6 Mo) was chosen for surfacing, to create an alloying gradient. Such butt joints can occur in welding boiler pipe systems, for instance, boiler manifold from R91 steel with superheaters from austenitic steels.

Two different approaches to welding were used:

1) To assess the influence of welding technique, namely angle of electrode inclination on decarburization kinetics single-pass deposits were made (to eliminate the reheating effect) on R91 steel plates, using Fox CN 23/12 Mo-A electrodes. Deposits were made at small (~30°) and large (~90°) angles of inclination. It was anticipated that each mode introduces a different degree of overheating in near-weld zone and is known to cause a reduction or increase of the dimensions of coarse-grained microstructural regions (Figure 1). A larger angle of electrode inclination promotes greater heating of the near-weld zone and contrarily — lower heating is observed at a smaller angle of inclination.

In both the cases surfacing was performed in the following mode: $I_w = 120$ A, $U_a = 24$ V, $v_w \approx 4.5$ mm/s at room temperature.

After deposition samples were cut into two templates (Figure 2). To intensify the processes of carbon diffusion and formation of a decarburized interlayer, they were tempered at the temperature of 700 °C for 7 and 18 h. As-tempered templates were used to prepare sections, which were electrolytically etched in H_2CrO_4 for 15 s at the voltage of 10 V to reveal the decarburized interlayer.

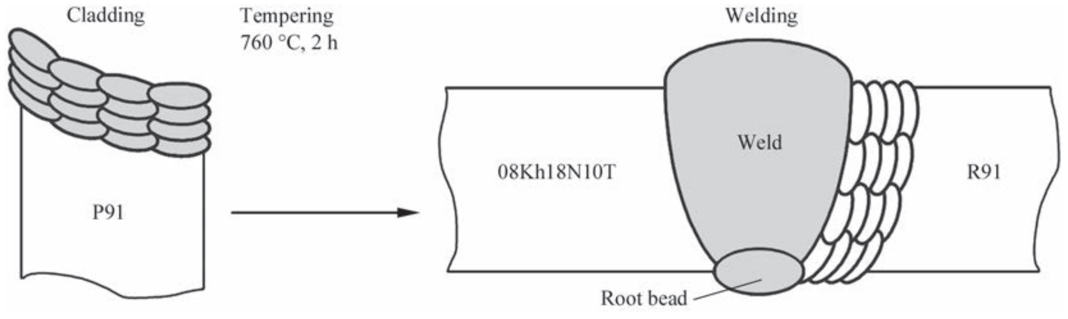

Figure 3. Scheme of cladding and welding

2) To assess the influence of the welding mode on decarburization kinetics in a real welded joint, two test joints were made on plates from martensitic steel R91 20 mm thick. Before welding the butt joints, the edges of R91 steel were first surfaced with Fox CN 23/12 Mo-A austenitic electrodes of 3.2 mm diameter in 4–5 interlayers. After surfacing the plate was tempered at 760 °C, 2 h. The surfaced and tempered edge was welded to 08Kh18N10T steel, using Fox CN 23/12 Mo-A electrodes, at current I_w = 120 A, with 60° groove angle (Figure 3). In order to ensure a high-quality formation of welded joints, root welding was performed from the reverse side of the butt after filling the groove.

The need for high-temperature tempering at the temperature of 760 °C in martensitic steel joints is attributable to the fact that dislocation excess develops in the HAZ of such steels after welding. In the presence of residual stresses, the high dislocation density accelerates the processes of recovery and recrystallization in steel that adversely affects the long-term strength [4]. High-temperature tempering leads to reduction of dislocation density and, thus, promotes an increase of long-term strength in the low loading range in high-temperature service.

Two surfacing modes were checked:

- with a small angle of inclination (~30°) at the current of I_w = 110 A;
- with a large angle of inclination (~90°) at the current of I_w = 130 A.

After welding, tempering at 700 °C for 14 h was performed for part of the samples to simulate the thermal impact in service (corresponds to ~16.8 thou h at the temperature of 600 °C at conversion using Larsen–Miller parameter [14]. After welding and tempering, sections were prepared from the samples. The microstructure of welded joint metal was revealed by electrolytic etching in chromic acid (U = 10 V, t = 10 s). Microhardness was measured in PMT-3 hardness meter at 100 g load. Metallographic analysis was performed using NEOPHOT-3 optical microscope.

In publications, for instance [15], the notion of effective width of the diffusion interlayer is used, which is determined by the shortest distance from the saturation surface (for instance, fusion line) to the measurement region. This width is characterized by established nominal values of basic parameter, which is taken to be either the diffusing element concentration, or the property (hardness) or structural feature, such as weak etchability of this region. At the same time, it is rather complicated to precisely determine the carbon content, using modern methods of elemental analysis (for instance, us-

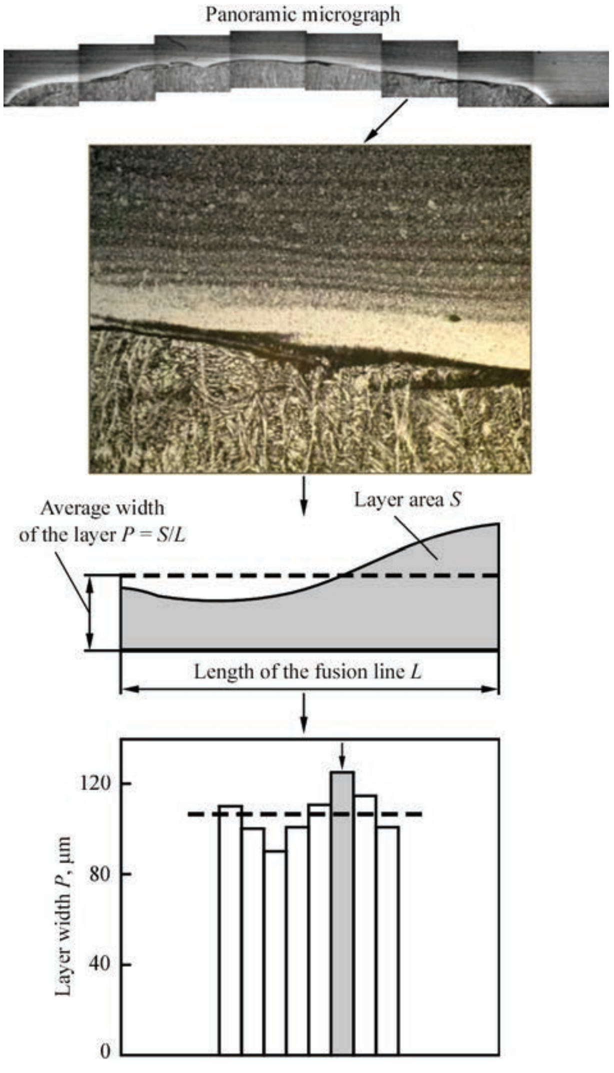

Figure 4. Scheme of plotting the histograms (adapted from [12])

ing electron probe X-Ray microanalysis), because carbon is a light element ($Z > 10$) [1].

Panoramic micrographs of the structure along the fusion line were taken at ×100 magnification, in order to determine the average width of the decarburized interlayer in the tempered deposits. From 8–9 (for deposits) to 16–17 (for welded joints) micrographs were obtained, depending on the length of the fusion line. The area of the weakly-etched near-weld zone and length of the fusion line were measured using free ImageJ software [16]. Measurement results were used to plot histograms for the case of variation of the angle of electrode inclination at surfacing and of the welding mode. Each bar of the histograms reflects the interlayer width in a certain micrograph, the bars are located in the order of filming and numbering of the micrographs from the bead left edge to its right edge (Figure 4).

Mean values of diffusion interlayer width P for each bead (dash line in the histograms) were found by the following formula

$$P = \frac{\sum_{i=1}^{n} (p_i l_i)}{\sum_{i=1}^{n} l_i},$$

where p_i is the width of the diffusion interlayer (μm) in a certain micrograph (n is the total number of micrographs for a certain bead); l_i is the length of the fusion line (μm) in a certain micrograph i.

EXPERIMENTAL RESULTS AND THEIR ANALYSIS

Figure 5 gives examples of micrographs of near-weld zone of R91 steel in the deposits after tempering at 700 °C, for 7 and 18 h, respectively, Figure 6

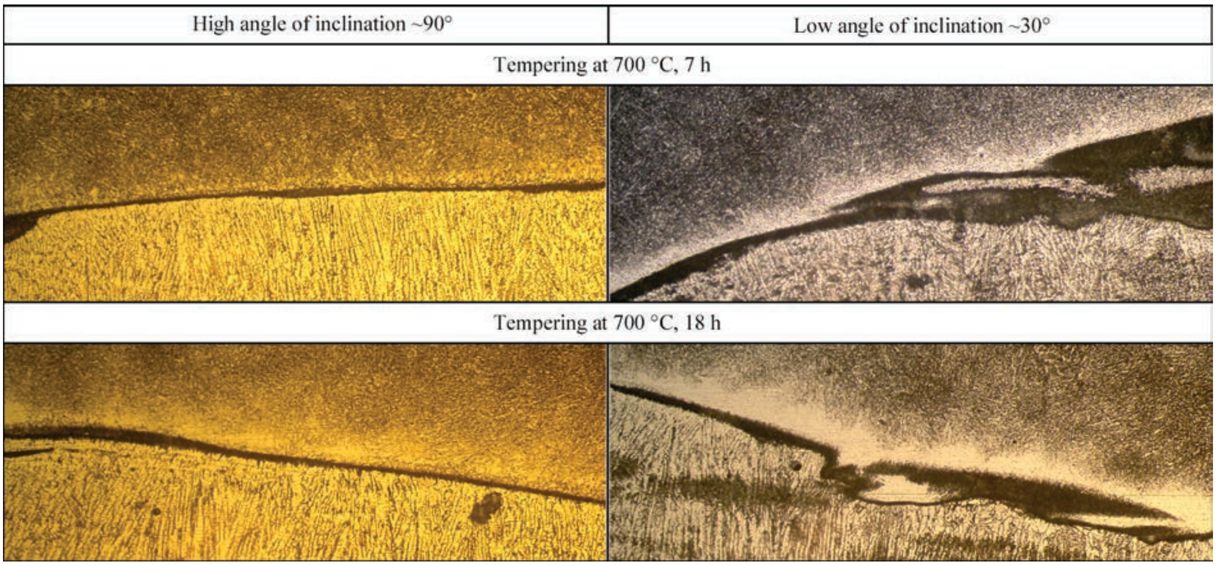

Figure 5. Example of micrographs to determine the interlayer width, depending on the angle of inclination after tempering, ×100 (lower weld)

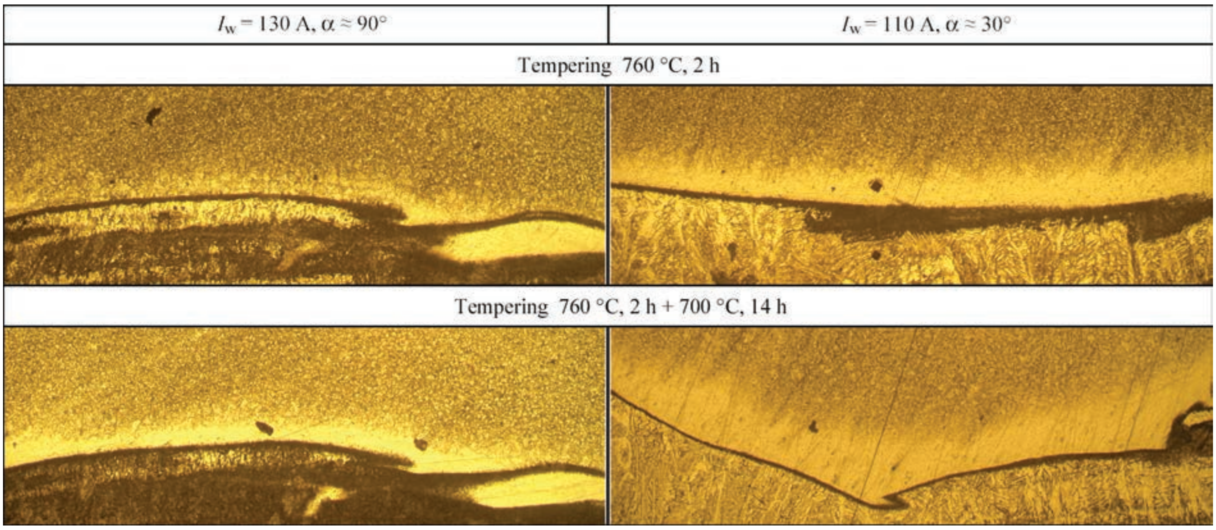

Figure 6. Example of micrographs to determine the interlayer width, depending on welding mode after tempering, ×100 (lower weld below)

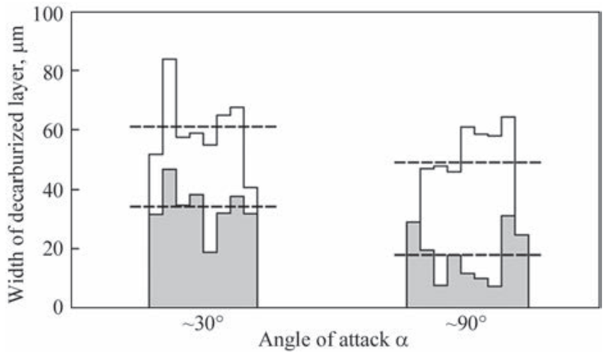

Figure 7. Histograms of the dependence of decarburized interlayer width on parameters of the angle of electrode inclination in the near-weld zone of R91 steel after tempering at 700 °C, for 7 h (contour filled with gray colour) and at 700 °C, for 18 h (contour filled with white colour)

are welded joint micrographs. A noticeable range of variation of the decarburized interlayer width at the same temperature holding can be seen in these micrographs. Figure 7 shows the built by the above procedure histograms of the decarburized interlayer width, depending on the parameter of the angle of electrode inclination after tempering at 700 °C for 7 and 18 h, and Figure 8 presents histograms of the decarburized interlayer width, depending on the surfacing mode in the welded joint after tempering at 760 °C, for 2 h and at 760 °C for 2 h + 700 °C for 14 h.

Additional measurement of microhardness in welded joints in the HAZ of R91 steel under the middle of the second clad bead from the top was performed for both the welding modes (Figure 9). The results show that in the mode with lower current and higher decarburization a noticeable softening is observed in the near-weld zone, as well as in the zone of critical temperatures between A_{C1} and A_{C3}, compared to the mode at a higher current and with lower decarburization. It enables establishing a direct relationship between the structural and mechanical characteristics of the metal, as a result of carbon diffusion in the near-weld zone: softening becomes greater with increase of decarburization visible in the micrographs.

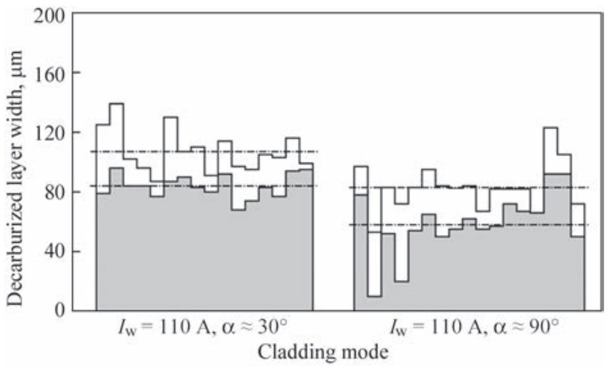

Figure 8. Histrograms of the dependence of decarburized interlayer width on the parameters of welding mode in the near-weld zone of R91 steel after tempering at 760 °C for 2 h (gray coloured contour)

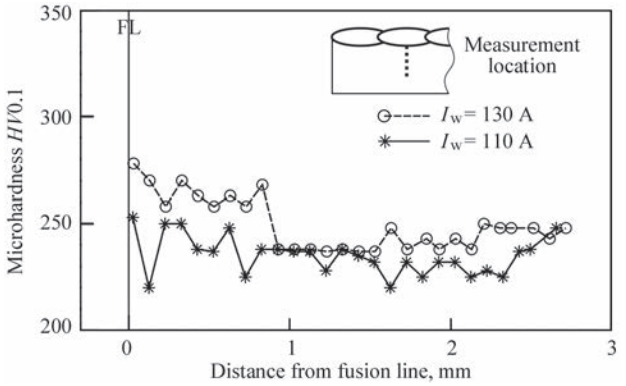

Figure 9. Microhardness in the HAZ near-weld zone of R91 steel after tempering at 760 °C, for 2 h + 700 °C, 14 h

The data obtained from the histograms agree with investigation results, described in the previous paper [12]: the rate of development of the decarburized interlayer at tempering decreases at increase of the heat input. This is related to the fact that at the temperatures of high tempering and lower, diffusion along the grain boundaries is the prevailing type of diffusion. At surfacing at high mode parameters, the area of grain boundaries per a unit of volume becomes smaller than that in the metal with a deposit made at lower parameters, as a result of growth of primary austenite grain in the near-weld zone that limits the grain-boundary diffusion.

Grain-boundary diffusion is a complex process which includes direct diffusion through the grain lattice, diffusion along the grain boundaries, scattering of the diffusing substance from the grain boundaries and its subsequent infiltration into the grain lattice around the intergranular boundaries [17]. Different diffusion kinetics (or diffusion modes) can be observed, depending on prevalence of one of these elementary processes. Each mode prevails in a certain temperature range and soaking duration at these temperatures, and it also depends on grain dimensions, lattice parameters and grain boundaries.

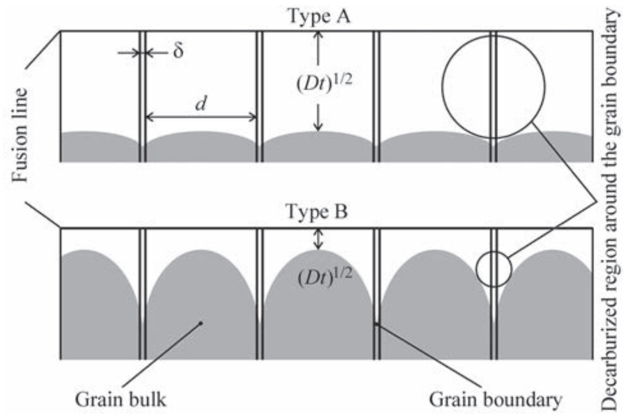

Figure 10. Diffusion kinetics of type A and B (using the data of [17])

Figure 10 shows two of the three types of diffusion kinetics classification.

KINETICS OF TYPE A

This kinetics is observed at high-temperature or long-term soaking at higher temperature in materials with small-sized grains. In work [18] it is shown that realization of such kinetics requires that the diffusion length $\sqrt{Dt}$ (where D is the coefficient of diffusion in the lattice (m^2/s); t is the time from the start of diffusion (c)) was only a little larger than the distance between the grain boundaries d:

$$\sqrt{Dt} \geq \frac{d}{0,8}.$$

In such a case, the decarburized regions around the adjacent grain boundaries overlap, and the decarburization front can capture the grain bulk.

KINETICS OF TYPE B

This kinetics is characteristic for materials after soaking at lower temperatures and/or at relatively short soaking duration in materials with sufficiently large grain size. Under such conditions, diffusion length $\sqrt{Dt}$ ahead of the grain body can become much smaller, than the distance between the grain boundaries d. At the same time, the width of near-boundary decarburized regions that is also calculated using $\sqrt{Dt}$ can be much greater than the width of grain boundaries, δ. Therefore, the following condition is satisfied for kinetics of type B:

$$\delta \ll \sqrt{Dt} \ll d.$$

At this kinetics, decarburization takes place from regions around the grain boundaries into carbon-depleted boundary regions of the grains, where diffusion has already occurred. However, unlike type A, the decarburized regions around adjacent grain boundaries do not overlap in the grain bulk [17].

At increase of grain size, type A kinetics gradually develops into type B kinetics, so that any deviations in grain size distribution in the HAZ near-weld zone after welding, caused by different heat input, will result in different decarburization rate. These data show that from the view point of the process of containment the decarburization, the coarse-grained structure has advantages over the fine-grained one. The coarse-grained structure also has a positive effect on long-term strength. This is attributable to the fact that deformation and destruction at high temperatures often take place along the grain boundaries, which have a large number of defects (vacancies, dislocations, etc.): at higher temperatures and presence of stresses elementary events of slipping and nucleation of cavities and microcracks easily occur along them, which lead to decohesion of grain boundaries [4, p. 346]. Thus, while at low temperatures the high density of grain boundaries (at fine-grained structure) promotes deceleration of dislocation motion and alloy hardening, at high temperatures, contrarily, the high density of the boundaries facilitates accelerated softening of polycrystalline metals. Therefore, coarser grain promotes an increase of high-temperature strength [15, p. 302].

The disadvantages of the coarse-grained structure in the HAZ near-weld zone are lower ductility and impact toughness, and in low-alloyed steels also the susceptibility to formation of tempering cracks. However, in the case of R91 steel, it was reported that it is not prone to temper cracking [4]. As regards impact toughness, the most critical portion of martensitic and ferritic steel joints is the region of the first cladding interlayer: intensive dilution and mixing take place in the first deposited beads with different ratios of the melt of base metal with electrode metal. In particular, nickel content in the mixed zone decreases in the direction away from the melting zone to the less alloyed base metal. In a certain point in the region of this lowering the nickel content becomes too low to stabilize austenite at cooling to room temperature, but the relatively high alloying level in this zone promotes a high hardness resulting in martensite formation there [2]. In particular, performed impact toughness testing in the first interlayer of both the deposits — at 110 and 130 A — showed that *KCV* value in this region varies within 30 J/cm^2. This zone, however, did not make any negative effect on other properties in the condition after welding and tempering — bend angle of transverse samples was not less that 100°, and fracture at static tensile testing of transverse samples occurred in the austenitic base metal.

CONCLUSIONS

1. It is established that the width of the decarburized interlayer in R91 steel, clad and welded by austenitic welding consumable, which develops at tempering or in high-temperature service, can vary at the change of values of the angle of electrode inclination: interlayer width decreases at the angle close to 90°, and increases at reduction of the angle of inclination to 30°. The width of the interlayer on samples made with angle of inclination of 30°, is greater than that on samples made with angle of inclination of 90°, after soaking at 700 °C for 7 h — 1.89 times, and after soaking for 18 h — 1.24 times.

2. Metallographic investigations and hardness measurements show that reduced decarburization and softening in the HAZ near-weld zone of marten-

sitic steel is observed after high-temperature tempering in the real welded joint of martensitic and austenitic steels, clad in the higher current mode (up to 130 A) than in the joint clad in the lower current mode (110 A). The width of the interlayer in the joints made at 110 A current with angle of inclination of 30°, is greater than that of the interlayer made at 130 A current with angle of inclination of 90°, after soaking at 760 °C for 2 h — 1.45 times; and after additional soaking at 700 °C for 14 h — 1.29 times.

REFERENCES

1. Lundin, C.D., Khan, K.K., Yang, D. (1995) Effect of carbon migration in Cr–Mo weldments on metallurgical structure and mechanical properties. *Welding Research Council Bull.*, **407**, 1–49.
2. DuPont, J.N. (2012) Microstructural evolution and high temperature failure of ferritic to austenitic dissimilar welds. *Int. Materials Reviews*, 57(**4**), 208–234.
3. Dawson, K.E., Tatlock, G.J., Chi, K., Barnard, P. (2013) Changes in precipitate distributions and the microstructural evolution of P24/P91 dissimilar metal welds during PWHT. *Metallurg. and Mater. Transact. A*, **44**, 5065–5080.
4. Abe, F., Kern, T.-U., Viswanathan, R. (2008) *Creep-resistant steels*. Cambridge, Woodhead Publishing.
5. Helander, T., Andersson, H.C.M., Oskarsson, M. (2000) Structural changes in 12–2.25 % Cr weldments — an experimental and theoretical approach. *Mater. High Temp.*, 17(**3**), 389–396.
6. Brett, S.J. (2004) Type IIIa cracking in 1/2CrMoV steam pipework systems. *Sci. and Technol. of Welding and Joining*, 9(**1**), 41–45.
7. Frei, J., Alexandrov, B.T., Rethmeier, M. (2019) Low heat input gas metal arc welding for dissimilar metal weld overlays Pt III: Hydrogen-assisted cracking susceptibility. *Welding in the World*, **63**, 591–598.
8. You, Y., Shiue, R.K., Shiue, R.H., Chen, C. (2001) The study of carbon migration in dissimilar welding of the modified 9Cr–1Mo steel. *J. of Materials Sci. Letters*, **20**, 1429–1432.
9. Karthick, K., Malarvizhi, S., Balasubramanian, V., Gourav Rao, A. (2018) Tensile properties variation across the dissimilar metal weld joint between modified 9Cr–1Mo ferritic steel and 316LN stainless steel at RT and 550 °C. *Metallography, Microstructure and Analysis*, **7**, 209–221.
10. Urzynicok, M., Jachym, R., Kwiecinski, K. et al. (2013) Application of EPRI87 in dissimilar welding austenitic martensitic welded joints of TEMPALOY AA-1 and T92 steel grades. In: *Proc. of 7th Inter. Conf. on Advances in Materials Technology for Fossil Fuel Power Plants* (*Waikoloa, Hawaii, USA*), 992–1005.
11. Coleman, K., Gandy, D. (2007) Alternative filler materials for DMWs involving P91 materials. Advances in materials technology for fossil power plants. In: *Proc. of 5th Inter. Conf. on Advances in Materials Technology for Fossil Fuel Power Plants* (*Marco Island, Florida, USA*), 940–967.
12. Nimko, M.O. (2021) Influence of welding parameters on decarburization in heat affected zone of dissimilar weldments after post weld heat treatment. *Archives of Materials Sci. and Engineering*, 112(**1**), 23–31.
13. Defects/imperfections in welds – reheat cracking. *Job Knowledge for Welders*, 48, TWI, July 2000, 4 p. www.twiglobal.com/technical-knowledge/job-knowledge/defectsimperfections-in-welds-reheat-cracking-048
14. Tamura, M., Abe, F., Shiba, K. et al. (2013) Larson–Miller constant of heat-resistant steel. *Metallurg. and Mater. Transact. A*, 44(**6**), 2645–2661.
15. *Lakhtin* Yu.M. (1984) *Metals science and heat treatment*. Moscow, Metallurgiya [in Russian].
16. *Image Processing and Analysis in Java*. https://imagej.nih.gov/ij/
17. Mehrer, H. (2007) *Diffusion in solids. Fundamentals, methods, materials, diffusion-controlled processes*. Springer-Verlag.
18. Belova, I.V., Murch, G.E. (2001) The transition from Harrison type-B to type-A kinetics in grain-boundary tracer diffusion. *Philosophical Magazine A*, 81(**10**), 2447–2455.

ORCID

M.O. Nimko: 0000-0002-9672-4921,
V.Yu. Skulskyi: 0000-0002-4766-5355

CONFLICT OF INTEREST

The Authors declare no conflict of interest

CORRESPONDING AUTHOR

V.Yu. Skulskyi
E.O. Paton Electric Welding Institute of the NASU
11 Kazymyr Malevych Str., 03150, Kyiv, Ukraine
E-mail: vsku@paton.kiev.ua

SUGGESTED CITATION

M.O. Nimko, V.Yu. Skulskyi, A.R. Gavryk, I.G. Osypenko (2022) Influence of welding modes on decarburization in the HAZ of R91 steel in welded joints of dissimilar steels after high-temperature tempering. *The Paton Welding J.*, **3**, 27–33.

JOURNAL HOME PAGE

https://pwj.com.ua/en

Received: 17.01.2022
Accepted: 16.05.2022

https://doi.org/10.37434/tpwj2022.03.04

FEATURES OF MICROSTRUCTURE OF JOINTS OF HYPEREUTECTOID AREAL-136HE-X RAIL STEEL IN FLASH-BUTT WELDING

V.I. Shvets[1], O.V Didkovskyi[1], Ye.V. Antipin[1], I.V. Zyakhor[1], L.M. Kapitanchuk[1], Wang Qichen[2]

[1]E.O. Paton Electric Welding Institute of the NASU
11 Kazymyr Malevych Str., 03150, Kyiv, Ukraine
[2]CIMC Offshore Engineering Institute Company Limited Yantai
70 Zhifudao E Rd, Zhifu District, Yantai, Shandong, 264012, P.R. China

ABSTRACT

The microstructure and properties of butt joints of rails from hypereutectoid Areal 136HE-X steel produced by the flash-butt welding technology were investigated. It was found that under thermal and deformation conditions of welding, carbon redistribution is accompanied by the formation of particles in the microstructure with carbon precipitation and a decrease in carbon content in the matrix. A number of particles grows in the direction of the butt and their highest concentration is observed in the near-contact layer. According to the distribution of hardness in the zone of a coarse grain, in contrast to the butt joints of hypoeutectoid rails, as compared to the base metal, the hardness is slightly reduced — *HV* 3900 MPa and *HV* 4000 MPa, respectively. This is caused by the absence of free carbides in the microstructure. The features of microstructure do not significantly affect the results of tests on static bending and meet the requirements of domestic and European standards.

KEYWORDS: flash-butt welding, hypereutectoid rail steels, carbon redistribution, hardness distribution, static bending

INTRODUCTION

The complex conditions of operation of rolling stock of railway transport require the improvement of strength characteristics of both the rails and their joints. This was the reason for the start of numerous developments, the aim of which was to produce rail steels resistant to an increased axial load on the track and cyclic loads caused by an increased speed of movement. The possibilities of heat treatment of hypoeutectoid rail steels are exhausted. As one of the ways to improve the quality of rails, the use of hypereutectoid steels with a carbon content of more than 0.8 % is considered. It is envisaged to increase wear resistance due to carbide structural components on the boundaries of primary austenitic grains.

During construction of railway tracks, the most common technological process of joining rails is flash-butt welding (FBW) [1]. FBW of rails is fully automated and used worldwide as a method that provides a high quality and efficiency of the process. An increase in carbon content in rail steel required the improvement of FBW technology. It is known about the works [2, 3] on the development of methods and optimization of conditions for FBW of hypereutectoid rails, which were conducted by Nippon Steel & Sumitomo Metal Corporation (Japan). The choice of conditions was carried out with taking into account the comparison of the distribution of hardness with the nature of abrasive wear of metal within a joint.

In Ukraine, FBW of rails is performed by using stationary and mobile machines of the PWI of the NASU. To weld rails with a hypereutectoid carbon content, certified programs of pulsating flashing are used, according to which the adjustment of heat input is carried out by changing the duration of flashing and values of welding current [4, 5].

Hypereutectoid steels contain carbon in an amount from 0.8 to 2.14 %. Their structure represents a hardening sorbite with the precipitations of carbides on the boundaries of primary austenitic grains, the presence of which in the structure increases hardness and wear resistance [6]. An increase in carbon content in rail steels is limited by the ability to form a dangerous carbide network.

In equilibrium conditions, carbon in steel can be in a solid solution based on α- and γ-iron, in the composition of carbides, in the clusters of dislocations, on interphase and intraphase boundaries. Due to a high diffusion mobility at high temperatures, in the process of thermal and thermomechanical treatment, redistribution of carbon is possible. The problem of thermodynamics and the mechanism of decay of cementite and accelerated carbon transfer to defects of the structure during plastic deformation is considered in the monograph [7]. Redistribution of carbon between the structural components of steel, as well as the exit of the structure to defects in the conditions of high temperatures and plastic deformation is considered in the work [8]. The study of the evolution of the structure showed that in martensitic steel, an increase in carbon on defects in the structure at its reduction in α-iron at the same time. In steel with a bainite structure, the amount of carbon increases in α-iron, at the same time

Table 1. Chemical composition of rail Areal 136 HE-X steel (wt.%)

Element	C	Mn	Si	V	Ti	Cr	P	Al	S
According to the certificate	0.99–1.00	0.69–0.71	0.50–0.52	–	–	0.21–0.22	–	0.005	0.02
According to the results of spectral analysis	0.97	0.69	0.49	0.01	0.008	0.21	0.012	≤0.01	0.008

it decreases in γ-iron and in the particles of cementite, which are located in the volume of bainite plates, in addition, a transfer of carbon to crystalline structure defects occurs. It is known [9], that operation of railway rails is accompanied by a significant redistribution of carbon in a thin surface layer. If in the initial state the main carbon content is concentrated in the composition of cementite Fe_3C, then after a long-term operation of rails, the content of carbon is determined at dislocations, grain and subgrain boundaries.

Under thermodeformation conditions of FBW, the prerequisites for redistribution of carbon exist. The aim of the work was to determine the features of the microstructure of joints of hypereutectoid rail steels with an increased carbon content in FBW.

PROCEDURE AND EQUIPMENT

Welding of hypereutectoid rails of grade AREAL 136HE-X manufactured by Nippon Steel Corporation (Japan) was carried out in the K1000 machine for flash-butt welding using pulsating flashing. After optimization of conditions, the recommended parameters should be within the following values: welding time — 70–90 s, welding current — 360–390 A, tolerance for flashing — 10–14 mm, upsetting value — 11–14 mm. The grade composition and results of the spectral analysis of the delivered batch of rails are given in Table 1.

The macrostructure of the joints was revealed in accordance with the requirements of GOST R51685-2013 on a full-profile template, cut out in the transverse direction. Etching of polished specimens was carried out with an aqueous solution of ferric chloride. The microstructure was revealed by etching of preliminary polished specimens in a 4 % alcohol solution of HNO_3. Metallographic examinations were performed in the NEOPHOT 32 optical microscope equipped with a digital camera. To analyze the microstructure and determine the chemical composition of structural components, Auger-microprobe JAMP 9500F of JEOL Company (Japan) with the installed X-ray energy dispersive JNCA Penta FET x3 spectrometer of «Oxford Instrument» Company was used. The energy of the primary electron beam was 10 keV at a current of 0.5 nA for the REM and PCMA methods and a current of 10 nA for the method of Auger-electron spectroscopy. Auger-spectra were recorded with the energy resolution $\Delta E/E$ = 0.6 %. Prior to the studies, the surface of the specimens was subjected to cleaning directly in the analysis chamber of the device by etching with argon ions Ar + with an energy of 1 keV during 10 min. The etching rate over the reference specimen-witness SiO_2 was 4 nm/min. The vacuum in the analysis chamber was in the range of $5\cdot10^{-8}$–$1\cdot10^{-5}$ PA.

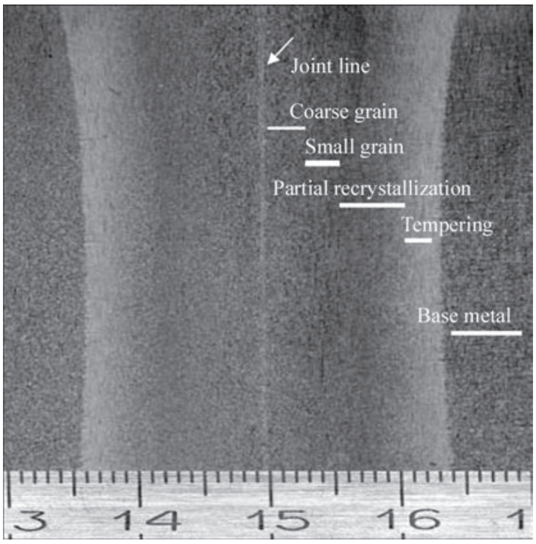

Figure 1. Microstructure of rail joint of steel of grade AREAL 136 HE-X (×25)

The Vickers hardness was measured in the NOVOTEST TC-GPB hardness tester with a load of 292.4 N (30 kg). The hardness distribution in the joint was investigated at a distance of 5 mm from the rolling surface of the rail.

RESULTS OF RESEARCH AND DISCUSSION

Metallographic examinations showed that macrostructure of the joint is similar to that of hypoeutectoid rails and consists of a weld zone, to which the zone of a coarse grain is adjacent, followed then by the zones of a fine grain, partial recrystallization and tempering (Figure 1). The width of the heat-affected zone (HAZ)

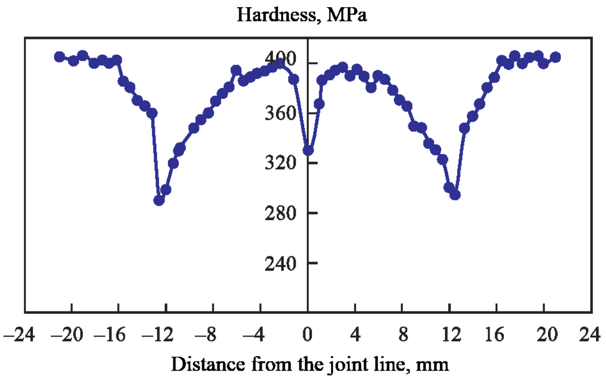

Figure 2. Distribution of Vickers hardness in the joint of the hypereutectoid rail steel of grade AREAL-136HE-X. Load is 30 kg

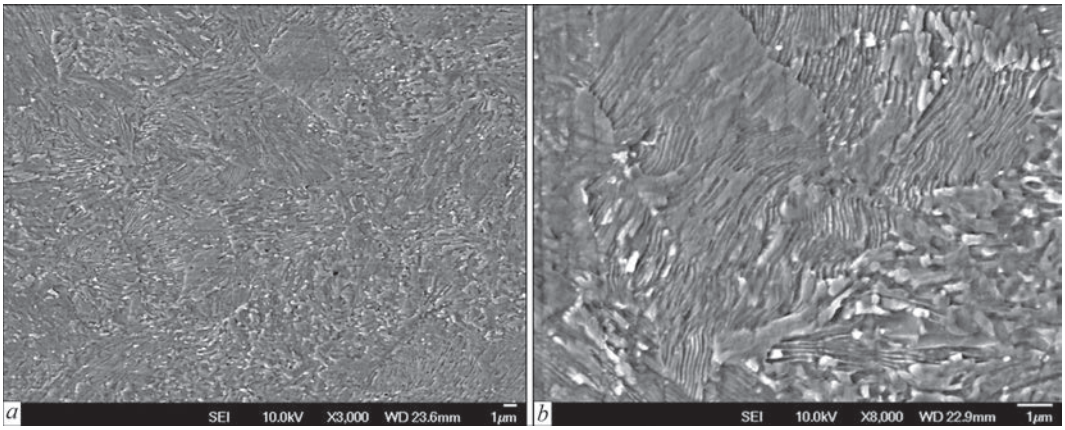

Figure 3. Microstructure of hypereutectoid steel of grade AREAL 136 HE-X: *a* — ×3000; *b* — ×8000

of the studied joint was 30 mm. Analysis of the hardness distribution showed (Figure 2) that in the zone of a coarse grain, unlike in the joints of hypoeutectoid rails, the hardness is slightly reduced as compared to the base metal — *HV* 3900 MPa and *HV* 4000 MPa, respectively.

The study of the microstructure showed that the base metal represents a hardening sorbite (Figure 3). The size of sorbite colonies is estimated at 10 μm. The interplate distance in sorbite is estimated at 0.14 μm. It should be noted that cementite plates in sorbite are deformed and refined.

During the analysis of the microstructure it was found that in the base metal along the grain boundaries, a structural component with a carbon content of 44.5 at.% is observed, the rest is iron. Its thickness is tenth fractions of a micron (Figure 4). The formation of a solid carbide network is not observed. The particles chaotically distributed in the matrix are observed, in the composition of which 68.4 at.% of carbon is recorded.

Taking into account the possible error while using the Auger-spectral method of analysis, it can be assumed that at the grain boundaries, a hypoeutectoid carbide phase is observed and in the structure of steel,

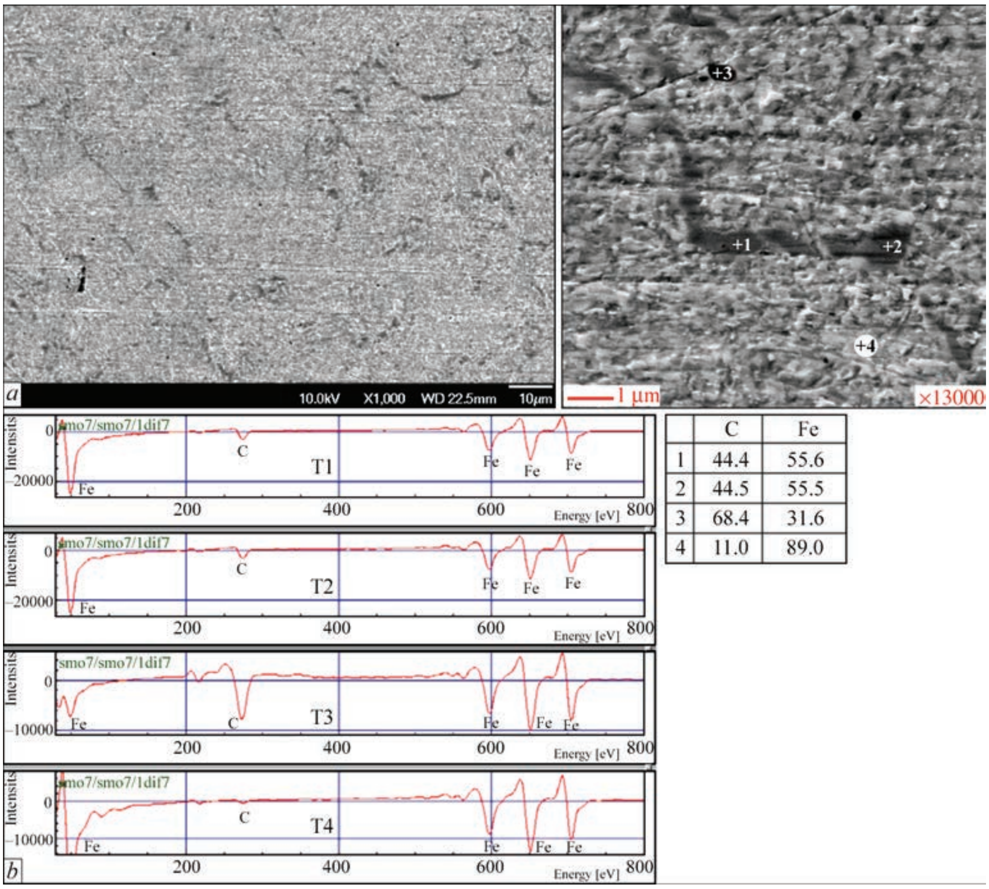

	C	Fe
1	44.4	55.6
2	44.5	55.5
3	68.4	31.6
4	11.0	89.0

Figure 4. Precipitations of carbide phase at the boundaries of grains of the hypereutectoid rail steel of grade AREAL 136 HE-X: *a* — microstructure; *b* — Auger-spectra and results of Auger-spectral analysis (at.%)

Table 2. Composition of nonmetallic inclusions in the Areal 136 HE-X steel (at.%)

Number	C	O	Mg	Al	Si	Ca	Mn	Fe
1	0.44	63.30	2.16	25.82	3.46	3.30	0.68	0.84
2	1.09	61.36	3.05	24.98	3.64	2.66	1.35	1.86
3	1.14	61.31	1.65	27.57	1.55	0.97	0.98	4.83
4	1.57	60.75	2.64	23.57	4.09	2.97	1.07	3.34
5	1.54	62.41	0.82	27.45	2.32	1.55	0.17	3.74
6	1.35	57.03	0.67	25.00	2.12	2.00	0.73	11.08

particles with carbon precipitations are present. It should be noted that the ratio of carbon and iron in the carbide phase does not correspond to the stoichiometric one in cementite: 75 at.% iron — 25 at.% carbon.

Contamination with nonmetallic inclusions is insignificant. Primarily, deoxidation products are observed unsystematically located in the matrix: aluminium oxides with impurities of calcium, silicon and magnesium (Table 2, Figure 5, *a*). Sulfides of up to 10 μm length (Figure 5, *b*) are observed, elongated along the direction of the rolled metal and dispersed aluminium carboxides with the size of less than 1 μm, not previously mentioned in the structure of rail steels (Figure 5, *c*).

The study of the metal in the HAZ showed that the microstructure represents a lamellar pearlite of varying degree of dispersion (Figure 6, *a*). The exception is the tempering zone, where coagulation of sorbite cementite occurs, resulting in a decrease in hardness in this region (Figure 6, *b*). At the recrystallization area along the boundaries of the primary austenitic grains, precipitations of a hypoeutecoid ferrite with a thickness of less than 1 μm are found (Figure 6, *c*). The presence of a hypoeutectoid ferrite is obviously a consequence of a decrease in carbon content in austenite formed during welding, which is lower than an eutectoid one.

Along the joint line as a result of depletion of the near-contact layer with carbon during flashing of the rail ends in welding, a band with a hypoeutectoid ferrite is formed at the boundaries of the primary austenitic grains (Figure 7). The band width is about 300 μm. According to the ASTM scale, the grain size of the primary austenite corresponds to a grain size number of 2–3. The interplate distance in sorbite is estimated at about 0.17 μm, which is much larger unlike that in the area of a coarse grain, which is 0.10 μm (Figure 6, *d*). The size of the interplate distance is the main factor that determines the level of hardness of steel. Accordingly, a significant decrease in hardness is observed along the joint line.

Despite the existing preconditions, carbides at the boundaries of primary austenitic grains were not detected in the joint, a number and sizes of chaotically distributed globular particles increased, that are similar to particles with precipitations of carbon in the base metal (Figure 8, *a*). According to the results of Auger-spectral analysis, the studied particles contained 84.2–92.8 at.% C, the rest was the iron (Figure 8, *b*). Their number increases in the direction of the butt joint, the highest concentration is observed in the near-contact layer.

The interplate distance in sorbite determines the hardness of steel — its reduction leads to an increase in hardness. In the base metal and in the area of a coarse grain, the interplate distance is 0.14 and 0.10 μm, respectively. However, the hardness in the area of a coarse grain is lower than that of the base metal — 3900 and 4000 MPa, respectively. Apparently, this is associated

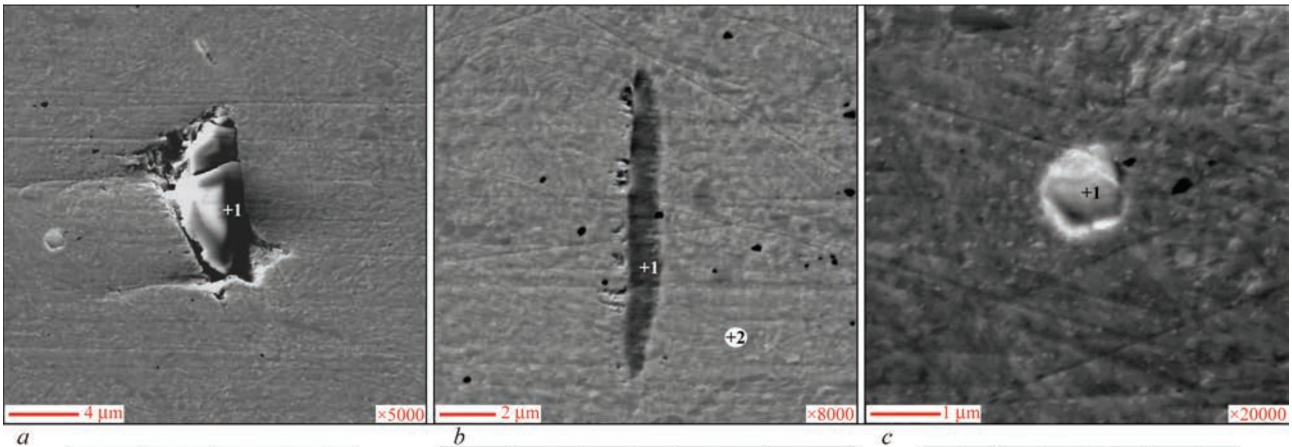

a

C	O	Fe	Al
0.6	72.0	1.1	26.3

b

	C	S	Fe	Mn
1	1.0	43.6	15.9	19.3
2	13.8	0	86.2	0

c

C	O	Fe	Al
33.4	46.6	0.7	19.3

Figure 5. Nonmetallic inclusions of hypereutectoid steel of grade AREAL 136 HE-X and results of the Auger-spectral analysis (at.%) of: *a* — aluminium oxide; *b* — sulfide; *c* — aluminium carboxide

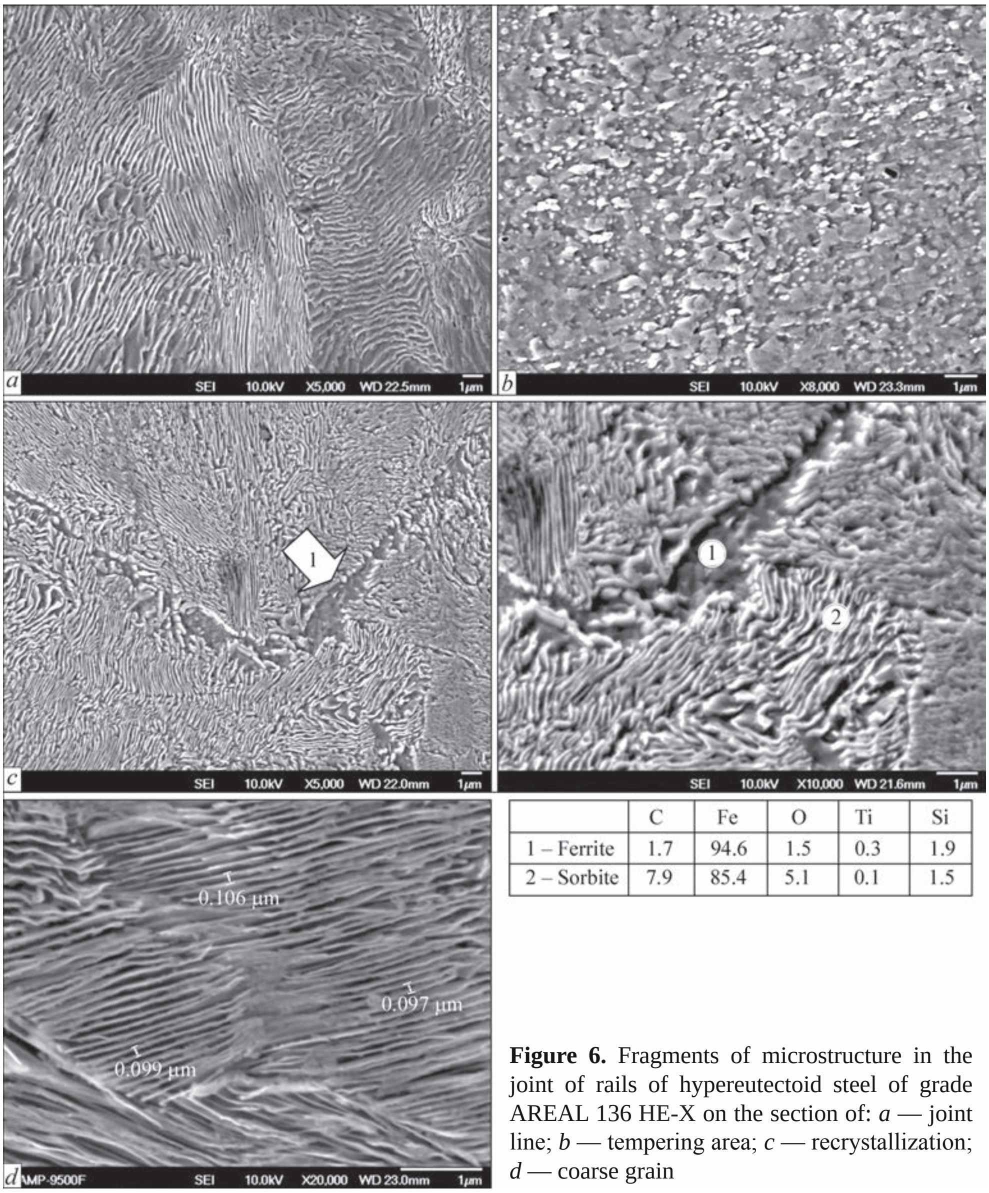

	C	Fe	O	Ti	Si
1 – Ferrite	1.7	94.6	1.5	0.3	1.9
2 – Sorbite	7.9	85.4	5.1	0.1	1.5

Figure 6. Fragments of microstructure in the joint of rails of hypereutectoid steel of grade AREAL 136 HE-X on the section of: *a* — joint line; *b* — tempering area; *c* — recrystallization; *d* — coarse grain

with the presence in the base metal of the carbide phase at the boundaries of the primary austenitic grains and its absence in the structure of the joint.

Fractographic examinations showed that on the fracture surface of the joint, carbon is present primarily around nonmetallic inclusions (Figure 9, *a*, *b*). The presence of formations of the C–N–O system should be noted adjacent to carbon and containing 54.91–61.36 at.% of carbon; 14.65 at.% of nitrogen; 8.39 at.% of oxygen (Figure 9, *c*).

It is believed that carbon in the structure of carbon steels and cast irons is present in the composition of chemical compounds (carbides), solid iron solution, as well as in the form of the main allotropic modifica-

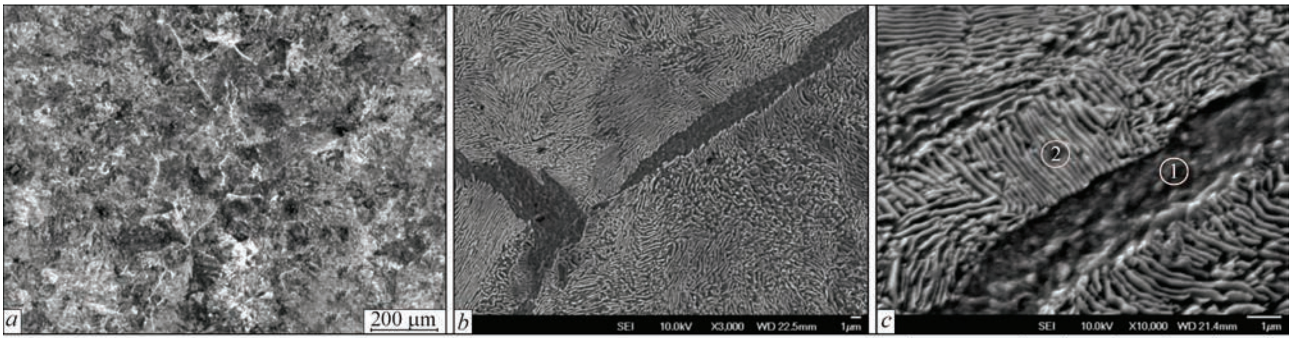

Point	C	O	Fe	Ti	Si
1 –Ferrite	1.0	3.3	94.4	0.5	1.0
2 – Sorbite	6.1	2.2	90.6	0.7	0.5

Figure 7. Joint line of rails of hypereutectoid steel of grade AREAL 136 HE-X: *a*, *b* — microstructure (×100, ×3000); *c* — results of Auger-spectral analysis (at.%)

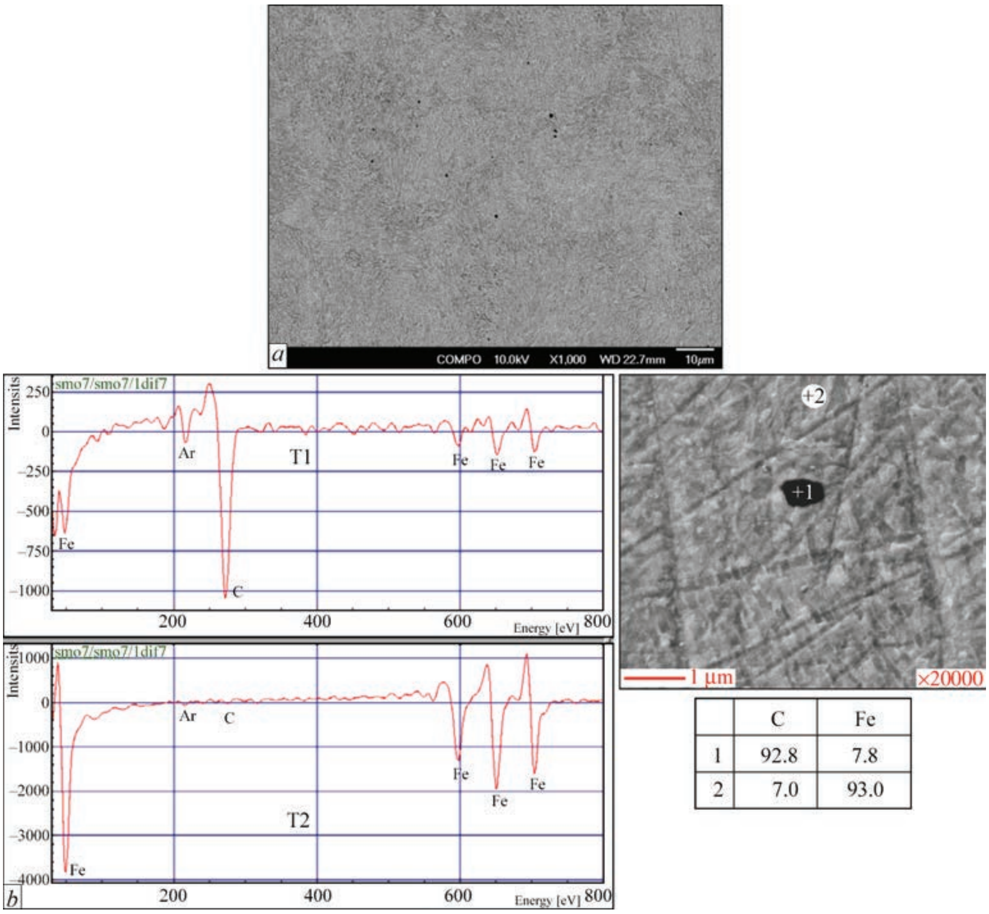

	C	Fe
1	92.8	7.8
2	7.0	93.0

Figure 8. Inclusions of carbon in the joint of rails of hypereutectoid steel of grade AREAL 136 HE-X: *a* — location in the microstructure; *b* — Auger-spectra and results of Auger-spectral analysis (at.%)

tion — graphite. However, in the studies of a number of authors based on experimental data, it was shown that in the alloys of the Fe–C system, carbon can be present in the states that do not meet the abovementioned variants [10]. In particular, in welded joints fullerenes were revealed — a molecular form of carbon [11]. The obtained results of fractographic examinations give reasons to suggest the existence of carbon modifications different from graphite in the structure of rail joints.

Carbon inclusions can be considered as a violation of metal continuity. Taking into account their small amount, sizes and a globular shape, a significant decrease in strength characteristics is not envisaged.

The tests on static bending during tension of the foot with a load of 1740–2400 kN were carried out.

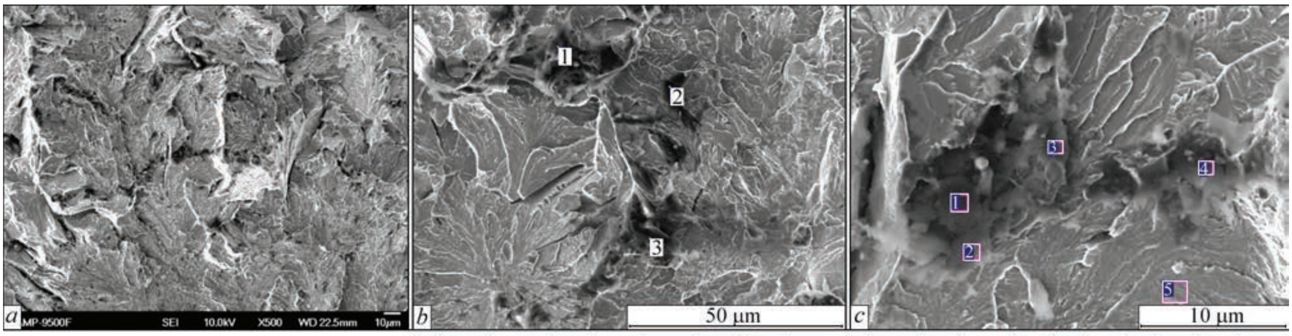

	C	O	Na	Si	S	Cl	Ca	Fe
1	82.86	6.62	0.79	0.39	0.16	0.28	0.24	8.67
2	81.20	12.97	0.23	0.21	0.07			5.32
3	64.02	7.44	0.51	0.35				27.68

	C	N	O	Na	Mg	Al	Si	S	Mn	Fe
1	59.66	19.32	15.42	0.50		0.45	0.52	1.97	0.04	2.12
2	54.91	14.65	8.92	0.56			0.43	1.21	0.08	19.75
3	55.72	15.48	8.39	0.28	0.11		0.40	1.39	0.50	17.75
4	61.36	15.85	13.22	0.62	0.19	0.64	0.66	0.90	0.27	5.76
5	11.78		2.82				1.53		0.88	82.99

Figure 9. Inclusions of carbon on the fracture surface of the joint of hypereutectoid rail steel AREAL 136 HE-X: *a* — microstructure of the fracture surface; *b* — inclusions of carbon and results of X-ray microanalysis (at.%); *c* — inclusions of the C–N–O system and results of X-ray microanalysis (at.%)

The bending deflection was 26–43 mm. The results of tests, as well as the size of the HAZ meet the requirements of domestic [12] and European [13] standards.

CONCLUSIONS

1. The microstructure of the joint of the hypereutectoid rail steel of grade AREAL-136HE-X, produced by flash-butt welding, represents a lamellar pearlite of a different degree of dispersion. The exception is the tempering area where coagulation of sorbite cementite occurs. Along the joint line as a result of depletion of the near-contact layer in flashing of rail ends during welding, at the boundaries of primary austenitic grains, a band with a hypoeutectoid ferrite is formed. Hypoeutectoid ferrite in a small amount is also observed in the area of recrystallization. Carbides at the boundaries of primary austenitic grains were not detected in the joint. At the same time, in the microstructure globular particles with a high carbon content are observed.

2. The results of examinations of the microstructure evidence that in the thermodeformation conditions of FBW, redistribution of carbon occurs, the result of which is its transfer to defects of the structure. In this time, carbon content in the matrix decreases and recrystallization in the HAZ metal occurs similarly to hypoeutectoid rail steels.

3. Investigation of hardness distribution showed that in the area of a coarse grain, unlike the joints of hypoeutectoid rails, the hardness is reduced as compared to the base metal — *HV* 3900 MPa and *HV* 4000 MPa, respectively. This is caused by the absence of the area of a coarse grain, carbide phase at the boundaries of primary austenitic grains for the microstructure unlike the base metal.

4. The results of tests of the hypereutectoid rail steel of grade AREAL-136HE-X on static bending meet the requirements of domestic and European standards. The use of FBW to produce high-quality joints of the rails of a hypereutectoid composition is recognized as challenging.

REFERENCES

1. Kuchuk-Yatsenko, S.I. (1992) *Flash-butt welding*. Kyiv, Naukova Dumka [in Russian].
2. *Fujll* Mitsuru, Nakanowatari Hiroaki, Narial Kiyoshi (2015) *Rail Flash-Butt Welding*. Jfe Technical Report No. 20, March. https:WWW jfe-steel.co.jp
3. S. Kendji, F. Hiroshi, T. Yasunobu (2014) Method of flash-butt welding of rail steel. *Nippon Steel and Sumitomo Metal Corp. No. 216.012 A172/20.02.2014.* https://edrid.ru/en/rid/216/012/a172.html
4. Kuchuk-Yatsenko, S.I. (2018) Technologies and equipment for flash-butt welding of rails: 60 years of continuous innovations. *The Paton Welding J.*, **11-12**, 29–44. DOI: https://doi.org/10.15407/tpwj2018.12.03.
5. Kuchuk-Yatsenko, S.I., Didkovsky, O.V., Bogorsky, M.V. et al. (2002) *Flash-butt welding*. Ukraine Pat. 46820 6B23K11/04, C2, Russia Pat. 2222415 of 2003, US Pat. 6.294.752 of 2001, Great-Britain Pat. GB235725.9A of 20.06.01, China Pat. ZL00101672/5, of 2004.
6. Gulyaev, A.P. (1977) *Metals science: Manual for Higher Education Inst.*, Moscow, Metallurgiya [in Russian].
7. Gavrylyuk, V.G. (1987) *Distribution of carbon in steel*. Kyiv, Naukova Dumka [in Ukrainian].
8. Aksenova, K.V., Gromov, V.E., Ivanov, Yu.F. et al. (2017) Carbon redistribution under deformation of steels with bainite and martensite structures. *Izv. Vuzov, Chyorn. Metallurgiya*, 60(**7**), 544–548 [in Russian]. DOI: https://doi.org/10.17073/0368-0797-2017-7-544-548.
9. Yuriev, A.A., Ivanov, Yu.F., Gromov, V.F. et al. (2017) Redistribution of carbon in structure of rail steel after long operation. *Vestnik SibGIU*, **4**, 22, UDK 669.539.382.17 [in Russian] https://cyberleninka.ru/article/n/pereraspredelenie-ugleroda-v-strukture-relsovoy-stali-po
10. *Belous M.V.*, Novozhilov, V.B., Shatalova, L.A., Shejko, Yu.P.(1995) *Distribution of carbon by state in tempered steel*. *FMM KPI*, 79(**4**), 128–137 [in Russian].
11. Zakirpichnaya, M.M., Kuzeev, I.R., Tkachenko, O.I. (1999) Distribution of fullerenes by zones of welded joint. *Svarochn. Proizvodstvo*, **11** [in Russian]. http://library.nuft.edu.ua/ebook/file
12. TU U 27.1-40081293-002:2016. *New welded rails for railways*. Dnipro, NDKTI Ukrzaliznytsia [in Ukrainian].
13. DIN EN 14587-2:2009 (E). *Railway applications - Track - Flash butt welding of rails. Pt 2:* New R220, R260, R260Mn and R350HT grade rails by mobile welding machines at sites other than a fixed plant. URL://https://www.en-standard.eu/din-en14587-2-railway-applications-track-flash-butt-welding-of-rails-part-2-new-r220-r260-r260mn-and-r350ht-grade-railsby-mobile-welding-machines-at-sites-other-than-a-fixed-plant

ORCID

V.I. Shvets: 0000-0003-4653-7453,
O.V. Didkovskyi: 0000-0001-5268-5599,
Ye.V. Antipin: 0000-0003-3297-5382
I.V. Zyakhor: 0000-0001-7780-0688

CONFLICT OF INTEREST

The Authors declare no conflict of interest

CORRESPONDING AUTHOR

I.V. Zyakhor
E.O. Paton Electric Welding Institute of the NASU
11 Kazymyr Malevych Str., 03150, Kyiv, Ukraine
E-mail: zyakhor@paton.kiev.ua

SUGGESTED CITATION

V.I. Shvets, O.V. Didkovskyi, Ye.V. Antipin, I.V. Zyakhor, L.M. Kapitanchuk, Wang Qichen (2022) Features of microstructure of joints of hypereutectoid AREAL-136HE-X rail steel in flash-butt welding. *The Paton Welding J.*, **3**, 34–40.

JOURNAL HOME PAGE

https://pwj.com.ua/en

Received: 27.01.2022
Accepted: 16.05.2022

https://doi.org/10.37434/tpwj2022.03.05

EXPERIMENTAL STUDIES OF BIFILAR ELECTROSLAG WELDING WITH AN EQUALIZING WIRE

Yu.M. Lankin, O.P. Bondarenko, V.G. Tyukalov, V.G. Soloviov, I.Yu. Romanova

E.O. Paton Electric Welding Institute of the NASU
11 Kazymyr Malevych Str., 03150, Kyiv, Ukraine

ABSTRACT

At bifilar electroslag welding, compared to the traditional two-electrode circuit, the path of current flowing in the slag pool is significantly different, and, consequently, the position of heat evolution zones and electromechanical forces acting on the molten slag and metal, changes drastically. Experiments showed that at bifilar electroslag welding penetration of the edges of welded item metal is considerably smaller, and reduction of the welding gap becomes possible that allows raising the welding speed at the same power, and power factor cos φ increases essentially from 0.67 to 0.9. Connection of equalizing wire between the midpoint of output winding of power transformer and the item being welded ensures stability of the electroslag welding process by the bifilar circuit of power source connection.

KEYWORDS: electroslag welding, bifilar power circuit, edge penetration, process stability, power factor

INTRODUCTION

Electroslag welding (ESW) is performed with application of one, two, three and more electrode wires. In two-electrode machines the electrode wires are connected to the power source in parallel by electrode–welded item circuit. Such a connection is believed to be traditional. At electroslag remelting (ESR) with two electrodes the bifilar circuit of electrode connection to the power source became widely accepted [1–5]. Bifilar ESR has certain advantages over ESR with electrodes connected in parallel. Bifilar ESW by wire electrodes is not applied now. However, there is ground to believe that it has even more advantages over bifilar ESR. As the cross-sectional area of consumable electrodes in ESW and ESR differs considerably, the thermophysical processes, causing their melting, also differ essentially. Compared to the traditional circuit with two electrodes, at bifilar ESW the path of current flowing in the slag pool changes significantly, and, consequently, the position of heat evolution zones, electromechanical forces acting on molten slag and metal, also changes dramatically. Therefore, a physical experiment is required to study the process of bifilar ESW. We are not aware of any publications on conducting ESW with the bifilar circuit of unit connection to the power source, except for the experiment on the mathematical model [6, 7].

The objective of experimental studies is comparison of the results of ESW by bifilar scheme of connection to the power source and traditional two-electrode connection circuit. The anticipated results of the work can be useful for different mechanical engineering industries, as they will create real conditions for increasing ESW productivity and operational efficiency of welded joints of carbon, low- and medium-alloyed steels of large thickness (40–250 mm).

MATERIALS, METHODS AND RESULTS OF EXPERIMENTS

The work was performed under the conditions of PWI laboratory*. In order to check the equipment performance and welding procedures, experimental studies of bifilar ESW with an equalizing wire were performed in comparison with the traditional ESW circuit with two wire electrodes. Experiments were performed in a unit, fitted with A-535 machine with liquid metal level regulator, level sensor and digital meter of electrode wire feed speed, as well as power transformer TShS-1000/3 with thyristor voltage stabilizer at the high-voltage side. The unit circuit enabled operation by the traditional or bifilar power circuit with zero wire.

Experiments were conducted using samples from low-carbon structural steel 70 mm thick, sample dimensions were 420×200×70 mm. Welding wire of 3 mm diameter and flux of AN-8 grade were used as welding consumable. In all the experiments number of electrodes was 2, interelectrode distance was $d =$ $= 55$ mm, dry electrode extension was 90 mm. Welding by the traditional and bifilar circuit was conducted at practically same power P and electrode feed rate V_f, same gaps b and slag pool depths h_{sl}. One welding operation was purposefully performed in a narrow gap ($b = 20$ mm) to determine the possibilities of the bifi-

---

*O.A. Moskalenko took part in the work performance.

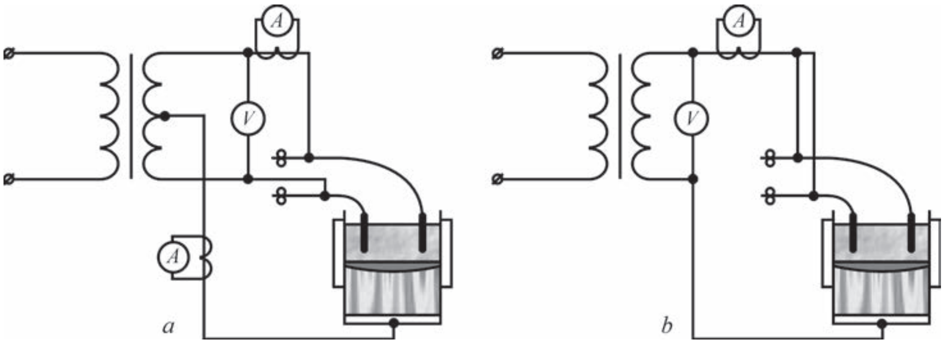

Figure 1. Experimental circuits of bifilar ESW with an equalizing wire (*a*) and traditional ESW (*b*)

Table 1. Main parameters of welding modes

Parameter description	Sample number			
	1	2	3	4
Power circuit	Bifilar	Traditional	Bifilar	Traditional
Welding gap *b*, mm	32	32	20	32
Interelectrode distance *d*, mm	55	55	55	55
Welding voltage *U*, V	76	38	76	55
Wire feed rate V_f, m/h	230	240	235	230
Welding speed V_w, m/h	1.45	1.51	2.37	1.45
Electrode current *I*, A	500	960	520	1120
Equalizing current h_{eq}, A	0	-	60	-
Slag pool depth h_{sh}, mm	50	55	40	50
Power applied to the slag pool *P*, kW	38	36.5	39.5	61.6
Power factor cos φ, rel. un.	0.9	0.7	0.89	0.68
Edge penetration depth, mm	8	13	7	22

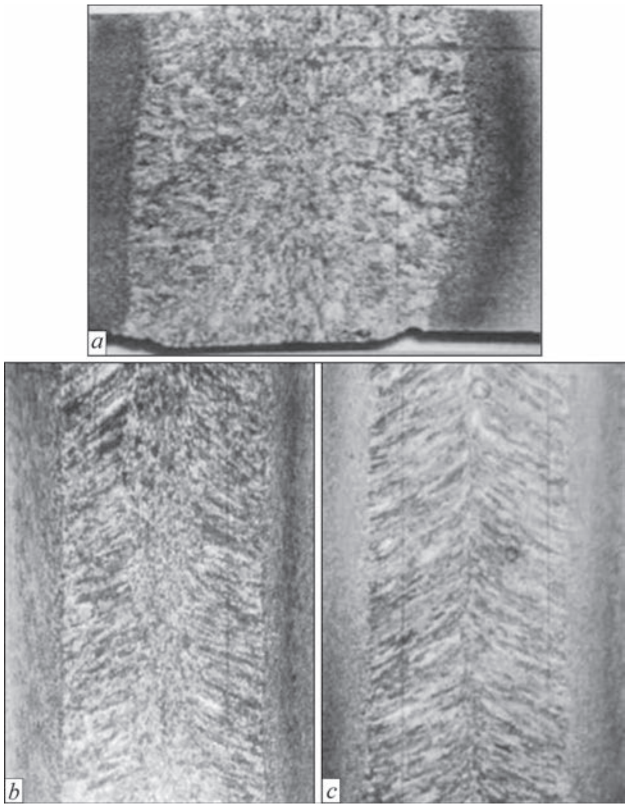

Figure 2. Macrosections of sample No.1: *a* — transverse macrosection of welded joint made with bifilar circuit (*b* = 32 mm); *b* — longitudinal macrosection (section under the electrode); *c* — longitudinal macrosection (section between the electrodes)

lar power circuit. Another ESW operation by the traditional scheme was performed at a higher (1.7 times) welding power at practically the same electrode feed rate. All the electric mode parameters were recorded in keeping with Figure 1.

The main parameters of the welding modes are given in the Table 1, and welded joint macrosections are shown in Figures 2–5.

DISCUSSION

The electroslag process was stable in welding all the samples (Nos 1–4). It is known that the process of single-electrode ESW with power supply from a source with rigid external characteristic is stable, as it has the self-regulation property, similar to the consumable electrode arc welding process. In bifilar ESW without the equalizing wire self-regulation is absent and such a process is unstable at the action of disturbances on it, which are inevitable under the real conditions. Application of equalizing wire, as shown in Figure 1, *a*, ensured self-regulation, and, hence, also the stability of bifilar ESW without the automatic regulation systems with negative feedbacks.

When using the bifilar power circuit of ESW with an equalizing wire, the process of "cold" start is essentially simplified and shortened, compared to the traditional ESW with two wire electrodes. At this stage,

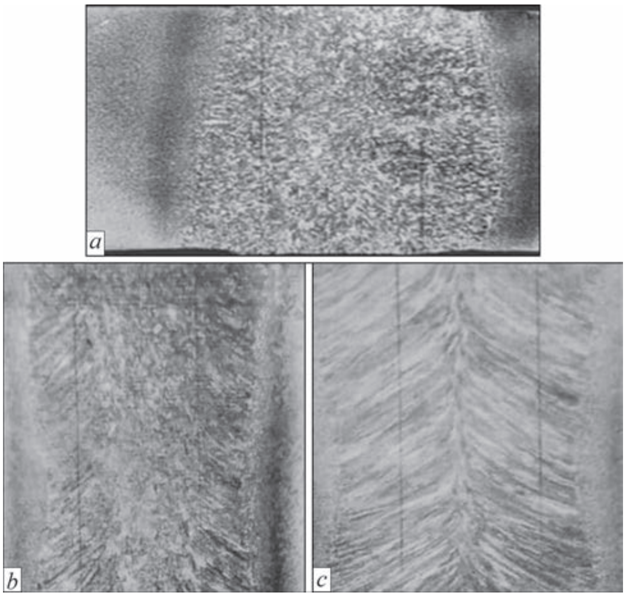

Figure 3. Macrosections of sample No.2: *a* —transverse macrosection of welded joint made by ESW with the traditional circuit ($b = 32$ mm); *b* — longitudinal macrosection (section under the electrode); *c* — longitudinal macrosection (section between the electrodes)

each electrode is powered practically individually from its half of the transformer secondary winding, and slag melting is performed by two electric arcs simultaneously, burning between the electrode edges and inlet pocket. At this stage, all the current runs through the equalizing wire. After slag melting, it becomes electrically conducting, and the electric arc process turns into the electroslag one. Gradually, an ever greater part of the total current starts flowing between the electrodes, and current in the equalizing wire decreases to zero. Only at very small welding gaps current, which is due to currents between the electrodes and edges of the item being welded, can flow continuously through the equalizing wire. This current is small, for instance, in welding sample No.3 (welding gap of 20 mm), it was equal to 12 % of the total welding current.

One of the main advantages of ESW bifilar power circuit is smaller depth of the edges of item being welded. As one can see from the Table 1, the penetration depth of the edges of item being welded at ESW by the bifilar circuit (sample No.1) is by 40 % smaller than that of penetration of the edges at ESW by the traditional circuit (sample No.2) at other welding conditions being equal.

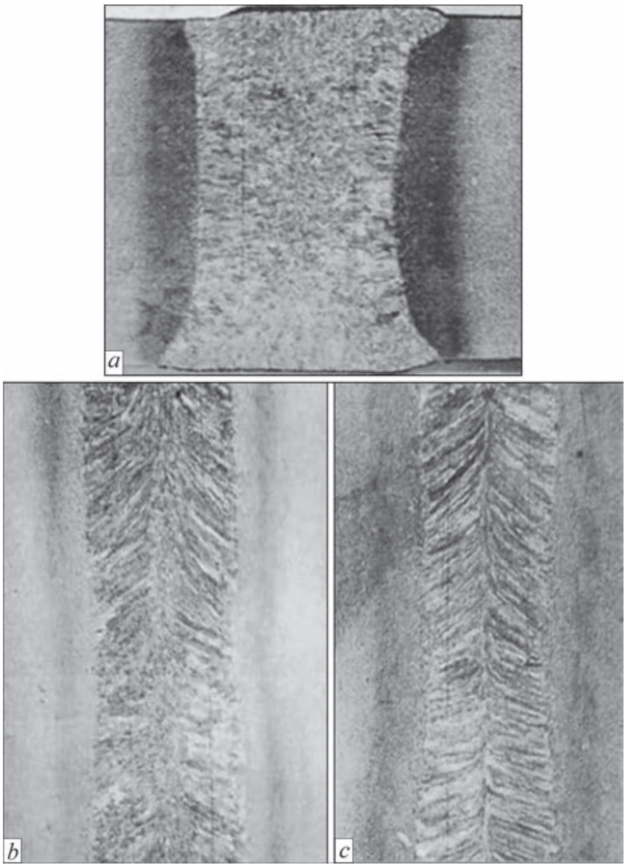

Figure 4. Macrosections of sample No.3: *a* — transverse macrosection of welded joint made by ESW by bifilar circuit ($b =$ $= 20$ mm); *b* — longitudinal macrosection (section under the electrode); *c* — longitudinal macrosection (section between the electrodes)

Another important advantage of bifilar ESW is the possibility of welding into a narrow gap of 20 mm (sample No.3) that allowed increasing the welding speed by 63 %, compared to sample No.1, at the same power.

A thinner macrostructure of welds made by the bifilar power circuit is noted. The presence of two different macrostructures in the sections under the electrodes and between the electrodes was established both with the traditional and the bifilar power circuit:

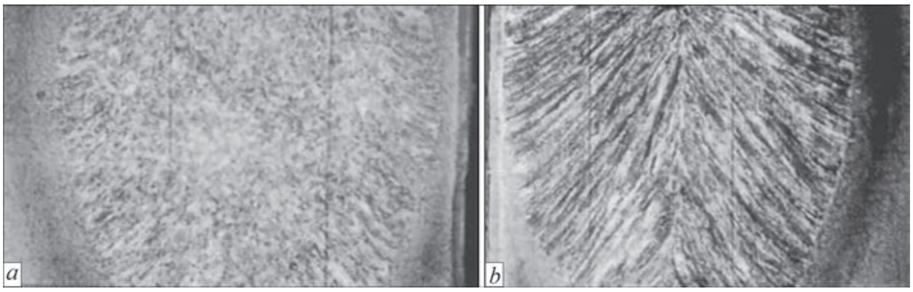

Figure 5. Longitudinal macrosections of welded joint on sample No.4 made by ESW by the traditional circuit, at higher power (1.7 times higher): *a* — section under the electrode; *b* — section between the electrodes

- dendritic and disoriented cellular-dendritic macrostructure under the electrodes;
- coarse dentritic macrostructure between the electrodes (for all the welds in different gaps).

However, in sample No.4 the coarse dendritic macrostructure is more expressed, compared to sample No.2. It is envisaged that at traditional ESW direct flowing of current (electrode-bottom plate) may lead to slag overheating, and, accordingly, metal pool deepening that does not allow increasing the linear welding speed (“hot” cracks can form in the weld, so-called critical ESW speed).

At bifilar power circuit of ESW the respective relative arrangement of power cables, connecting the power source to the welding machine, enables a significant reduction of inductance of the power source secondary circuit. As a result, for instance, for our welding unit power factor cos φ increased from 0.7 for the traditional circuit to 0.9 for ESW bifilar power circuit. Such an increase of power factor greatly decreases the load on the external electrical network and reduces power losses.

CONCLUSIONS

ESW by the bifilar circuit allows redistributing the components of thermal balance in the slag pool. Here, it is possible to essentially increase the welding speed without any negative consequences for weld metal quality.

Equalizing wire ensures stability of ESW process with a bifilar power circuit.

The depth of penetration of edges of the item being welded is much smaller with ESW bifilar circuit, than with the traditional two-electrode ESW circuit.

It became possible to use 20 mm gaps between the edges that greatly improved the energy values of ESW process at a considerable increase of linear welding speed.

Finer macrostructure of the welds, made by the bifilar power circuit, is noted.

At transition from ESW traditional power circuit to the bifilar one with an equalizing wire cos φ of the unit increased abruptly (from 0.7 up to 0.9) that may ensure an improvement of operating conditions of the unit external network.

REFERENCES

1. Medovar, B.I., Stupak, L.M., Bojko, G.A., (1976) *Electroslag furnaces.* Ed. by B.E. Paton. Kyiv, Naukova Dumka [in Russian].
2. Jing, Xie (2008) Structure advantage of a 5-t double pole series circuit electroslag furnace. *Heavy Casting and Forging*, 5(**3**), 43–45 [in Chinese].
3. Xi-min, Zang, Tian-yu, Qiu, Xin, Deng et al. (2015) Industrial test of a 6-m long bearing steel ingot by electroslag remelting with drawing process. *China Foundry*, 12(**3**), 202–207.
4. Tezuka, M., Yamamoto, S., Takahashi, F. et al. (2014) Internal quality of 2150 mm-diameter ingot manufactured using new 150-ton ESR furnace. In: *Proc. of the 19th Int. Forgemasters Meeting – IFM (Tokyo, Japan, 29.09–03.10)*, 90–94.
5. Son, I., Lee, W., Sim, Kw. et al. (2014) Installation of 150-ton new ESR facility and production of 120-ton ESR ingot for 12Cr HIP rotor forgings. In: *Proc. of the 19th Int. Forgemasters Meeting — IFM (Tokyo, Japan, 29.09–03.10)*, 333–337.
6. Lankin, Yu.M., Soloviov, V.G., Tyukalov, V.G., Romanova I.Yu. (2021) Comparison of the processes of electroslag welding at power connection by mono- and bifilar circuits. *The Paton Welding J.*, **11**, 22–28.DOI: https://doi.org/10.37434/tpwj2021.11.04
7. Soloviov, V.G., Lankin, Yu.M., Tyukalov, V.G., et al. (2022) Prediction of weld parameters in ESW with a bifilar circuit of power source connection. *Avtomatich. Svarka*, **1**, 49–53 [in Ukrainian]. DOI: https://doi.org/10.37434/as2022.01.08.

ORCID

Yu.M. Lankin: 0000-0001-6306-8086,
V.G. Tyukalov: 0000-0003-3491-193X,
V.G. Soloviov: 0000-0002-1454-7520,
I.Yu. Romanova: 0000-0001-7154-1830

CONFLICT OF INTEREST

The Authors declare no conflict of interest

CORRESPONDING AUTHOR

Yu.M. Lankin
E.O. Paton Electric Welding Institute of the NASU
11 Kazymyr Malevych Str., 03150, Kyiv, Ukraine
E-mail: lankin.y.n@gmail.com

SUGGESTED CITATION

Yu.M. Lankin, O.P. Bondarenko, V.G. Tyukalov, V.G. Soloviov, I.Yu. Romanova (2022) Experimental studies of bifilar electroslag welding with an equalizing wire. *The Paton Welding J.*, **3**, 41–44.

JOURNAL HOME PAGE

https://pwj.com.ua/en

Received: 10.12.2021
Accepted: 16.05.2022

https://doi.org/10.37434/tpwj2022.03.06

INDUCTORS FOR HEAT TREATMENT OF WELDED BUTT JOINTS OF RAILWAY AND TRAM GROOVED RAILS

Ye.O. Panteleimonov

E.O. Paton Electric Welding Institute of the NASU
11 Kazymyr Malevych Str., 03150, Kyiv, Ukraine

ABSTRACT

The aim of the work is to create inductors for heat treatment of welded butt joints of railway and tram grooved rails. For heat treatment of welded butt joints of railway rails, the inductors were proposed, located opposite each other on the two sides of the rail. Investigation of local heating of railway and tram grooved rails with a frequency of 2.4 kHz showed that the inductors provide a uniform heating of cross-section rail elements, a low difference in the temperature between the surface and deep layers of the metal in the head of the rails and a decrease in heating time from the workshop temperature to the normalization temperature.

KEYWORDS: rails, rail welded butt joints, heat treatment, induction heating, inductors

INTRODUCTION

The reliability and service properties of the rail track depend to a large extent on the quality of welded butt joints of the rails. Under the conditions of high loads and speed of railway transport, welded butt joints are damaged more often than the base metal of the rails. The negative impact of welding is manifested in the appearance of a local decrease in hardness, unfavourable diagram of inner residual stresses across the HAZ, changes in the uniformity of microstructure, creation of conditions for arising inner defects, which are stress concentrators and weaken the sections of rails with a welded butt joint [1]. The most effective mean to improve the quality of welded butt joints is heat treatment. It consists in the local heating of welded butt joints and share of the base metal adjacent to them, to the normalization temperature of 850–950 °C, cooling of the web and the foot in a calm air and hardening of the rolling surface of the head with a compressed air. A high rate of local heating is provided by an induction method of heating metals by high frequency currents [2, 3]. Now, while performing the heat treatment of welded butt joints of railway rails in track and workshop conditions, the local heating of rails is performed by the currents of 8.0–16.0 kHz frequency. As a power source, frequency converters on IGBT transistors are used. The composition of the heating devices includes inductors without magnetic conductors. The technology and equipment provide heating of welded butt joints of railway rails of type R65 from different grades to the normalization temperature within a time of up to 240 s. The width of the HAZ in the head of the rails reaches 80–94 mm, in the foot of the rails it is 140–150 mm [4, 5].

The feasibility of heat treatment of welded butt joints exists for both railway rails as well as rails of other types of rail transport — tram, subway, crane, etc. The rails differ between each other in the shape of a cross-section, metal volume in individual elements and conditions of heat removal in the cold mass of metal. The railway rails have a symmetrical cross-section shape relative to the vertical axis. Tram grooved rails, unlike railway, are equipped with a groove and a lip. A rolling surface, a groove and a lip are displaced relative to the vertical axis. Depending on the method of welding — flash-butt, induction, alumothermic, electric arc, welded butt joints of rails have different width of the HAZ. For example, the width of the HAZ of welded butt joints of railway rails of type R65, produced by flash-butt welding, is 26–32 mm [6], tram grooved rails of type RT62, produced by automatic arc welding with the consumable nozzle, have a width of 45–55 mm. In order to relief inner stresses in the metal of rails, resulting from nonuniformity of volumetric changes in the heating process, it is necessary to provide the same temperature of cross-section rail elements and a low temperature between the surface and deep layers of metal at the end of the heat treatment of welded butt joints. Taking into account the specific features of the effect of high-frequency currents during heating products of a complex shape, certain requirements arise specified to the design of inductors of heating devices and current frequency. Inductors of heating devices should create an appropriate distribution of induced current on the surface of rails and its density, taking into account the conditions of heat removal into the cold mass of metal and not causing overheating of protruding rail elements — feathers and the upper edge of the lip. To achieve a low temperature difference between the surface and deep layers of the rails, it is advisable to increase the depth of current penetration into the metal, i.e. reduce the current frequency.

AIM OF THE WORK

The aim of the work is to create inductors of heating devices for heat treatment of welded butt joints of railway and tram grooved rails, providing a uniform heating of cross-section rail elements and a low temperature drop between the surface and deep layers of metal in the rail head.

DESCRIPTION AND DESIGN FEATURES

Figure 1, *a* shows the scheme of a heating device for heat treatment of welded butt joints of railway rails. The heating device includes inductors *1* and *2* of the same design [7]. The inductors are arranged opposite each other on two sides of the rail *3*. The shape of inducing wires of the inductors repeats the bending shape of the rail surface over the rolling surface of the head, side surfaces of the head, the web and the foot. The width of inducing wires and air gaps to the surface of the rails depend on the width of the HAZ of welded butt joints and the volume of cross-section rail elements. At a small gap, the induced current is concentrated, approximately, across the width of the inducing wire and at a large gap it extends to a considerable width. To enhance the proximity effect, as a result of which the density of induced current is increased, inductors are produced with the smallest air gaps over the head and the foot of the rails and slightly enlarged gaps above the web of the rails. A significant increase in the air gap over the rail feathers leads to a significant decrease in the density of induced current in these elements. Inducing wires of the inductors consist of two parallel wires. This provides an achievement of redistribution of the magnetic field across the width of the inductive wire and approaching the density of inducing current to the outer ends of the inducing wire. The total width of the wires in the inductors for heat treatment of welded butt joints of the rails of type R65 is 60 mm. It is larger than the width of the HAZ and the share of the base metal of the rails that adjacent to it, after flash-butt and automatic arc welding with a consumable nozzle. For the concentration of heating on the side surfaces of the cross-section elements and an overall increase in the efficiency coefficient of the system inductor–rail, magnetic conductors *4* are used, mounted over the rolling surface of the head, side surfaces of the head, the web and a part of the foot of the rail. Magnetic conductors consist of a set of plates of a transformer steel.

Inductors *1* and *2* of the heating devices for heat treatment of welded butt joints of tram grooved rails [8] have different design (Figure 1, *b*). Inducing wire of the inductor 1, mounted on the side of the head of the rail *3*, is extended only before the beginning of the groove *5*. This prevents overheating of the lip, as the magnetic flow into the depression of the groove is weakened by a large air gap. The shape of the inducing wire repeats the bending shape of the rail surface over the rolling surface of the head, the side surface of the head, the web and a part of the foot. The air gaps are enlarged over the web and significantly increased over the rail feathers. Magnetic conductors *4* are mounted over the rolling surface of the head, the side surface of the head, the web and a part of the foot. The inducing wire of the inductor *2*, mounted on the side of the lip *6*, repeats the bending shape of the rail

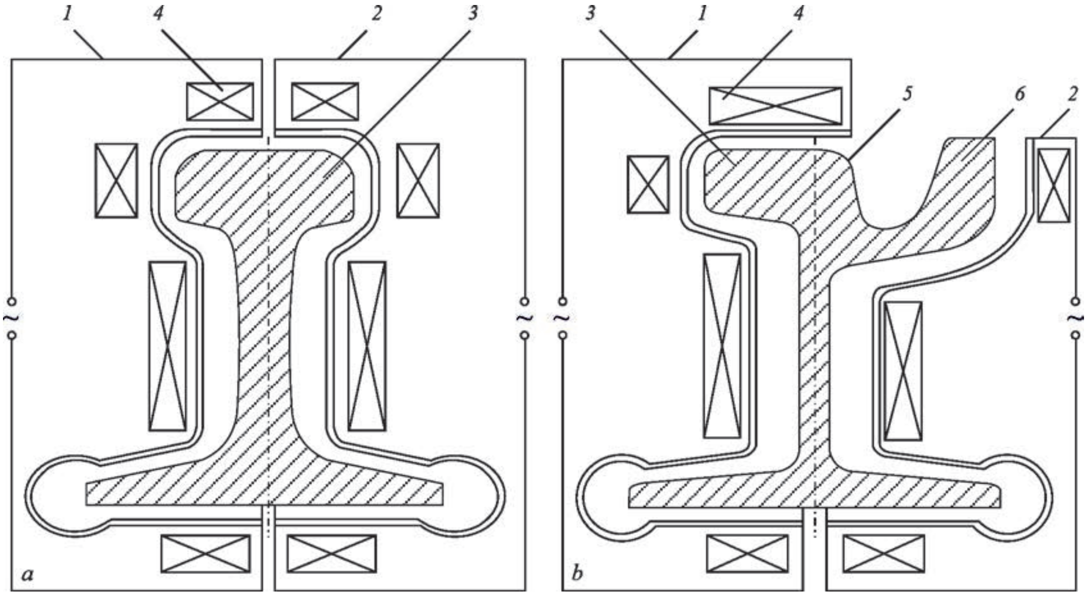

Figure 1. Scheme of heating devices for heat treatment of welded butt joints of railway (*a*) and tram grooved (*b*) rails (description *1–6* see in the text)

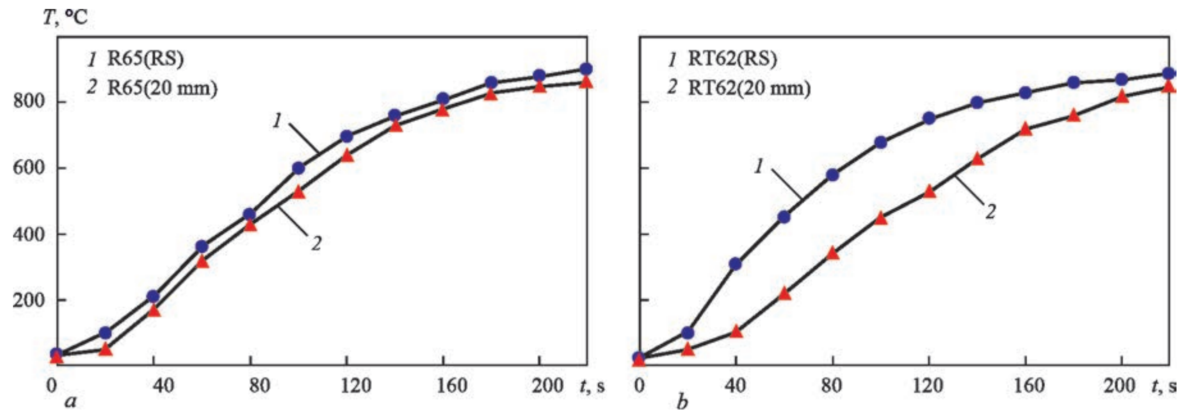

Figure 2. Time dependences of temperature on the rolling surface of the head (RS) and at a depth of 20–22 mm (20 mm) from the rolling surface of railway rails of type R65 (*a*) and tram grooved rails of type RT62 (*b*)

surface over the side surface of the lip, the web and a part of the foot. An inducing wire is extended only to the upper edge of the lip. The air gaps are enlarged over the side surface of the lip, the web and significantly enlarged above the feathers of the rails. Magnetic conductors 4 are mounted over the side surface of the lip, web and a part of the foot of the rail. The metal of the lip is heated partially as a result of thermal conductivity from the heated metal of the head and partially from the induced current on the side surface of the lip. In both inductors, inducing wires also consist of two parallel wires. The total width of the wires exceeds the width of the HAZ of the joints after flash-butt or arc welding.

RESULTS OF STUDIES AND THEIR DISCUSSION

The efficiency of the inductors was investigated in local heating of railway rails of type R65 and tram grooved rails of type RT62 applying currents of 2.4 kHz frequency. The heating temperature was measured on the rolling surface of the head, at a depth of 20–22 mm from the rolling surface, in the centre of the web, at a distance of 10 mm from the edges of the feathers, at the places of transition of the head into the web and the web into the foot, at a depth of 10 mm from the upper edge of the lip and in the centre of the lip. To measure the temperature, chromel-alumel thermocouples were used. The initial temperature of the base metal of the rails was 20 °C. As a power source, a thyristor frequency converter of type TFC-160/2.4 was used. In the process of heating rails to the normalization temperature, the constant value of the TFC rectifier current was maintained. Thus, the reaction of the frequency converter was compensated to the change of the complex load resistance due to the change in the specific electric resistance and magnetic permeability of the rail metal. Figure 2 shows the time dependencies of heating temperature of the head of railway and tram grooved rails. It was found that while heating railway rails during 220 s, the temperature on the rolling surface of the head reached 900 °C. The power at the output of the TFC rectifier varied from 90 to 105 kW. The duration of the heating stage to the temper ture of magnetic transformations, the so-called cold mode, was about 60 % from the time of heating, the average heating rate at this stage was 5.6 °C/s. The duration of heating stage above the temperature of magnetic transformations, the so-called hot mode, was equal to 40 %. The heating rate at this stage decreased to 1.7 °C/s. While heating tram grooved rails during 220 °C, the temperature on the rolling surface of the head reached 890 °C. The power at the output of the TFC rectifier varied from 90 to 100 kW. The duration of the “cold mode” stage was longer than during heating of railway rails. It was about 75 %. The average heating rate was 4.5 °C/s. The duration of the “hot mode” stage decreased to 25 %, the rate of heating at this stage increased to 2.6 °C/s. Figure 3 shows the values of temperature in the cross-section rail elements at the end of the local heating process. In the railway rails the temperature

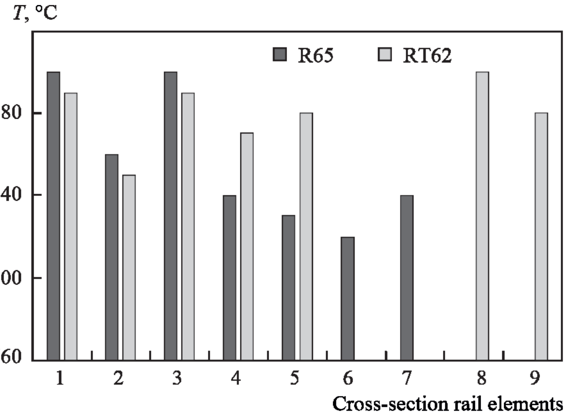

Figure 3. Temperature of heating cross-section elements of railway rails of type R65 and tram grooved rails of type RT62: rolling surface of the head (*1*); at a depth of 20–22 mm from the rolling surface of the head (*2*); web (*3*); feathers (*4*, *5*); place of transition of the head into the web (*6*); place of transition of the web to the foot (*7*); upper edge of the lip (*8*); centre of the lip (*9*)

of the web was equal to the temperature of the rolling surface of the head. The temperature difference between the rolling surface of the head and the layer at a depth of 20 mm was not more than 40 °C, between the centre of the head and the places of transition of the head into the web and the web into the foot did not exceed 20–40 °C. The temperature of the rail feather was at the level of 830–840 °C. The width of the HAZ on the rolling surface of the head, in the centre of the web and the bottom of the foot, was 54 mm. In the places of transition of the head into the web and the web into the foot, the width of the HAZ was by 4–6 mm lower. This is caused by weakening of the proximity effect due to difficulties of mounting magnetic conductors in such places. In the tram grooved rails, the temperature difference between the rolling surface of the head and the layer at a depth of 22 mm was not more than 40 °C. The temperature of the web was equal to the temperature on the rolling surface of the head, the temperature of the rail feather was by 10–20 °C lower. The heating temperature of the upper edge and the centre of the lip almost did not differ from the temperature of other elements.

CONCLUSIONS

Inductors of heating devices for heat treatment of welded butt joints of rail and tram grooved rails performed by the methods of flash-butt or arc welding applying high-frequency currents were developed. Designs of inductors take into account the shape of rails and the volume of cross-section elements.

Checking the efficiency of inductors in a local heating of railway rails of type R65 and tram grooved rails of type RT62 applying the currents of 2.4 kHz frequency showed, that inductors provide a decrease in the heating time of cross-section elements from the workshop temperature to the normalization temperature, the uniform heating of cross-section rail elements, a low temperature difference between the surface and deep layers of metal in the rail head and a reduction in the width of the HAZ after heat treatment as compared to existing equipment.

REFERENCES

1. Shur, E.A., Borts, A.I. et al. (2019) Means of elimination of higher damage of rails in the welded joint zone. *Vestnik VNIIZhT*, 78(**4**), 210–217 [in Russian].
2. Golovin, G.F., Zimin, N.V. (1979) *Technology of heat treatment of metals using induction heating*. Issue 3. Leningrad, Mashinostroenie [in Russian].
3. Feshchukov, A.N. *Device for heat treatment of rail welded butt joints in field conditions*. Russia, Pat. RU168673, Int. Cl. E01B31/18 [in Russian].
4. Rezanov, V.A., Fedin, V.M., Bashlykov, A.V. (2013) Differential hardening of rail joints. *Vestnik VNIIZhT*, **2**, 28–33 [in Russian].
5. (2009) STO RZhL 1.08.002-2009: *Railway rails welded by resistance welding*. Moscow, JSC RZhD [in Russian].
6. Kuchuk-Yatsenko S.I., Antipin E.V., Didkovskyi O.V. et al. Evaluation of quality of welded butt joints of high-strength railway rails of modern production taking into account the requirements of Ukrainian and European standards. *The Paton Welding J.*, **7**, 2–10. DOI: https://doi.org/10.37434/tpwj2020.07.01.
7. Pantelejmonov, E.A., Gubatyuk, R.S. (2016) Induction device for heat treatment of welded butt joints of railway rails. *The Paton Welding J.*, **10**, 41–43. DOI: https://doi.org/10.15407/as2016.10.08.
8. Pantelejmonov, E.O., Datsuk, I.I. (2006) *Induction device for heat treatment of welded butt joints of tram rails*. Ukraine, Pat. 149152, Int. Cl. C21D 1/10 (2006.01) [in Ukrainian].

ORCID

Ye.O. Panteleimonov: 0000-0002-5569-9141

CORRESPONDING AUTHOR

Ye.O. Panteleimonov
E.O. Paton Electric Welding Institute of the NASU
11 Kazymyr Malevych Str., 03150, Kyiv, Ukraine
E-mail: panteleymonov01@ukr.net

SUGGESTED CITATION

Ye.O. Panteleimonov (2022) Inductors for heat treatment of welded butt joints of railway and tram grooved rails. *The Paton Welding J.*, **3**, 45–48.

JOURNAL HOME PAGE

https://pwj.com.ua/en

Received: 20.12.2021
Accepted: 16.05.2022

https://doi.org/10.37434/tpwj2022.03.07

INVESTIGATIONS OF THE QUALITY OF WROUGHT SEMI-FINISHED PRODUCTS FROM VT9 TITANIUM ALLOY PRODUCED BY ELECTRON BEAM MELTING

S.V. Akhonin[1], A.Yu. Severin[1], V.O. Berezos[1], O.M. Pikulin[1], V.A. Kryzhanovskyi[2], O.G. Yerokhin[3]

[1]E.O. Paton Electric Welding Institute of the NASU
11 Kazymyr Malevych Str., 03150, Kyiv, Ukraine
[2]“NVO Khvylia” Company
44/1 Naberezhna Peremohy, 49094, Dnipro, Ukraine
[3]SC “SPC “Titan” of the E.O. Paton Electric Welding Institute of the NASU”
26 Raketna Str., 03028, Kyiv, Ukraine

ABSTRACT

Complex works were performed to study the quality of wrought semi-finished products, manufactured from an ingot of VT9 titanium alloy. Electron beam remelting technology was used to produce ingots of 600 mm diameter and 1.5 m length, from which semi-finished products were manufactured in the form of hot-pressed rods of 315 mm diameter. Results of investigations of structural and mechanical properties of semi-finished products in the form of hot-pressed rods are given. It is shown that the metal of the produced ingots and wrought semi-finished products after the respective heat treatment meets the requirements of the standards.

KEYWORDS: electron beam melting; high-strength titanium alloy; ingot; chemical composition; structure; deformation; mechanical properties

INTRODUCTION

High-strength VT9 titanium alloy of Ti–Al–Mo–Zr–Si alloying system was developed in the middle of the previous century, and it became widely accepted in batch production of parts of gas turbine engines (GTE), which operate for a long time at up to 450 °C temperature [1]. VT9 alloy is a two-phase ($\alpha+\beta$)-alloy. High aluminium content and silicon alloying ensure its higher high-temperature properties, compared to the most widely accepted VT6 titanium alloy. VT6 titanium alloy is deformable, and it belongs to materials with a high heat and corrosion resistance. VT9 alloy is strengthened by heat treatment, namely hardening and aging. An optimum combination of mechanical properties is ensured by double annealing. It is used to make discs, blades and other GTE compressor parts [2, 3].

High requirements are made of service properties of critical parts, which are constantly increased and become more stringent. This largely applies also to the quality of initial materials [4]. Therefore, for extensive application of titanium alloys in different structures it is necessary to not only create new titanium-based materials with higher service properties, but also to improve manufacture of semi-finished products from these alloys further on. Note that any imperfections of chemical or structural homogeneity in titanium alloys lead to lowering of product strength and fatigue life. Producing titanium alloys involves difficulties, which are due to high sensitivity of titanium to interstitial impurities, particularly, oxygen, nitrogen, hydrogen, carbon, as well as interaction with many chemical elements, resulting in formation of solid solutions or chemical compounds. More over, one of the main structural imperfections of titanium alloys is presence of refractory nonmetallic inclusions. High activity of titanium leads to running of physicochemical processes of interaction with gases even in the solid state. Therefore, nonmetallic inclusions, in particular nitrides and oxides, can form both during ingot production, and at different stages of technological processing into finished products. Nonmetallic inclusions can be introduced into the finished product from charge materials during melting, as well as formed at thermodeformational treatment of metal. Titanium actively interacts not only with gases, but also with other elements, including alloying components of the alloys, so that local enrichment of individual volumes of the ingots by alloying elements can lead to formation of intermetallic inclusions, for instance, Ti_3Al, TiAl, $TiCr_2$, and oth. [5].

At present, not all the processes of manufacturing titanium alloy ingots allow producing sound metal,

Figure 1. Ingot of VT9 alloy produced by EBM process

and violation of the technological process of producing titanium alloys results in appearance of defects in the ingots, which lower the metal quality. Electron beam melting (EBM) is the most effective process of vacuum metallurgy to produce alloys, also from refractory and reactive metals, with superlow content of gas, volatile impurities and nonmetallic inclusions. EBM allows controlling the melting rate in a wide range, owing to an independent heating source, that, in its turn, enables controlling the duration of metal staying in the liquid state. EBM is a technology that allows practically completely ensuring removal of high-melting inclusions of high- and low density. Thus, EBM allows improving the quality of titanium alloy ingots [6].

Most of the titanium alloys contain a large number of alloying elements that makes their production by electron beam melting somewhat more complicated. At melting ingots of high-strength titanium alloys by EBM there arises the problem of ensuring the specified chemical composition of the ingot, as melting in vacuum promotes selective evaporation of alloying elements with high vapour pressure [7]. In this case, such elements include aluminium, whereas concentration of elements in the ingot with vapour pressure lower than that of titanium, in this case Mo, Zr and Si, may even become somewhat higher. Calculations of the predicted chemical composition of the ingots were conducted proceeding from fundamental investigations of the processes of alloy component evaporation from the melt in vacuum earlier performed at PWI [6], and their results were used for correction of the billet charge components. The alloying component with a high vapour pressure, namely, aluminium, was added to the charge to compensate for evaporation losses. The charge billet for producing the ingots was formed in a nonconsumable box. Electron beam unit UE5810 was used to conduct the melting operations [6].

Work on producing an ingot of VT9 titanium alloy was performed and an ingot of a round cross-section of 600 mm diameter and 1500 mm length was manufactured (Figure 1). Ingots were produced by cold-hearth EBM technology with portioned feed of liquid metal into a water-cooled crucible.

The side surface of the produced ingots after cooling in vacuum to a temperature below 300 °C is clean without any concentration of impurity elements on the surface in the form of an oxidized or alphized layer. The depth of surface defects of “corrugation” type was 2–3 mm, defects in the form of ruptures, cracks or lacks-of-fusion were absent.

In order to assess the quality of metal of the produced ingots, chemical composition was studied in samples, cut out along the ingot length from the upper, middle or lower part. Results of analysis of the produced ingot metal composition showed that alloying element distribution along the ingot length is uniform, and their content corresponds to grade composition (Table 1).

Ultrasonic testing method was used to study the presence or absence of internal defects in titanium ingots in the form of nonmetallic inclusions, as well as pores. Investigations were performed by pulse-echo method with ultrasonic flaw detector UD4-76 at contact testing variant. When testing the ingots, multiple small-amplitude reflections were observed, that is typical for cast metal and is the result of signal reflection from grain boundaries (dendrites). No shrinkage cavities, porosity or isolated reflections which could be interpreted as large nonmetallic inclusions, were found in the ingot.

In order to determine the influence of electron beam melting technology on the quality of semi-finished products from high-strength titanium alloy hot-pressed rods of 300 mm diameter were manufactured from an earlier produced VT9 alloy ingot of 600 mm dia (see Figure 1).

Forging was performed by the technological procedure, which consisted of three stages.

First stage is heating of 600 mm ingot to 1180 °C temperature; billet soaking for 8 hours; forging on flat heads to form a 450×450 mm square.

Table 1. Distribution of alloying elements along the length of VT9 titanium alloy ingot, wt.%

Alloy grade	Ingot part	Al	Mo	Fe	Zr	Si	O	N
VT9	Upper	6.06	3.63	0.21	1.69	0.32	0.11	0.012
	Middle	6.13	3.68	0.14	1.64	Same		
	Lower	6.64	3.21	0.22	1.67	0.31		
OST1 90013–81 for VT-9 alloy		5.8–7.0	2.8–3.8	≤0.25	1.0–2.0	0.20–0.35	<0.15	<0.05

Second stage is heating of 450×450 mm blank to a temperature of 1100 °C; forging into a round rod of 360 mm diameter and its cutting into three parts.

Third stage is heating the billet of 360 mm diameter to 1100 °C temperature; billet forging through a square into a finished size of 315 mm diameter; and straightening.

The temperature of the end of forging was not lower than 850 °C. Three deformed rods were produced, and a 15 mm thick template was cut from each of them for further studies.

In order to study the quality of the produced semi-finished products from VT9 titanium alloy, comprehensive investigations were performed, which included the following operations: producing templates from wrought semi-finished products; heat-treatment of the templates; preparation of template surface; chemical etching of the templates; control of metal macrostructure; cutting up into samples; determination of polymorphous transformation temperature (T_{pt}), 20° C mechanical properties, long-term strength level at 500 °C; and microstructure control.

Heat treatment of the manufactured forgings and templates cut out of them was performed by the following mode:

- heating up to 950 °C temperature, soaking for 60 min, cooling in air;
- heating up to 550 °C temperature, soaking for 360 min, cooling in air.

After machining and etching of the template surfaces, their macrostructure was studied, and it was established that the macrostructure of the manufactured rod metal does not have any cracks, delaminations, voids, ant no metal or nonmetal inclusions were found.

For further studies samples were cut out of three templates by electric-spark cutting by a scheme given below (Figure 2) for determination of mechanical characteristics and temperature of polymorphous transformation of VT9 titanium alloy.

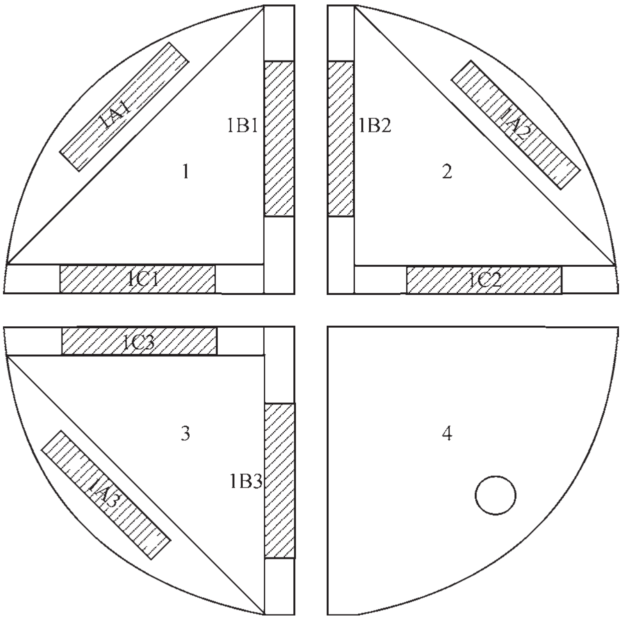

Figure 2. Scheme of cutting up a template into samples for further mechanical testing

The experimentally determined polymorphous transformation temperature (T_{pt}) for these samples of VT9 titanium alloy was 950 °C.

Mechanical properties were determined at temperatures of 20 and 500 °C after conducting the above-described heat treatment. Testing for compliance to standard requirements included tensile, impact toughness, hardness and long-term strength testing (Tables 2, 3).

These data lead to the conclusion that the majority of mechanical properties of semi-finished products from VT9 alloy, produced by EBM process, comply with standard requirements, but the ductility properties turned out to be lower than the standard ones. This may be related to the fact that the deformation temperature was in the region of β-phase existence and a completely platelike structure with a rather large size of the plates formed in the metal. It is known that the values of material ductility very strongly depend on the type of the structure and crystallite dimensions. Lowering of reduction in area with a platelike struc-

Table 2. Mechanical properties of samples of wrought semi-finished product from VT9 titanium alloy

Template number	Sample number	σ_t, MPa	δ, %	ψ, %	*KCU*, J/cm^2	Hardness, *HB*
1	1C1	1129	3.2	9.0	23	341
	1C2	1116	4.8	17.0	25	
	1C3	1120	4.0	12.0	20	
2	2C1	1142	4.8	14.5	23	331
	2C2	1139	Same	12.6	28	
	2C3	1127	3.2	11.8	Same	
3	3C1	1089	4.0	13.4	35	321
	3C2	1078	Same	18.5	Same	
	3C3	1101	6.0	20.6	30	
OST1.90107–73		932–1177	>6	>14	>29	269–363

Table 3. Long-term strength of samples of wrought semi-finished products from VT9 titanium alloy at 500 °C temperature

Template number	Sample number	σ, MPa	τ, h	Note
1	1A1	60	132	No fracture
	1A2		Same	Same
	1A3		96	With fracture
2	2A1	Same	126	No fracture
	2A2		137	Same
	2A3		113	»
3	3A1	»	96	With fracture
	3A2		126	No fracture
	3A3		137	Same
OST1.90107–73		»	≥100	–

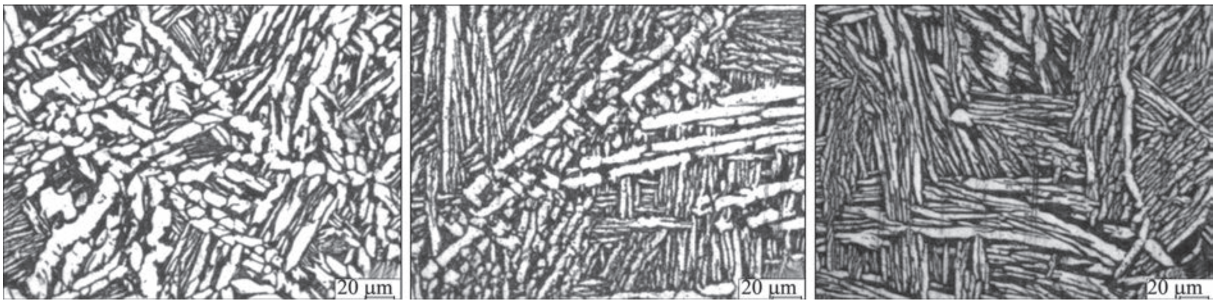

Figure 3. Microstructure of 315 mm dia rods, produced by deformation processing of 600 mm dia ingot from VT9 titanium alloy: *a* — 1; *b* — 2; *c* — 3

Table 4. Mechanical properties of samples of wrought semi-finished product from VT9 titanium alloy after additional heat treatment

Template number	Sample number	σ_t, MPa	δ, %	ψ, %	*KCU*, J/cm^2	Hardness, *HB*
1	1	1068	11	29	29	321
	2	1092	10	14	30	311
2	1	1092	7	16	29	321
	2	1067	10	42	30	Same
3	1	1078	11	29	33	»
	2	1118	14	32	32	»
OST1.90107–73		932–1177	>6	>14	>29	269–363

ture, compared to the globular one, can reach 70–80 wt.%, and relative elongation can be reduced by 40–50 % [8, 9]. Annealing temperature also was quite low — at the lower limit of polymorphous transformation.

Most of the samples of VT9 titanium alloy have passed long-term strength testing at 500 °C temperature and σ = 60 MPa without fracture; average testing time was 122 h.

Analysis of microstructure of the manufactured semi-finished products from VT9 titanium alloy in the form of hot-formed rods of 315 mm diameter showed that the microstructure of all the samples corresponds to type 4a–6a of the 9-type microstructure scale in Instruction No.1054-76 (Figure 3) [10].

Additional heat treatment of VT9 titanium alloy samples was conducted to improve the ductility characteristics. First heating temperature was increased to 980 °C, and the furnace soaking time of samples was extended up to 120 min. Conducted mechanical testing of the samples after additional heat treatment (Table 4) showed the complete compliance of mechanical characteristics of VT9 titanium alloy semi-finished products, manufactured by EBM, with standard requirements.

CONCLUSIONS

1. It is shown that ingots of VT9 titanium alloy, produced by the technology of cold-hearth electron beam melting, are characterized by high homogeneity both by their chemical composition, and by structure, and absence of defects in the form of pores or nonmetallic inclusions.

2. A technological procedure of thermodeformational treatment of 600 mm dia ingots from VT9 titanium alloy is proposed, which ensures producing 315 mm dia rods of a homogeneous structure.

3. Modes of heat treatment of 315 mm dia rods from VT9 titanium alloy were determined, which ensure complete correspondence of semi-finished

product mechanical characteristics to standard requirements.

REFERENCES

1. Pavlova, T.V., Kashapov, O.S., Nochovnaya, N.A. (2012) Titanium alloys for gas turbine engines. *All materials. Encyclopedic reference book*. Moscow, MGTY im. N.E. Bauman [in Russian].
2. Khoreev, A.I., Khoreev, M.A. (2005) Titanium alloys, their application and prospects of development. *Materialovedenie*, **7**, 25–34 [in Russian].
3. Aleksandrov, V.K., Anoshkin, N.F., Bochvar, G.A. et al. (1979) *Semiproducts from titanium alloys*. Moscow, Metallurgiya [in Russian].
4. Antonyuk, S.L., Molyar, A.G., Kalinyuk, A.N., Zamkov, V.N. (2003) Titanium alloys for aircraft industry of Ukraine. *Advances in Electrometallurgy*, **1**, 9–12.
5. Babenko, E.P., Dolzhenkova, E.V. (2014) Examination of destruction causes of large-sized product from VT23 alloy. *Metallurgicheskaya i Gornorudnaya Promyshlennost*, **3**, 82–85 [in Russian].
6. Paton, B.E., Trigub, N.P., Akhonin, S.V., Zhuk G.V. (2006) *Electron beam melting of titanium*. Kiev, Naukova Dumka [in Russian].
7. Akhonin, S.V., Severin, A.Yu., Berezos, V.A. et al. (2016) Peculiarities of melting of titanium alloy VT19 ingots in electron beam cold hearth installation. *Sovrem. Elektrometall.*, **2**, 23–27 [in Russian].
8. Iliin, A.A., Kolachev, B.A., Polkin, I.S. (2009) *Titanium alloys. Composition, structure, properties*: Refer. Book. Moscow, VILS-MATI [in Russian].
9. Elagina, L.A., Gordienko, A.I., Ivashko, V.V. et al. (1978) Influence of structure on mechanical properties of VT9 and VT18 alloys. *Tekhnologiya Lyogkikh Splavov*, **13**, 33–38 [in Russian].
10. (1974) Instruction No. 1054–76: *Metallographic analysis of titanium alloys*. Moscow, VIAM [in Russian].

ORCID

S.V. Akhonin: 0000-0002-7746-2946,
A.Yu. Severin: 0000-0003-4768-2363,
V.O. Berezos: 0000-0002-5026-7366,
O.M. Pikulin: 0000-0001-6327-3448,
V.A. Kryzhanovskyi: 0000-0002-0917-8687,
O.G. Yerokhin: 0000-0003-2105-5783

CONFLICT OF INTEREST

The Authors declare no conflict of interest

CORRESPONDING AUTHOR

S.V. Akhonin
E.O. Paton Electric Welding Institute of the NASU
11 Kazymyr Malevych Str., 03150, Kyiv, Ukraine
E-mail: akhonin.sv@gmail.com

SUGGESTED CITATION

S.V. Akhonin, A.Yu. Severin, V.O. Berezos,
O.M. Pikulin, V.A. Kryzhanovskyi,
O.G. Yerokhin (2022) Investigations of the quality of wrought semi-finished products from VT9 titanium alloy produced by electron beam melting. *The Paton Welding J.*, **3**, 49–53.

JOURNAL HOME PAGE

https://pwj.com.ua/en

Received: 06.10.2021
Accepted: 16.05.2022

https://doi.org/10.37434/tpwj2022.03.08

OPTIMIZATION OF THE DESIGN OF EDDY CURRENT PROBE OF PARAMETRIC TYPE TO DETECT SURFACE CRACKS

V.M. Uchanin

G.V. Karpenko Physico-Mechanical Institute of the NASU
5 Naukova Str., 79060, Lviv, Ukraine

ABSTRACT

The paper summarizes the results of research concerned with optimization of the eddy current probe of the parametric type used for surface defects detection. It is shown that the choice of eddy current probe diameter significantly depends on the smallest length of cracks needed to be detected. In particular, it was determined that to detect a crack longer than 2 mm, it is optimal to use an eddy current probe with windings mounted on the 1.2 mm diameter ferrite core. To detect shorter cracks longer than 1 mm, it is necessary to use an eddy current probe with windings on the 0.75 mm diameter ferrite core. The influence of ferrite core parameters (length, magnetic permeability, and offset of winding from the ferrite core end) on the efficiency of parametric type eddy current probes is analyzed. The results obtained should be used for eddy current probe optimization. The conditions of separation of defect and lift-off influence are analyzed by interpretation of signals in the complex plane, and the possibility of their separation for the developed eddy current probes for all nonmagnetic structural alloys is shown. The design of a parametric type eddy current probe makes it possible to increase their quality factor more than twice. The optimal choice of the cable for connection of an eddy current probe and flaw detector is considered. The optimized parametric eddy current probes were tested. The high sensitivity of the developed probe to short cracks longer than 2 mm with reliable separation of the defect and lift-off influence was shown.

KEYWORDS: eddy current non-destructive testing, surface crack, eddy current probe, ferrite core

INTRODUCTION AND PROBLEM STATUS

Over the recent decades the eddy current method has taken up a leading position among the most widely accepted NDT methods, which ensure detection of surface defects (for instance, fatigue cracks) in metal structures without contact with the controlled surface or even through a dielectric coating [1–9]. We will note as a no-alternative example that only miniature eddy current probes (ECP) may reliably detect cracks in difficult-of-access places of aircraft structures, in particular those located on the side wall of rivet holes, where cracks usually form because of mechanical stress concentration [1, 7]. At the same time, eddy current flaw detection methods are sensitive to a range of factors (in addition to defects), which essentially influence the ECP output signal. These factors include changes in electric conductivity and magnetic permeability of the studied material, variations of the geometrical parameters, or lift-off between ECP and surface of the evaluated object (EO). Experienced operators are looking for a possibility to remove or reduce this interference to obtain reliable control results. Changes of ECP lift-off or inclination are especially critical for manual eddy current evaluation, when ECP position relative to EO changes during scanning. Changes in the lift-off due to different roughness of EO surface, or a change in dielectric coating thickness, can also lead to wrong decisions about presence of defects. Therefore, it is important to reduce the influence of the lift-off for a reliable detection of defects. It is usually difficult to reveal short (even deep) defects in the structures, such as corrosion pits and shallow (even long) cracks. That is why development of testing technologies is aimed at improvement of the possibilities for detection of short and shallow defects with high reliability based on reducing the influence of interference of different physical nature. The reliability of control is used to assess the probability of defect detection, as a qualitative parameter based on statistics. Even for one and the same equipment the probability of defect detection is influenced by several factors, such as EO materials properties, defect type and dimensions, testing conditions, etc.

Important components of the procedure for surface crack detection is selection of ECP type and geometrical parameters for reliable detection of cracks, the dimensions of which characterize the sensitivity threshold, and simple interpretation of the signal that allows separation of useful signals, generated by cracks, from those related to such factors as lift-off or influence of the edge [1, 5, 7, 9]. For the majority of eddy current testing procedures, it is believed to be enough to reliably detect more than 2 mm long and more than 0.2 mm deep cracks that determines the sensitivity threshold of eddy current flaw detectors (ECFD). Such a defect should be reliably detected through a dielectric coating up to 0.5 mm thick. In this case, structural elements protected by anticorrosion coating will be evaluated without a costly procedure of its removal. However, for testing aircraft engine components, an attractive goal is the possibility to detect two times shorter cracks (about 1 mm), for which the eddy current technique can also be used in principle, under the condition of correct selection of ECP parameters.

In works [1–8] different types of ECP were considered and analyzed, which can be used to detect surface cracks. To detect short surface cracks in manual scanning mode, it is the most convenient to use the simplest ECP with one single-layer winding, mounted on a cylindrical ferrite core (FC) [1, 8, 10–13]. An important advantage of such an ECP is the independence of its sensitivity on the crack direction that allows selection of arbitrary scanning paths without the need to maintain ECP orientation relative to the direction of the probable crack. Not less important features of parametric ECP, influencing such a choice, are design simplicity, small size, ease of meeting the requirements as to parameter repeatability in manufacture and low cost [1, 7, 8, 10–11]. Such ECP are traditionally used in self-generator ECFD [8]. More over, single-winding ECP are applied in ECFD operating in resonance mode, the most widely spread of which are known ECFD of DEFECTOMETR family (for instance, DEFCTOMETR 2.837), developed in Germany by Institute Dr. Foerster GmbH&Co). In some all-purpose ECFD, for instance of EDDYCON type, produced by SPC “Promprylad” (Ukraine), or ECFD of ELOTEST M2 type of Rohmann GmbH (Germany), the resonance mode is used as an auxiliary one.

Known is the traditional approach to determination of ECP efficiency, when the surface of a standard specimen (SS) with a defect is scanned and the ECP output signal from the defect is monitored. ECP efficiency is determined by the parameters of the signal from the defect, in particular, its amplitude. Such a procedure is usually used during selection of optimal ECP and working frequency to solve a specific flaw detection task [1, 8, 14]. Such a practice was also envisaged by the European standard on determination of ECP characteristics [15]. With such an approach, it is difficult to compare the results of efficiency evaluation performed by different researchers, as the experiment conditions should be reproduced. In particular, for SS manufacture, it is necessary to use a material with identical electrophysical characteristics and introduce a defect of identical dimensions. A method to determine ECP efficiency, presented by the American Bureau of Standards in works [16, 17], is more advanced. With this method, ECP impedance is measured when it is placed at a distance from SS (in “air”) and when mounted on the surface of aluminium SS. ECP efficiency is evaluated by the difference in the measured impedances. A disadvantage of this method is its dependence on the selected operational frequency, resonance frequency and number of ECP winding turns that limits its application for determination of ECP design efficiency, irrespective of the number of turns and test working frequency.

For quantitative evaluation of the influence of different structural factors on ECP efficiency, it was proposed to use a dimensionless coefficient of eddy current efficiency ξ (Uchanin V.M. Method to determine the efficiency of eddy current probes. Patent of Ukraine 105072, 2014, Bull. No.4). Conditions necessary for studying it were also determined, and invariant properties of the coefficient of eddy current efficiency ξ for windings without FC were also determined, as regards winding diameter and turn number [18]. A procedure for calculation of ECP efficiency ξ was optimized for different ECP variants (also with FC) by the method of volume integral equations [12, 13, 19], using VIC-3D program [20].

This work is a generalization of the results of a number of investigations and developments, related to an optimal selection of structural and electrical parameters of the simplest ECP of parametric type, which are most often used to detect surface defects.

1. ENSURING THE SENSITIVITY THRESHOLD ALONG THE CRACK LENGTH BY SELECTION OF THE DIAMETER OF PARAMETRIC ECP WINDING

Selection of ECP winding diameter is determined by the length of the shortest crack to be detected. A nonoptimal selection of ECP dimensions may lead to overlooking critical defects or unjustified increase of time losses for testing. More over, analysis of the features of ECP signal for cracks of different length is required for interpretation of test results. When selecting the diameter of ECP winding, we will use the results of the work, in which the volume integral method is applied to study the spatial distribution of the signal generated by cracks of different length [9]. During modelling, the crack was located in the center of the system of coordinates: coordinate X corresponded to the direction transverse relative to the crack, coordinate Y ran in the direction along the crack. ECP winding parameters are as follows: average winding diameter D_{av}, winding thickness (difference between the outer and inner radius) Δr and winding height l_o. The signal from the crack was calculated in the form of introduced by the defect module Z_{cr} of ECP impedance, which was normalized to ECP impedance module Z_{eo}, when mounted in EO defectfree part : $Z'_{cr} = \Delta Z / Z_{\mathrm{eo}}$. Crack length and ECP coordinates were normalized to average diameter of ECP winding: reduced crack length l_{cr}/D_{av}, reduced ECP coordinate along the crack $y' = yD_{av}$.

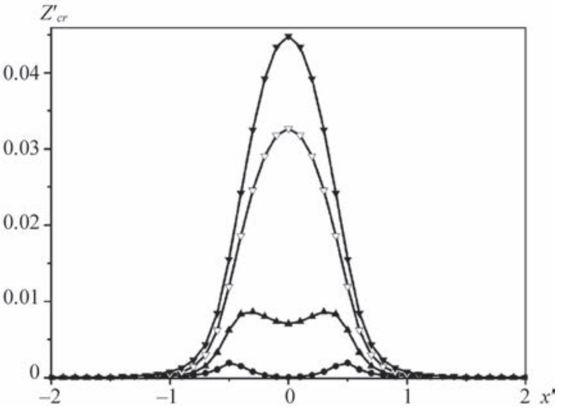

Figure 1. Changes of ECP signal during scanning with reduced lengths: (●) — l'_{cr} = 0.3; (▲) — l'_{cr} = 1.0; (∇) — l'_{cr} = 2.0; (▼) — l'_{cr} = 5.0

During development of eddy current testing procedures, information on the direction of possible propagation of cracks, which in real structures are determined by acting mechanical stresses, is often taken into account. It allows scanning in the direction transverse relative to the crack that corresponds to distribution of ECP signal amplitude along *X* coordinate (Figure 1), which was derived for scanning through the middle (y' = 0) of four cracks of different reduced length (l_{cr}' = 0.3; 1.0; 2.0 and 5.0). One can see that ECP signal dependence for short cracks (l'_{cr} < 0.3) has two maximums, and at ECP location over the center of such a crack (x' = 0), the signal can reach zero. However, with increase of crack length, the maximum amplitude value of the signal from the crack is observed exactly, when ECP is located directly over the defect (x' = 0). With such scanning, the maximum is sufficiently "sharp", when ECP signal from the defect at a short distance, which is close to one diameter of ECP winding, rises abruptly to a maximum, and drops as rapidly after the maximum is passed. Such a feature allows the flaw detector operator reliably separating the signal from the defect from possible interference, the influence of which leads to slower changes of the signal during scanning. This feature is exactly responsible for certain advantages of such a scanning.

Figure 4 gives the distributions of ECP signals during scanning along the crack length by axis *Y* under the condition of preservation of ECP central position relative to the crack mid-plane. Note that the maximums of ECP signal during performance of an ordered transverse scanning in different crack sections (at different *y* coordinates) will also form a profile, similar to the distributions in Figure 2. Derived dependencies allow studying at which ECP position relative to the crack we have maximum signal values and possible sensitivity "dips" ("dead" zones).

Analysis of the obtained distributions (Figure 2) shows their essential dependence on the ratio of crack length to ECP diameter, i.e to the reduced crack length l'_{cr}. Here, not only the amplitude characteristics of ECP signals, but also the general view of signal distributions, change. This encourages us to analyze them separately.

To begin with, we will consider the most interesting case of short cracks, which we will conditionally assume to be cracks of reduced length l'_{cr} < 1.2. For short cracks distribution of ECP signal is of a two-hump symmetrical shape with the minimum at ECP

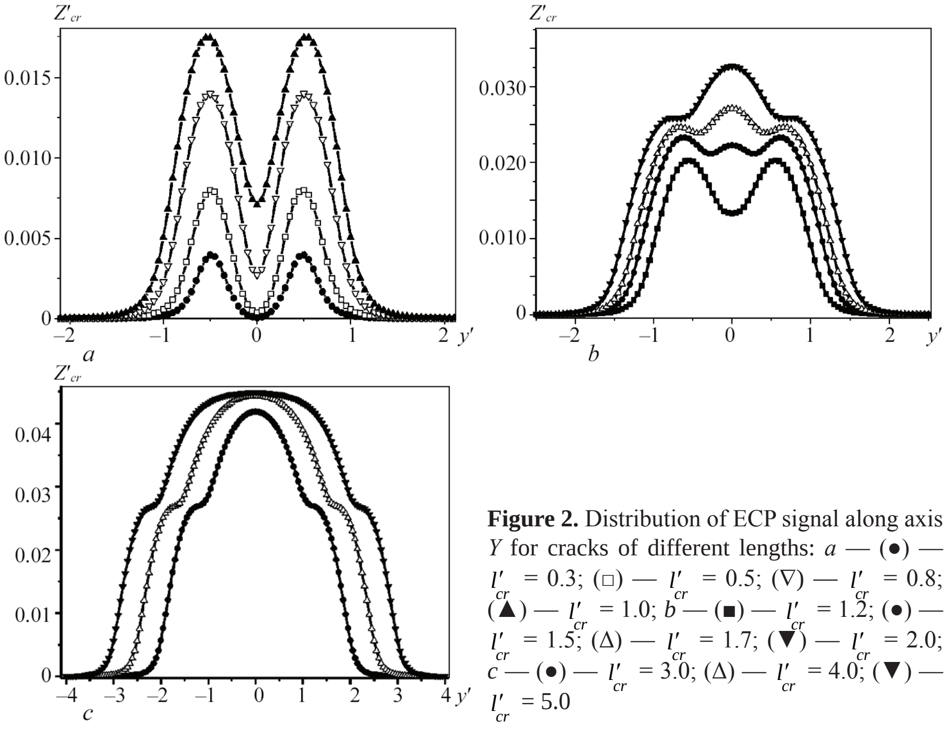

Figure 2. Distribution of ECP signal along axis *Y* for cracks of different lengths: *a* — (●) — l'_{cr} = 0.3; (□) — l'_{cr} = 0.5; (∇) — l'_{cr} = 0.8; (▲) — l'_{cr} = 1.0; *b* — (■) — l'_{cr} = 1.2; (●) — l'_{cr} = 1.5; (Δ) — l'_{cr} = 1.7; (▼) — l'_{cr} = 2.0; *c* — (●) — l'_{cr} = 3.0; (Δ) — l'_{cr} = 4.0; (▼) — l'_{cr} = 5.0

position directly over the crack (at $y = 0$). For a very short crack (relative to ECP dimensions), at $l'_{cr} < 0.3$ the amplitude can reach zero at crack location in the center of ECP winding. This is readily attributable to the features of distribution of ECP eddy current density, which is maximal directly over the winding turns, and fades to zero, when moving closer to ECP center (so-called "dead" zone), that is we have zero ECP signal in the case, when a short crack is located in the central "dead" zone of ECP and practically does not influence the eddy current redistribution. At the same time, ECP signal reaches its maximal value, when the crack middle is located directly under ECP windings, and has a maximal influence on eddy currents. Hence, it becomes clear that for short cracks with $l'_{cr} < 1.0$ the distance between the maximums is approximately equal to winding diameter D_{av}, and in the reduced coordinates in Figure 2, it is equal to 1.0. With increase of crack length, the distance between the maximums increases only slightly (see the distribution for $l'_{cr} = 1.2$ and 1.5 in Figure 2, *b*), and the values of signal amplitude in the minimum point become larger. At $l'_{cr} = 1.5$ the ECP signal distribution already has three maximums, as the central minimum begins to gradually transform into a maximum. With further increase of crack length, this maximum grows (see, for instance, signal changes for $l'_{cr} = 1.7$ in Figure 2, *b*).

At further increase of the crack length, ECP signal distribution has only one maximum, when ECP is located directly in the crack center with two symmetrical almost horizontal regions on both sides. It is important that increase of crack length, beginning from $l'_{cr} = 4.0$ already does not influence the signal amplitude in the central part of the distribution. With increase of reduced crack length l'_{cr}, the central maximum becomes broader, and a horizontal region forms (Figure 2, *c*). Established features of distribution of a signal from cracks of different length allowed suggesting a new method for determination of their length, invariant relative to the specified testing sensitivity (see Uchanin V.M. Eddy current method to determine the crack length. Patent of Ukraine 86505, 2009, Bull. No.3).

"Dips" in signal distribution in Figures 1 and 2, *a*, lead to the conclusion about the possibility of overlooking short cracks under the condition of incorrect selection of ECP diameter and scanning through the crack center. Here, misinterpretation of the results is also possible, as two maximums for a short crack can be taken as signals from two individual defects. Let us consider a physical explanation of the process of formation of the characteristic distribution of ECP signal in the case of a crack of reduced length $l'_{cr} > 1.5$ (Figure 2, *b*). A gradual increase of signal amplitude begins at ECP movement into the crack zone. At further ECP displacement along the crack by axis *Y*, the beginning of the crack enters the "dead" zone, increase of ECP signal amplitude decelerates, and a horizontal region forms. Then the crack crosses the eddy current circuit from ECP other side, and further increase of the signal begins, which reaches a maximum directly over the defect. At further ECP movement, already the crack end falls within the "dead" zone, and another horizontal region forms.

The presented results were used to substantiate the dimensions of ECP for testing aircraft components, where the goal was to detect more than 2 mm long cracks [8]. For this purpose, the optimal ECP are those with windings, mounted on FC of 1.2 mm diameter that corresponds to a relatively uniform signal distribution for $l'_{cr} > 1.7$ in Figure 2, *b*. We will analyze parametric ECP with FC of such a diameter in greater detail in the next section from the view point of optimization of FC parameter selection. An ECP with a winding mounted on FC of 0.75 mm diameter was developed to detect short cracks of more than 1 mm length in aircraft engine parts.

2. OPTIMIZATION OF FERRITE CORE PARAMETERS OF PARAMETRIC ECP

Interaction of ECP turns with the material of the evaluated object (EO) is significantly reduced, depending on the distance from them to EO surface. Therefore, ECP geometry has an essential influence on its sensitivity [1, 16, 17]. FC application has the purpose of increasing the electromagnetic interaction of ECP upper turns with EO material. Therefore, optimal selection of the design of ECP with FC is an important stage of its development. Among the structural parameters of ECP with FC the most essential is FC diameter D_f and length l_f, winding length l_w (which for the single-layer winding is determined by the number of turns *w* and wire diameter *d*) and (offset) shifting l_{sh} of the winding relative to FC end (Figure 3).

It is obvious that FC diameter D_f in most of the cases determines the diameter of ECP winding, selection of which was described in the previous section. All the other above-mentioned parameters of ECP with FC (Figure 3) influence the operation of parametric ECP in different ways. For quantitative evaluation of their influence we will use the given above coefficient of eddy current efficiency ξ (furtheron referred to as efficiency ξ). For parametric ECP with one winding we will analyze FC influence on efficiency ξ, depending on the number of turns *w*, which was varied from 1 up to 100 during calculations. Efficiency ξ of similar

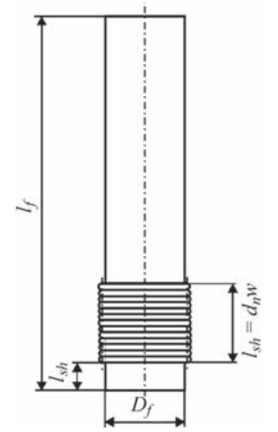

Figure 3. Design of the simplest ECP with one single-layer winding on FC

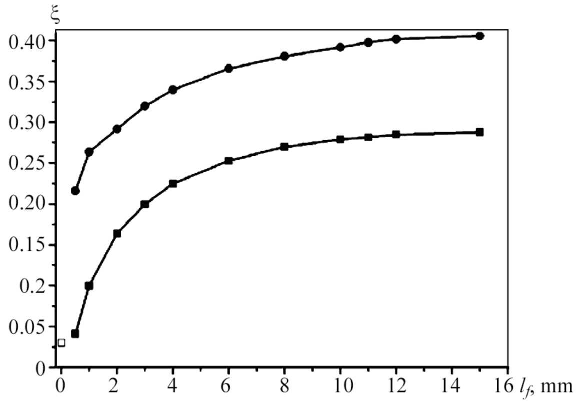

Figure 5. Dependence of efficiency ξ on FC length in case of mounting the winding at FC end (●), with an offset of 0.5 mm (■) and in the absence of FC (□)

windings of ECP without FC was also determined for comparison. Dependence of ξ coefficient on the number of turns was studied, when the winding is placed directly at the end of 10.0 mm long FC with initial magnetic permeability (MP) of the material μ = 100, 600, 1200, 2000 without shifting ($l_w = 0$). Calculations were conducted for working frequency of 10.0 MHz when mounting on a copper sample that corresponds to the conditions of investigation of efficiency ξ [18]. Dependencies of efficiency ξ on the number of turns *w* for coils without core and with FC with different initial MP μ are shown in Figure 4, *a*.

Derived dependencies show (Figure 4, *a*) that efficiency ξ for ECP with single-layer winding, mounted on FC, becomes significantly higher, compared to ECP without a core, depending on winding length (number of turns *w*), even at minimum value of FC material MP μ. At the same time, this effect depends on winding length, as efficiency ξ gradually decreases with its increase. Derived dependencies of efficiency ξ for MP μ = 100 and μ = 600 are rather close. Dependencies of efficiency ξ on the number of turns *w* (or winding length) for μ = 600, 1200 and 2000 are practically identical. This is confirmed by the dependence of efficiency ξ on initial MP μ of FC material (Figure 4, *b*). This dependence was calculated for a single-layer coil, which consists of 25 turns, wound with 0.06 mm wire, placed with a shifting of 0.5 mm on FC of 1.2 mm diameter and 7.0 mm length. Results, presented in Figure 4, *b*, show that efficiency ξ increases from 0.24 up to 0.27 with increase of the initial MP μ from 100 to 2000. The greatest increase of efficiency ξ, however, is observed in the initial portion of the dependence, when MP has not yet reached value μ = 500. At further increase of MP μ, increase of efficiency ξ is insignificant.

The next dependencies (Figure 5) allow evaluation of the influence of FC length and winding position on it on ECP efficiency ξ. For this purpose, efficiency ξ was calculated for ECP, where the single-layer winding consists of 25 turns, wound with 1.2 mm wire. As indicated above, ECP of such a diameter are optimal to detect 2 mm long cracks. Calculations were conducted for core material MP μ = 500. Coefficients of efficiency ξ for parametric ECP with different FC length were calculated for a winding, placed at the end of FC without shifting ($l_{sh} = 0$), and for winding, mounted with shifting $l_{sh} = 0.5$ mm (Figure 3). Efficiency ξ of ECP with similar winding without FC was also calculated and was equal to approximately 0.025 (point □ in Figure 5).

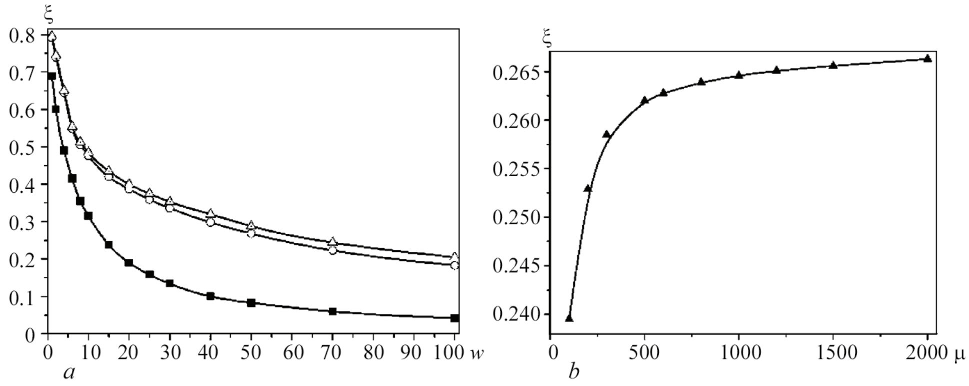

Figure 4. Dependencies of efficiency ξ of single-layer parametric ECP on number of turns w in the absence of FC (■) and with FC with material MP μ = 100 (○) and μ ≥ 600 (Δ) (*a*) and on initial MP μ of FC material (*b*)

The given results show that FC application significantly increases the efficiency of parametric ECP. For windings placed at the end of FC, ξ coefficients are increased 7 times even for short FC 0.5 mm long. ECP efficiency ξ rises with increase of FC length. When a certain FC length is reached (close to 5 mm for this winding), increase of efficiency ξ becomes slower, and when FC length $l_f = 10.0$ mm is reached, it becomes close to the maximum value. These results show that it is rational to select FC length l_f in the range from 6.0 up to 10.0 mm. Here, efficiency of ECP windings mounted with an offset of 0.5 mm, decreases not as strongly as for short FC of the length smaller than $l_f = 2.0$ mm. For FC of length $l_f = 10$ mm shifting of the winding relative to FC end to distance $l_{sh} = 0.5$ mm decreases the efficiency ξ 1.45 times. Such losses can be considered acceptable. Note that such a shifting of the winding relative to FC working end prevents possible ECP failure through wear during scanning of EO surface. Therefore, a certain compromise during selection of winding shifting l_{sh} is justified. More over, these results allow evaluation of the possible changes in ECP characteristics, when part of FC wears in operation. It must be remembered that absolute value of ECP inductance also increases significantly with FC application.

3. OPTIMIZATION OF ELECTRIC AND DESIGN CHARACTERISTICS OF PARAMETRIC ECP

Investigations, presented in Sections 1 and 2, were used to design the basic parametric ECP for aviation industry of Ukraine, in keeping with the specifications of the main customers (SC Antonov, SC Ivchenko-Progress, PJSC Motor-Sich, etc.). Currently available range of FC was analyzed and taken into account during development. The main characteristics of basic ECP are given in Table 1.

SELECTION OF WORKING POINT FOR SEPARATION OF THE INFLUENCE OF THE DEFECT AND THE LIFT-OFF

ECP parameters given in Table 1, determine the impedance of inductive winding Z_w, provided it is placed at a distance from electrically conducting objects (in “air”). Let us consider the changes in electrical characteristics of basic parametric ECP, when placed on nonmagnetic structural materials with different specific electric conductivity (SEC). Inductance L and introduced resistance R_{in} of basic ECP (without cable) were calculated by the method of volume integral equations [11, 12, 19] at operational frequency of 2.0 MHz, when mounted on SS from nonmagnetic metal, the SEC σ of which was changed from 0.05 to 58.0 MS/m. Moreover, inductances of basic ECP without the cable, when mounted on SS with different SEC, were measured, using quality factor meter VM 560. Obtained results (Figure 6, *a*) show a good convergence of the calculation results with the experiment (within 5–8 %). Here, the inductance of basic ECP at operational frequency of 2 MHz decreases essentially in the range of SEC change up to 0.5 MS/m. At further increase of SEC in the range up to 5.0 MS/m, the speed of inductance rise with SEC increase becomes smaller. At further increase of SEC up to copper SEC value (58.0 MS/m) inductance L of ECP winding practically does not change. It allows substantiation of the possibility of using only two modes for ECFD: first — for testing low-conductivity nonmagnetic alloys (titanium alloys, austenitic steel) with SEC from 0.44 up to 2.4 MS/m; the second — for testing in a broader range from magnesium alloys (smallest SEC value of 5.8 MS/m) up to copper (58.0 MS/m). Such a wide range of SEC for the controlled alloys in the second mode can be ensured due to slight changes in basic ECP inductance within the range of SEC changes in these alloys (Figure 6, *a*). It significantly simplifies the design of self-generator ECFD.

With SEC increase, introduced resistance R_{in} of ECP winding first rises to a maximum at $\sigma \approx 0.2$ MS/m, and then begins decreasing that corresponds to general regularities of the theory of eddy current technique as to changes in impedance components with SEC increase [1–6].

The influence of the defect and lift-off between ECP and EO surface can be separated by realization of the “”supercritical” mode (point “B” in Figure 7), which is in place with high values of generalized parameter $\beta = R\sqrt{\omega\sigma\mu\mu_0} > 5$; where: R is the equivalent radius of ECP winding; $\omega = 2\pi f$, where f is the operational frequency; $\mu_0 = 4\pi 10^{-7}$ H/m is the magnetic constant; μ and σ are the relative MP and SEC of EO material.

Figure 7 shows that in the “supercritical” mode the changes of introduced resistance due to defect (D) and lift-off (L) have different sign, unlike the “subcritical”

Table 1. Characteristics of basic ECP

Characteristic	Value
FC diameter D_f, mm	1.2
FC height l_f, mm	7.0
Number of turns w	25
Wire diameter d_w, mm	0.06
FC material MP μ_f	500
Distance l_{sh}, mm	0.5
Number of layers	1
Winding resistance, Ohm	1.2

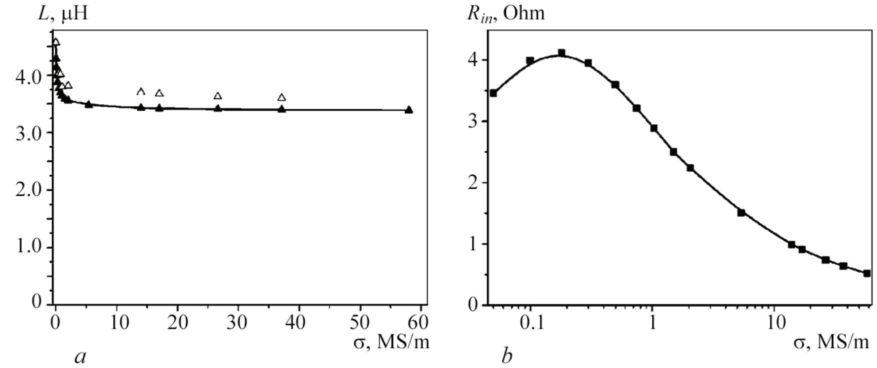

Figure 6. Dependence of inductance *L* (*a*) and introduced resistance (*b*) of basic ECP on SEC σ of EO material: ▲ and ■ — calculation; Δ — experiment

mode (point A). The maximum point in Figure 6, *b* corresponds to the start of fulfillment of the condition of "supercritical" position of the working point of the introduced impedance hodograph, required to separate the influence of the defect and the lift-off. It means that for basic ECP at more than 2.0 MHz working frequencies the possibility of separation of the influence of the defect and the lift-off is realized even for low-conductivity titanium alloys with SEC in the range from 0.44 to 2.4 MS/m.

REDUCTION OF THE INFLUENCE OF PARASITIC COMPONENTS OF IMPEDANCE

Equivalent circuit of parametric ECP, including the components for their connection to ECFD, can be presented in the form of three elements, connected in series. We will denote their impedance as follows: Z_w — impedance of ECP winding directly; Z_t — impedance of winding terminals and Z_c — impedance of the cable for ECP connection to ECFD. Impedance Z_w directly of ECP winding was analyzed in the previous section. Impedance of other elements, in particular, terminal impedance Z_t and connecting cable impedance Z_c are parasitic, as they do not participate in formation of a useful signal from the defect, and their changes may lead to reduction of ECP quality factor on the whole and generation of additional interference. In self-generator or resonance ECFD these elements are part of the oscillatory circuit, so that they can significantly influence their operation and limit ECP interchangeability (Figure 8).

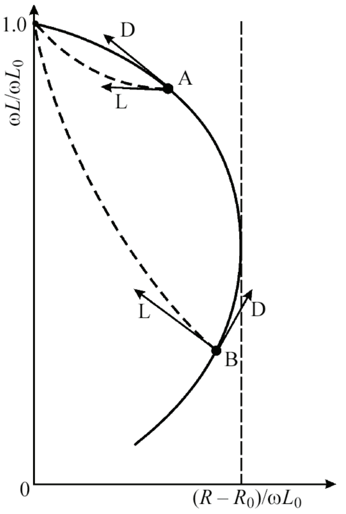

Figure 7. Influence of defect (D) and change of lift-off (L) on the hodograph of ECP impedance for the working point in the "subcritical" (point A) and "supercritical" (point B) modes [1]

Let us consider in greater detail the parasitic components of ECP impedance, namely: terminal impedance Z_t and connecting cable impedance Z_c. Parasitic impedance Z_t can be inadmissibly large, as in parametric ECP with a small number of turns (25 in basic ECP) the terminal length is commensurate with the total length of winding turns. It leads to reduction of informative fraction of the components of parametric ECP impedance (active and inductive resistances), introduced by the defect. Here, ECP quality factor is also significantly reduced. It has an essential influence on their sensitivity in autogenerator and resonance operating modes. In order to reduce the influence of parasitic impedance Z_t of the terminals, a design of parametric ECP was proposed, into which a dielectric insert was incorporated, having two electrically conducting buses, the cross-sections of which are by an order of magnitude larger that those of winding wire (see Uchanin V.M., RybachukV.G., Kyrychenko I.I. Surface parametric eddy current probe. Patent of Ukraine 137775, 2019, Bull. No.21). Figure 9, *a* shows the design of parametric ECP for manual testing, where: *1* is the ECP casing; *2* is the winding; *3* is the connector; *4* is the dielectric insert; *5* are the electrically conducting buses; 6 are the terminals; *7* are

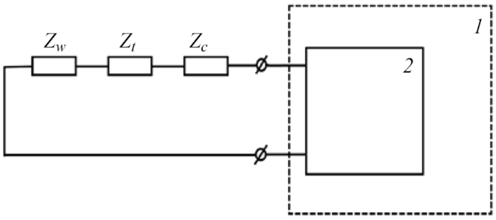

Figure 8. Equivalent circuit of parametric ECP: *1* — ECFD; *2* — oscillatory circuit

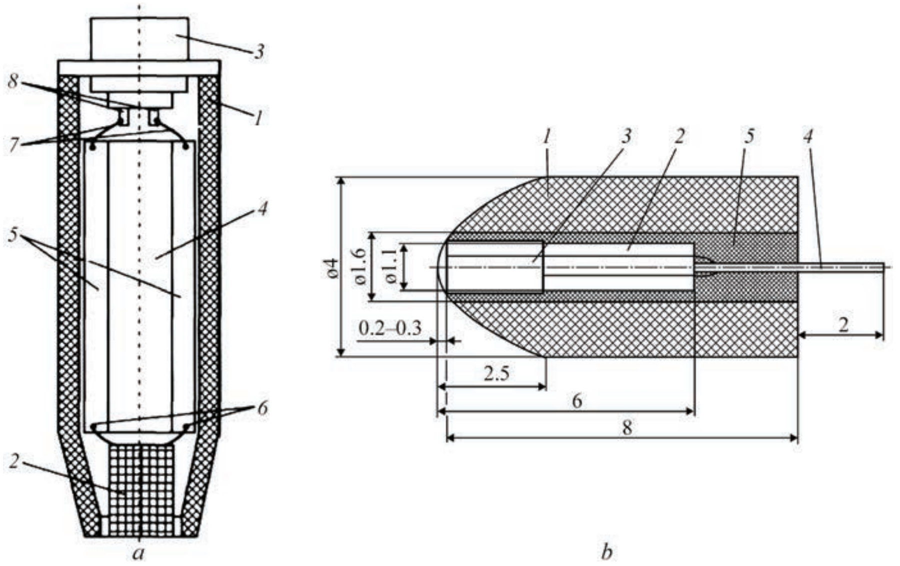

Figure 9. Designs of high-Q parametric ECP: *a* — ECP for manual testing; *b* — miniature ECP for testing difficult-of-access zones using a manipulator

the connecting wires; *8* are the connector contacts. Inductive winding terminals are connected to the ends of electrically conducting buses from the side of insert end face, adjacent to the winding, and terminals of the cable connector or the cable proper are connected to the ends of electrically conducting buses from the side of the opposite end face of the dielectric insert. It is better to place the electrically conducting buses from one side of the plate of the dielectric insert, as in this case their parasitic capacitance is significantly smaller.

In addition, these design features were used to create miniature ECP to detect defects on the inner surfaces of difficult-of-access cavities using manipulators. Design of miniature ECP (Figure 9, *b*) consists of a tubular polystyrol casing *1* of *4* mm diameter and *8* mm height, respectively, which contains FC *2* with winding *3* and dielectric insert *4* with electrically conducting buses. All the ECP elements are fastened in casing *1* using epoxy *5*. The protruding beyond the casing parts of electrically conducting buses of the dielectric insert are the contacts for ECP connection to ECFD cable. Testing showed that the Q-factor of such ECP is $Q = 0.53$, unlike ECP of a traditional design, for which $Q = 0.253$. Thus, the proposed technical solution allows increasing the quality factor of parametric ECP more than 2 times.

OPTIMUM SELECTION OF THE CONNECTING CABLE FOR CONNECTION OF PARAMETRIC ECP

As noted above, the characteristics of the cable for connection of the parametric ECP, also essentially influence ECFD operation. This is particularly true for self-generator and resonance ECFD, in which the cable impedance changes the resonance contour characteristics. Z_c values of the cable depend on its grade and cable length. In order to select the cable grade, its mechanical properties are analyzed, in particular flexibility and resistance to multiple bending during control operation performance. Cable length should be within 1–1.5 m for convenient scanning of EO surface by the operator under real production conditions. Due to that cable impedance Z_c cannot be reduced to such small values compared to winding impedance Z_w that it could be ignored. During cable selection it is important to ensure stable Z_c values during procedural manipulations and ECP interchangeability. The latter is particularly critical for self-generator ECFD of LEOTEST ECFD type, for which it is specified that the distributed capacitance of the connecting cable should be equal to 100 ± 5 pF. Depending on cable grade, not only the capacitance, but also other parameters, in particular specific attenuation (per a unit of length), are changed. In small diameter cables it reaches 0.4 dB/m. In thicker cables this parameter is essentially smaller and may drop to 0.05 dB/m, but they are not quite suitable for application, because of their low flexibility. Cable characteristics, in particular, their quality factor, essentially depend on the used materials. Materials based on polyethylene, polystyrene, and polytetrafluoroethylene are used for insulation. The central conductor of the radiofrequency cable can consist of one or several copper wires, tinned copper, copper with silver coating, etc. For optimal selection of the cable using quality factor meter of VM 560 type, electrical parameters of different cable variants of 1.5 m length were measured. The results are given in Table 2, where: R is the resistance; C is the capacitance; Q is the quality factor; L is the induc-

Table 2. Electrical characteristics of the cables (1.5 m length)

Cable type	R, Ohm	C, pF	Q	L, μH	ρ, Ohm	R_{eq}, Ohm
RK 50-1.5-11	0.24	121.0	6.0	0.23	40.3	242
RK 50-1.5-13	0.09	147.3	10.4	0.15	38.4	399
RK 50-2-11	0.25	168.0	7.0	0.19	33.7	236
RK 75-2-11	0.17	100.6	10.2	0.28	48.9	499
RK 75-2-13	0.20	97.9	10.8	0.34	58.5	632
RK 75-2-13A	0.18	99.0	10.6	0.31	63.5	673
Shielded twisted pair MGTF-0.14	0.41	110.0	12.0	0.79	95.3	1144
Shielded twisted pair MGShV-0.2	0.11	165.0	26.0	0.44	101.7	2644
Shielded wire MGShVE-0.2	0.14	257.0	7.5	0.90	54.8	411

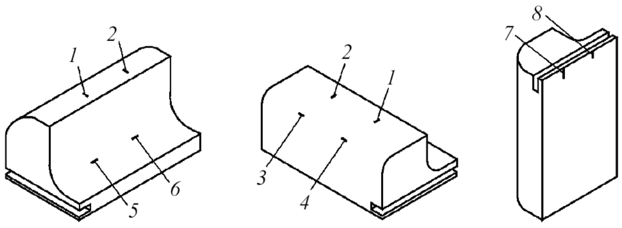

Figure 10. Appearance of SS with defects of SOP 5 type

tance; $\rho = \sqrt{L/C}$ is the wave resistance; $R_{eq} = \rho Q$ is the equivalent resistance.

Analysis of Table 2 leads to the following conclusions:

1. In the absence of stringent requirements as to cable length, all the grades of ratio-frequency cables with up to 100 pF specific capacitance and satisfactory quality factor can be used.
2. As to electrical parameters, cable of RK 75-2-11 grade looks the most suitable. Its application, however, is limited, because of high mechanical rigidity, which rises considerably at low temperatures.
3. Shielded wire pairs of MGTF-0.14, MGShV-0.2 and MGShVE-0.2 grades are hardly suitable for application by the totality of their electrical parameters.
4. Cables of RK-75-2-13 and RK 75-2-13A grades are optimal to manufacture longer (about 1.5 m cables) that is related to low values of specific capacitance.
5. Cables of grades RK 50-1.5-11 and RK 50-2-11 have relatively higher capacitance, lower quality factor, wave and equivalent resistance. Therefore, they can be used in the cases, when a relatively small cable length is admissible.

4. EXPERIMENTAL TESTING OF PARAMETRIC ECP: ANALYSIS OF SENSITIVITY AND POSSIBILITY OF SEPARATION OF THE INFLUENCE OF DEFECT AND LIFT-OFF CHANGE

The ECP presented above was studied using ECFD of EDDYCON type in the resonance mode. ECP was tested using standard specimen (SS) of SOP 5 type from aluminium, and titanium alloy and from ferromagnetic steel, respectively (Figure 10). Short slots of 2 mm length and up to 0.1 mm groove were made on SS surface by electric spark method. Slots of 0.2 and 0.5 mm depth were made on the surface of SS from an aluminium alloy, and slots of 0.5 mm and 1.5 mm depth were made on the SS from titanium alloy and steel. In addition to slots in SS flat part (defects *1*, *2* in Figure 10), slots were made on the cylindrical convex (defects *3*, *4* in Figure 10) and concave (defects *5*, *6* in Figure 10) regions of 6 mm radius. In addition, two defects of 0.5 and 1.0 mm length (defects *7*, *8* in Figure 10) were introduced in SS edge zone. Such SS allow evaluation of ECP sensitivity by defect depth and length in ferromagnetic steels and nonferromagnetic materials with different SEC for flat and curvilinear surfaces. The defectfree portion of these SS was also used to record the ECP signal from a change of lift-off. Looking ahead, we will note that

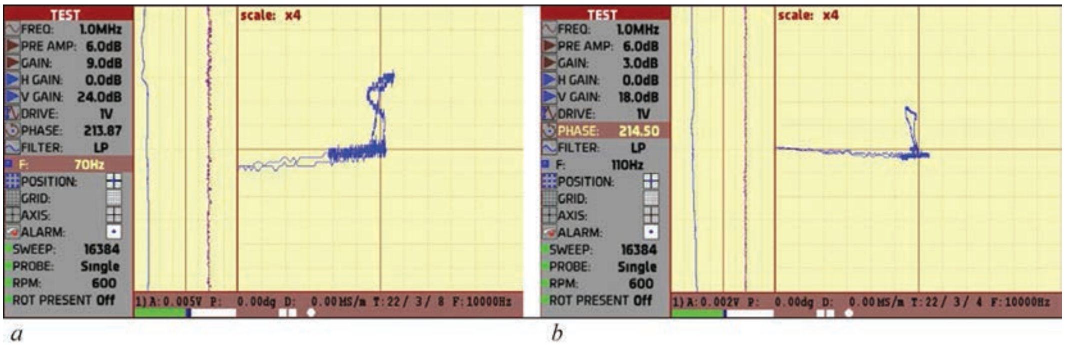

```
FREQ:         1.0MHz
PRE AMP:      6.0dB
GAIN:         9.0dB
H GAIN:       0.0dB
V GAIN:       24.0dB
DRIVE:        1V
PHASE:        213.87
FILTER:       LP
F:            70Hz
SWEEP:        16384
PROBE:        Single
RPM:          600
ROT PRESENT   Off
1) A:0.005V P:  0.00dg D:  0.00MS/m T:22/ 3/ 8 F:10000Hz
```

```
FREQ:         1.0MHz
PRE AMP:      6.0dB
GAIN:         3.0dB
H GAIN:       0.0dB
V GAIN:       18.0dB
DRIVE:        1V
PHASE:        214.50
FILTER:       LP
F:            110Hz
SWEEP:        16384
PROBE:        Single
RPM:          600
ROT PRESENT   Off
1) A:0.002V P:  0.00dg D:  0.00MS/m T:22/ 3/ 4 F:10000Hz
```

Figure 11. Signals of parametric ECP from a cracklike defect 2 mm long and 0.2 mm deep (*a*) and 0,5 mm (*b*) in aluminium alloy SS and from a lift-off change (*a*, *b*) at working frequency of 1.0 MHz

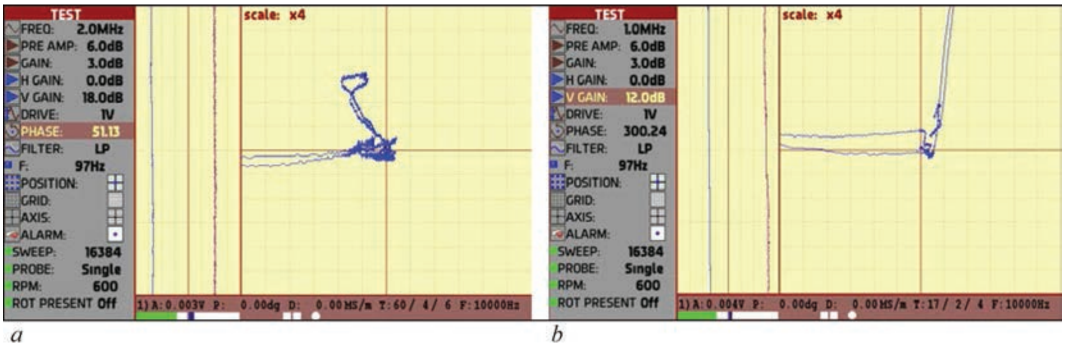

TEST
FREQ: 2.0MHz
PRE AMP: 6.0dB
GAIN: 3.0dB
H GAIN: 0.0dB
V GAIN: 18.0dB
DRIVE: 1V
PHASE: 51.13
FILTER: LP
F: 97Hz
POSITION:
GRID:
AXIS:
ALARM:
SWEEP: 16384
PROBE: Single
RPM: 600
ROT PRESENT Off
scale: x4
1) A: 0.003V P: 0.00dg D: 0.00MS/m T: 60/ 4/ 6 F: 10000Hz

TEST
FREQ: 1.0MHz
PRE AMP: 6.0dB
GAIN: 3.0dB
H GAIN: 0.0dB
V GAIN: 12.0dB
DRIVE: 1V
PHASE: 300.24
FILTER: LP
F: 97Hz
POSITION:
GRID:
AXIS:
ALARM:
SWEEP: 16384
PROBE: Single
RPM: 600
ROT PRESENT Off
scale: x4
1) A: 0.004V P: 0.00dg D: 0.00MS/m T: 17/ 2/ 4 F: 10000Hz

Figure 12. Signals of parametric ECP from a cracklike defect 2 mm long and 1.5 mm deep and from the change of lift-off in SS from titanium alloy (*a*) and from ferromagnetic steel (*b*)

basic ECP allowed reliable detection of all the defects in the above-mentioned SS, including defects on the convex and concave surfaces in the edge zone.

Results of testing parametric ECP to detect short cracks on SS from an aluminium alloy (Figure 11) demonstrated a sufficient sensitivity to defects 2 mm long and more than 0.2 mm deep with good separation of the signal from the lift-off and defect at operational frequency of 1.0 MHz. For this purpose, a methodological technique was used, when vertical sensitivity is higher than horizontal sensitivity (by 24 dB in Figure 11, *a*, and by 18 dB in Figure 11, *b*).

In order to test parametric ECP on titanium alloy SS, the operational frequency was increased up to 2 MHz, because of their essentially smaller SEC. Results of testing SS from a titanium alloy are given in Figure 12, *a*. Figure 12, *b* shows the results of testing SS from ferromagnetic steel at 1 MHz operational frequency. Here, vertical sensitivity is also greater than the horizontal one (by 18 dB in Figure 12, *a*, and by 12 dB in Figure 11, *b*).

Results presented in Figure 12, *a*, *b* show that ECP ensures detection of cracks longer than 2.0 mm in titanium alloys and ferromagnetic steels with the possibility of effective debugging from the influence of lift-off change. Note that the lower sensitivity by depth for defects in titanium alloys, compared to sensitivity to defects in aluminium alloys is known, and it is attributable to their essentially lower SEC. For ferromagnetic steels the sensitivity by depth is often limited by a significantly higher risk of interference, reducing which requires either additional magnetization or application of selective ECP [21].

CONCLUSIONS

1. Results of investigations and developments, associated with optimization of the design of parametric ECP to detect surface defects, were generalized.

2. Selection of ECP diameter was substantiated, depending on the smallest length of cracks to be detected. It is shown that in order to detect more than 2 mm long cracks, application of ECP with windings mounted on FC of 1.2 mm diameter is optimal. To detect short cracks more than 1 mm long an ECP was developed with winding mounted on FC of 0.75 mm diameter.

3. The influence of FC parameters (length, magnetic permeability and winding shifting from FC end) on the efficiency of parametric ECP was analyzed for their optimization.

4. Conditions of separation of the influence of the defect and lift-off were analyzed by interpretation of signals in a complex plane, and the possibility of their separation was shown for all the nonmagnetic structural alloys.

5. A design of parametric ECP is presented, which allows improving their quality factor more than 2 times, and the issue of optimal selection of the connecting cable for ECP connection to ECFD is considered.

6. Testing of basic parametric ECP was conducted, which confirmed its high sensitivity to short cracks more than 2 mm long with reliable separation of the influence of the defect and lift-off.

REFERENCES

1. Dorofeev, A.L., Kazamanov, Yu.G. (1980) *Electromagnetic flaw detection*. Moscow, Mashinostroenie [in Russian].
2. Gerasimov, V.G., Pokrovsky, A.D., Sukhorukov, V.V. (1992) *Non-destructive testing.* In: 5 Books. Book 3: Electromagnetic testing. Moscow, Vysshaya Shkola [in Russian].
3. Libby, H.L. (1971) *Introduction to Electromagnetic Non-destructive Test Methods*, New-York, Wiley-Interscience.
4. García-Martín, J., Gómez-Gil, J., Vázquez-Sánchez, E. (2011) Non-destructive techniques based on eddy current testing. *Sensors*, **11**, 2525–2565. DOI: https://doi.org/10.3390/s110302525
5. AbdAlla, A.N. Faraj, M.A., Samsuri, F., Rifai, D., Ali, K., Al-Douri, Y. (2019) Challenges in improving the performance of eddy current testing: Review. *Meas. Control*, **52**, 46–64. DOI: https://doi.org/10.1177/0020294018801382
6. Rao, B.P.C. (2011) Eddy current testing: Basics. *J. of Non-Destructive Testing & Evaluation*, 10(**3**), 7–16.
7. Hagemaier, D.J. (1991) Application of crack detection to aircraft structures. In: *Fatigue Crack Measurement: Techniques and Applications.* Eds by K.J. Marsh, R.A. Smith and R.O. Ritchie. Warley (UK): EMAS, 419–455.
8. Uchanin, V. (2021) Enhanced eddy current techniques for detection of surface-breaking cracks in aircraft structures. *Transact. on Aerospace Research*, 262(**1**), 1–14. DOI: https://doi.org/10.2478/tar-2021-0001.e, ISSN 2445-2835

9. Uchanin, V. (2007) Specific features of the space distribution of the signal of an eddy-current converter caused by cracks of different lengths. *Materials Sci.*, 43(**4**), 591–595. DOI: https://doi.org/10.1007/s11003-007-0068-2
10. Sobolev, V.S. Shkarlet, Yu.M. (1967) *Surface and screen sensors*. Novosibirsk, Nauka [in Russian].
11. Dyakin, V.V., Sandovsky, V.A. (1981) *Theory and calculation of surface eddy current converters*. Moscow, Nauka [in Russian].
12. Sabbagh, H.A., Sabbagh, L.D., Bowler, J.R. (1988) A model of ferrite-core probes over composite workpieces. *Review of Progress in Quantitative Nondestructive Evaluation*, **7A**, 479–486. New York, Plenum Press.
13. Sabbagh, L.D., Hedengren, K.H., Hurley, D.C. (1991) Interaction of flaw with a ferrite-core eddy current probe: Comparison between model and experiment. *Review of Progress in Quantitative Nondestructive Evaluation*, **10A**, 883–888. New York, Plenum Press.
14. Beda, P.I. (1970) Examination of signal of surface sensor depending on change of sizes and location of crack type defects. *Defektoskopiya*, **1**, 62–68 [in Russian].
15. (2000) EN 13860-2: *Non-destructive testing — Eddy current examination — Equipment characteristics and verification*. Pt 2: Probe characteristics and verification. European Committee for Standardization.
16. Capobianco, T.E., Splett, J.D., Iyer, H.K. (1990) Eddy current probe sensitivity as a function of coil construction parameters. *Research in Nondestructr. Eval.*, **2**, 169–186.
17. Capobianco, T.E. (1987) Field mapping and performance characterization of commercial eddy current probes. *Review of Progress in Quantitative Nondestructive Evaluation*, **6A**, 687–694. New York, Plenum Press.
18. Uchanin, V. (2012) Invariant efficiency parameter of eddy-current probes for nondestructive testing. *Materials Sci.*, 48(**3**), 408–413. DOI: https://doi.org/10.1007/s11003-012-9520-z
19. Dunbar, W.S. (1985) The volume integral method of eddy current modeling. *J. Nondestruct. Eval.*, 5(**1**), 9–14.
20. (1996) *User's Guide for VIC-3D: An Eddy Current NDE Code. Version 2.4*. USA, Bloomington, Sabbagh Associates, Inc.
21. Uchanin, V., Nardoni, G. (2020) Eddy current detection of cracks in ferromagnetic steel structures. In: *The Fundamentals of Structural Integrity and Failure*. Ed. by Richard M. Wilcox, Nova Sci. Publishers, NY, USA, 193–221.

ORCID

V.M. Uchanin: 0000-0001-9664-2101

CORRESPONDING AUTHOR

V.M. Uchanin
G.V. Karpenko Physico-Mechanical Institute
of the NASU
5 Naukova Str., 79060, Lviv, Ukraine.
E-mail: vuchanin@gmail.com

SUGGESTED CITATION

V.M. Uchanin (2022) Optimization of the design of eddy current probe of parametric type to detect surface cracks. *The Paton Welding J.*, **3**, 54–64.

JOURNAL HOME PAGE

https://pwj.com.ua/en

Received: 18.03.2022
Accepted: 16.05.2022